Master of Science Thesis

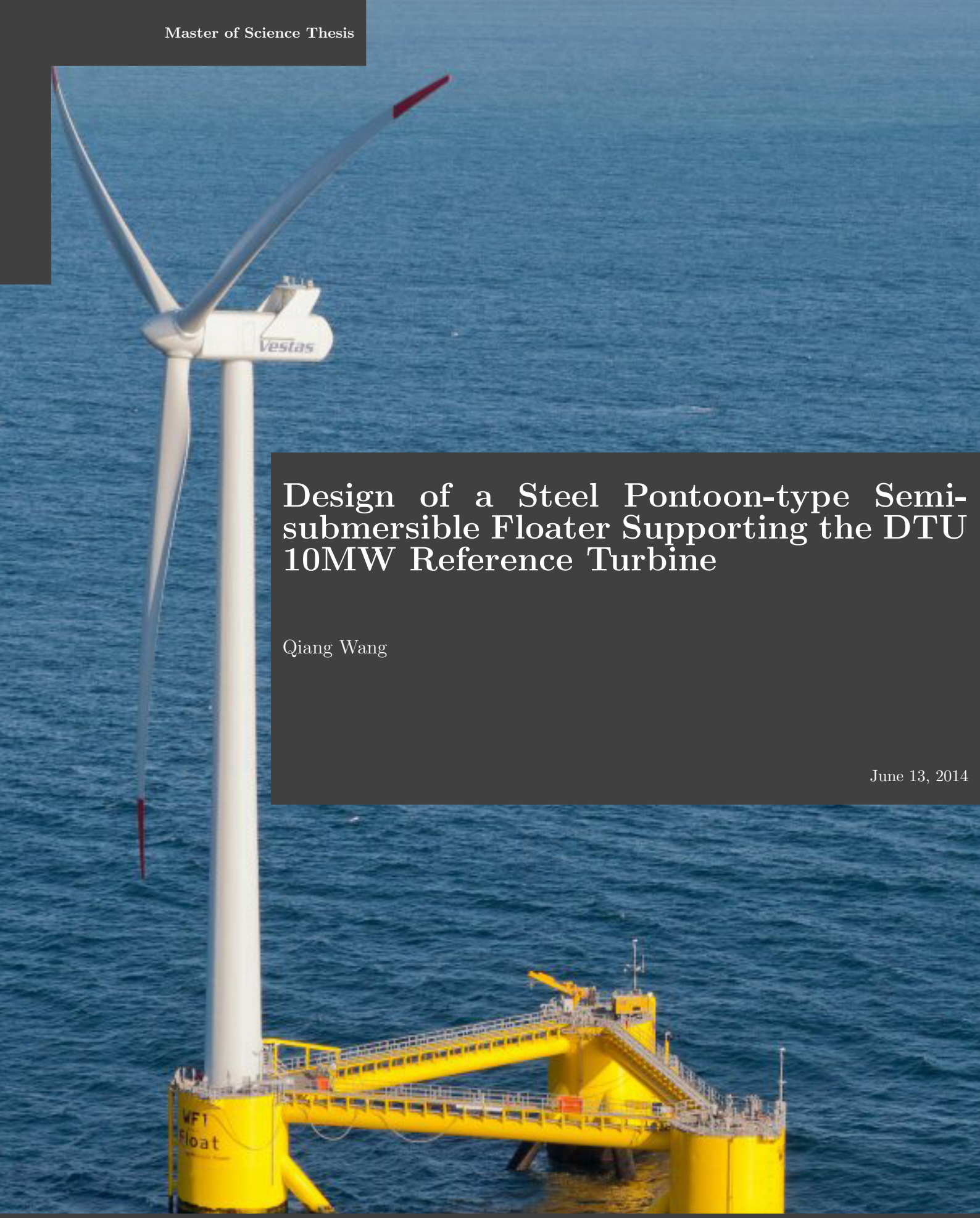

Design of a Steel Pontoon-type Semi-submersible Floater Supporting the DTU 10MW Reference Turbine

Qiang Wang

June 13, 2014

European Wind Energy Master - EWEM - Offshore Engineering Track

Design of a Steel Pontoon-type Semi-submersible Floater Supporting the DTU 10MW Reference Turbine

Master of Science Thesis

For obtaining the degree of Master of Science in Offshore Engineering at Delft University of Technology and in Technology-Wind Energy at Norwegian University of Science and Technology.

Qiang Wang

June 13, 2014

European Wind Energy Master - EWEM

Delft University of Technology
Faculty of Mechanical, Maritime and Materials Engineering
Department of Maritime and Transport Technology
Section of Offshore and Dredging Engineering

Norwegian University of Science and Technology
Faculty of Engineering Science and Technology
Department of Marine Technology

Cover photo - WindFloat, courtesy of Principle Power

European Wind Energy Master - EWEM
Of
Offshore Engineering Track

The undersigned hereby certify that they have read and recommend to the European Wind Energy Master - EWEM for acceptance a thesis entitled **"Design of a Steel Pontoon-type Semi-submersible Floater Supporting the DTU 10MW Reference Turbine"** by **Qiang Wang** in partial fulfillment of the requirements for the degree of **Master of Science**.

Dated: June 13, 2014

Supervisor: _____
Prof. A. Metrikine of TU Delft

Supervisor: _____
Prof. T. Moan of NTNU

Co-supervisor: _____
Dr. Z. Gao of NTNU

Reader: _____
Dr. E. Bachynski of MARINTEK

Reader: _____
PhD(c) C. Luan of NTNU

Summary

In recent years, offshore wind energy has experienced a huge development. Floating wind turbines may become competitive for water depth larger than 50m. However, high cost is still the main challenge for the offshore wind industry. Floating offshore designs provides the possibility to carry large wind turbines to reduce the cost per MWh.

In this thesis, a pontoon-type semi-submersible platform has been designed to support the DTU 10MW reference wind turbine. The initial design is made though upscaling of an existing 5MW semi-submersible platform design. The design is then checked against buoyancy, stability, hydrodynamic and strength criteria. In addition a spread catenary mooring system has been designed based on the catenary theory. Further tests show that clump weight might be needed to balance the strength and stiffness of the mooring lines.

Floating wind turbine models with different levels of complexity have been established and studied through the thesis. In addition, viscous drag force and second order wave force have been implemented. Finally the SIMO-RIFLEX-AeroDyn model is established, and extensive numerical tests have been performed to check the model. The modelling of blades, hub, nacelle and shaft has been found to be difficult and will result in some difficulties in eigenfrequency prediction of the wind turbine. It is also found that the blade pitch controller can excite large platform pitch resonant motion at above rated wind speeds, which could be possibly solved by reducing the PI gains of the controller.

Finally, time domain coupled dynamic analysis of the floating wind turbine system is performed by the SIMO-RIFLEX-AeroDyn code. Characteristic responses of the semi-submersible floating wind turbine are studied and compared to those of the land-based wind turbine. It is found that platform motions have limited influence on the aerodynamic performance of the wind turbine. Besides, operating at rated wind speed is found to produce the largest blade and tower bending moments for both land-based and floating wind turbines. For the floating wind turbine, resonant surge and pitch motions could be excited by turbulent wind under operational conditions which will dominate the response. Second order wave force has some influences on the surge and pitch resonant responses, but these influences are small comparing to those of turbulent wind. However, second order wave force could be important for the study of heave motion, which is wave force dominated even under turbulent wind conditions.

Acknowledgements

First of all, I would like to give my biggest thanks to the coordination of the European Wind Energy Master (EWEM) program. This thesis would be impossible without joining this exciting program.

I would like to give my warmest thanks to Prof. Torgier Moan at Norwegian University of Technology and Science (NTNU) and Prof. Andrei Metrikine at Delft University of Techology (TU Delft) for the kind supervision and arrangements of all the affairs for this new program. I would also like to give a big thanks to Dr. Zhen Gao at NTNU for the co-supervision and weekly meetings, his help is highly appreciated. During the thesis, I also benefit a lot from the discussions with PhD candidates Chenyu Luan regarding the initial design of the 10MW floater which is inspired by his 5MW design. Besides, Dr. Erin Elizabeth Bachynski at MARINTEK has gave me important guidances on the SIMO-RIFLEX-AeroDyn code and the coupled analysis, her comments on the thesis are also very helpful. In addition, the helpful and fruitful discussions with PhD candidates Jacobus Bernardus De Vaal and Lin Li at the Center of Ships and Offshore Structures (CeSOS) at NTNU regarding eigenfrequency analysis and environmental conditions and Dr. Madjid Karimirad at MARINTEK regarding smooth of response spectra are very much appreciated.

I would also like to thank all the other master students in the European Wind Energy Master (EWEM) program following the offshore engineering track: Timothy Cook, Marius Deac, Simon Brauer, Traian Marin, Jinchao Chen, Ying Chen, Niels Verkaik, Oliver Stettner, Bas Verheugt and Marijn Dekker. Together we make it happen!

I am very grateful for all the friends made through my stay at Lyngby, Delft and Trondheim during my master studies. My life is made richer by you.

Finally, I would like to thank my family, for their understanding, support and love!

Trondheim, Norway
June 13, 2014

Qiang Wang

Nomenclature

Latin Symbols

a,a'	Axial and rotational induction factors
$\boldsymbol{a}(\omega)$	Frequency dependent part of added mass matrix
$\boldsymbol{A}$	Added mass matrix
A_w	Water plane area
$\boldsymbol{b}(\omega)$	Frequency dependent part of potential damping matrix
$\boldsymbol{B}$	Potential damping matrix
B_{aero}	Aerodynamic damping per unit length
$B_{viscous}$	Linearized viscous damping coefficient
$\boldsymbol{C}$	Restoring matrix
C_L,C_D	Lift and drag coefficients
C_n,C_t	Normal and tangential force coefficients
$dC_L/d\alpha$	Rate of change of the lift coefficient with angle of attack
f_L,f_D	Lift and drag loads
$\overline{F}$	Mean drift force
$\boldsymbol{F}$	Force vector
$\boldsymbol{F_{drag}}$	Viscous drag force vector
F_D	Diffraction force
F_{FK}	Froude-Krylov force
$\boldsymbol{F_{mooring}}$	Mooring line force vector
$\boldsymbol{F_{wind}}$	Wind force vector
F_x	Axial force along x-axis

g	Acceleration of gravity
$\overline{GM}_L$	longitudinal metacentric height
h	Depth from fairlead to seabed
$\boldsymbol{h}(\tau)$	Retardation function
$\Im$	Imaginary part of an expression
$I_{Drivetrain}$	Drivetrain inertia cast to the low speed shaft
k	Wave number
K_L	Drag force linearization factor
K_P, K_I, K_D	Proportional, integral and derivative gain
l	Mooring line total length
ls	Length of the mooring line that is hanging in water
$\boldsymbol{M}$	Mass matrix
M_y	Bending moment about y-axis
M_z	Bending moment about z-axis
$\boldsymbol{n}$	Normal vector pointing into the fluid
N_{Gear}	High-speed to low-speed gearbox ratio
p	Pressure
P_0	Rated mechanical power
$\partial P/\partial\theta$	sensitivity of aerodynamic power to the rotor collective blade pitch angle
r	Distance to the center of rotation
$\boldsymbol{R}$	Rotation transformation matrix
$\Re$	Real part of an expression
$\boldsymbol{RF}$	Radiation force vector
S_{0B}	Mean body wetted surface
S_{0FS}	Mean free surface
S_B	Instantaneous body wetted surface
S_{SB}	Seabed surface
T_H	Pretension of the mooring line
$T^j_{mn}(\omega_m, \omega_n)$	Difference quadratic transfer function
dT/dr	Thrust force per unit length
u	Wave particle velocity
$\boldsymbol{V}$	Fluid velocity vector
V	Displaced volume
V_0	Wind velocity
$\boldsymbol{V_B}$	Body velocity
V_{rel}	Relative velocity
w	Unit weight of mooring line in water
x	Horizontal distance from fairlead to contact point of the mooring line with seabed

X	Horizontal distance between fairlead and anchor
z_b	Vertical center of buoyancy
z_G	Vertical center of gravity
$^{(1)}$,$^{(2)}$	First and second order quantities

Greek Symbols

α	Angle of attack
ζ_φ	Damping ratio of rotor speed error dynamic system
$\boldsymbol{\eta}$	Body displacement vector
$\dot{\boldsymbol{\eta}}$	Body velocity vector
$\ddot{\boldsymbol{\eta}}$	Body acceleration vector
θ	Local twist angle
λ	Wave length
ξ	Damping ratio
ξ_a	Wave amplitude
ρ	Fluid density
σ	solidity
σ_x	Axial stress
ϕ	Flow angle, velocity potential
φ_k	complex spatial velocity potential for the body oscillating with unitary speed in the kth dof
$\dot{\varphi}$	Rotor speed error
φ_w	Mooring line angle at fairlead
ω	Angular velocity
ω_n	Natural frequency
$\omega_{\varphi n}$	Natural frequency of rotor speed error dynamic system
ω_{damped}	Damped natural frequency

Abbreviations

1P	Rotational frequency of turbine blade
3P	Blade passing frequency for a three bladed wind turbine
BEM	Blade Element Momentum
CFM	Conservation of fluid momentum
CM	Center of mass
DNV	Det Norsk Veritas

dof	Degree of freedom
DPI	Direct pressure integration
DTU	Technical University of Denmark
FFT	Fast Fourier transform
GDW	Generalized dynamic wake
GL	Germanischer Lloyd
GM	Gravity metacentric height
IEC	International Electrotechnical Commission
JONSWAP	Joint north sea wave project
LSS	Low speed shaft
NREL	National Renewable Energy Laboratory
QTF	Quadratic transfer function
RAO	Response amplitude operator
rpm	Revolutions per minute
RWT	Reference wind turbine
SRA	SIMO-RIFLEX-AeroDyn
TLP	Tension-leg platform
ULS	Ultimate limit state
VCB	Vertical center of buoyancy
VCG	Vertical center of gravity

Contents

List of Figures

List of Tables

Chapter 1

Introduction

1.1 Offshore Wind Energy

Wind energy is believed to be one of the most promising clean energy solutions for the future. Offshore wind energy has many advantages over onshore wind energy, including [1, 2]:

- Higher and steadier wind speed, which lead to higher potential power output and greater predictability;
- The potential for deployment of larger wind turbines and development of larger wind farms leading to benefits of economy of scale.

Since the success of the first offshore wind farm at Vindeby in Denmark in 1991 [1], the offshore wind industry has experienced significant growth in recent years, especially in Europe. At the end of 2012, the installed offshore wind capacity reached 5 GW in total [3] as shown in Figure 1.1. As predicted by European Wind Energy Association (EWEA) [3], by 2020 this number could be eight times higher, at 40 GW, meeting 4% of European electricity demand. By 2030, offshore wind capacity could reach 150 GW in total, meeting 14% of the EU's total electricity consumption. Finally, by 2050 offshore wind could reach 460 GW, contributing to a European power supply met 50% by wind.

Currently, all commercial offshore wind projects are limited to a water depth less than 50m with bottom fixed structures. As indicated by a study by a Task Force that includes 16 leading companies in the offshore wind sector [4], floating designs are necessary to unlock the promising offshore market potential in deeper water regions such as the Atlantic, Mediterranean and deep North Sea waters, as shown in Figure 1.2. Besides, it also shows that floating designs would become competitive in terms of levelised cost of energy with bottom fixed foundations in more than 50m water depth.

However, there is a big disadvantage for offshore wind energy,namely the high cost [1, 2]. Cost reduction remains one of the main challenges for the offshore wind industry.

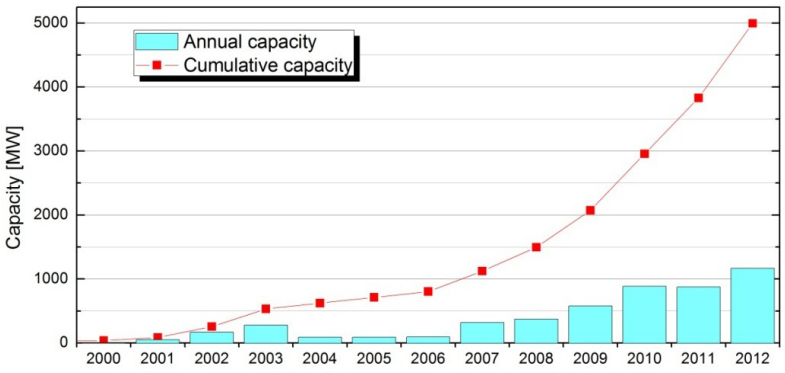

Figure 1.1: *Annual and cumulative installed capacity of offshore wind in Europe (based on Ref [3])*

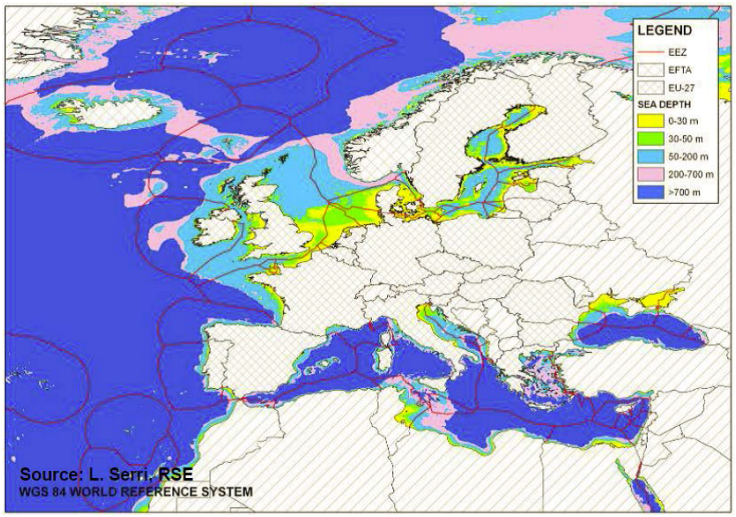

Figure 1.2: *European bathymetry map (Ref [5])*

Comparing to fixed-bottom solutions installed in deep waters, floating offshore designs are expected to have lower design and installation costs. Besides, floating offshore designs are also expected to produce more energy as they can accommodate bigger wind turbines to lower the final cost per MWh [3]. This is the key motivation for this thesis work.

1.2 Floating Wind Turbine Concepts

1.2.1 Background

The concept of floating wind turbine system was for the first time introduced in 1970s by professor Heronemus [6] from the University of Massachusetts at Amherst. Close to 40 years later, floating wind turbines are becoming a reality.

In 2009, Statoil installed the first grid connected floating wind turbine, Hywind [7], in Norway, with a 2.3 MW Siemens wind turbine. Two years later, another concept, Wind-

Float [8], developed by Principle Power was installed off the Portuguese coast with a 2 MW Vestas wind turbine. More recently, in 2013, Japan has installed the Compact Semi-Sub 2MW floating wind turbine as the first phase of the Fukushima Floating Offshore Wind Farm Demonstration Project(Fukushima FORWARD [9]). In addition, one Advanced Spar and one V-shape Semi-Sub concepts both with a 7MW wind turbine are planned in the second phase.

At the same time, many other exciting concepts are under developing and testing right now around the world. An overview of the concepts of floating wind turbines that are being developed could be found from reports by European Wind Energy Association [3] and Main(e) International Consulting [10].

1.2.2 Concept Classification

Because offshore wind turbines have a large top mass and a large thrust force acting at a height over 80m above the sea surface, the stability of the floating platform is a big challenge. Solutions to this challenge fall into three different strategies, based on the way they reach the stability in pitch/roll [11, 12]:

- Gravity-based, with the center of gravity under center of buoyancy. Similar to spar platform.
- Waterplane area based, with a wide free surface area to achieve large moment of inertia. Similar to barge and semi-submersible platform.
- External constrain based, with large external mooring forces to keep the platform stable. Similar to Tension-leg platform.

So far, all of the three strategies have been used to develop floating wind turbine platforms. They are discussed in the following [11, 12]:

Spar is a gravity stabilized structure which requires a very large draft. Spar usually has good stability and small heave motions. However, the necessary hull draft precludes using the spar in less than 100m of water depth. Besides, the transportation and installation of the spar requires very nice weather and significant offshore operation. The large draft may also limit the possibility to tow-back for major maintenance.

Semi-submersible is a waterplane area moment of inertia stabilized structure with flexible draft capability. The structure can operate in different draft, allows it to be fully assembled in a sheltered harbor and then wet-towed to its installation site. The procedure could also be inversed when there is a need for major maintenance. A main concern is that semi-submersible may experience large heave motions in waves.

Tension-leg platform use tendons to provide stability of the structure. The motion of the platform is limited due to the external tendons. However, the difficulties lie in the natural frequency similarities and the potential of structural coupling between the wind turbine and the tendons. Besides, the installation of TLP could

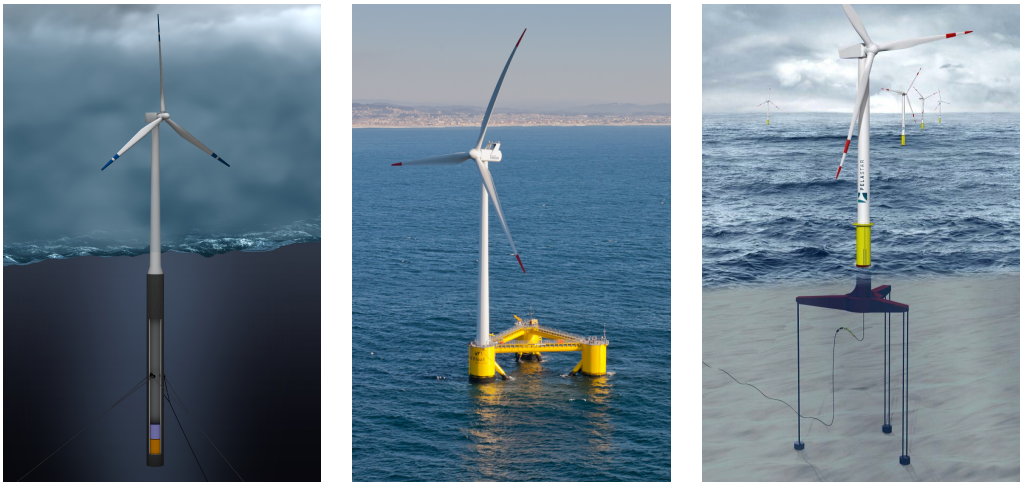

Figure 1.3: *Concepts of floating wind turbine platform (left to right: Spar-Hywind (courtesy of Statoil), Semi-submersible-WindFloat (courtesy of Principal Power), TLP-Pelastar(courtesy of Glosten))*

be difficult since the structure is not unconditionally stable during towing and it requires significant sea bed preparation before installation. The same difficulty will also apply to tow-back in case of a major maintenance.

Three examples of the above concepts are shown in Figure 1.3.

As pointed out by Roddier [13], in general terms, spar have better heave performance than semi-submersible due to its deep draft, but it has more pitch and roll motions due to the limited water plane area. TLPs have very good motions, but the complexity in the mooring system design and installation, as well as other difficulties discussed above are main challenges. Besides of motions, economics plays an important role in comparing floater types. Then, the flexibility in operating water depth brings the semi-submersible floating wind turbine concept on top of the others.

1.2.3 Research in Semi-submersible Wind Turbine Concepts

The semi-submersible floating wind turbine concept become popular after the WindFloat concept was introduced in 2009 in a three part OMAE paper [14, 15, 16], which was summarized in the later journal paper [13]. In these papers, the authors discussed the design basis, stability, hydrodynamic performance and structural assessment of the WindFloat concept. As shown in Figure 1.4, this WindFloat concept has three columns with the wind turbine sitting on one of the columns. The columns are connected to each other by braces. It is stabilized by the buoyancy of the three columns plus an active ballast system. Heave plates are introduced at the bottom of each column to improve the motion performance by extra added mass and damping. As mentioned, two years later, this concept was installed full scale with a 2MW turbine. In the same year, a generic version of the concept was published [11] supporting the 5MW NREL turbine [17] with details for numerical tool validation and comparison.

Some other recent activities include the ongoing IEA Task30 OC4 Phase II project [18], which is focused on the analysis of a semi-submersible platform developed by DeepCWind project, with model test performed at MARIN [19]. In this three-column semi-submersible concept the 5MW NREL wind turbine is supported by an extra central column so as to get rid of the active ballast system used in the WindFloat concept. The columns are also connected by braces. Recent researches are mainly focused on modeling and hydrodynamic analysis of this concept [20, 21, 22]. Another type of semi-submersible platform is suggested by the ongoing EU HiPRWind[1] project. This semi-submersible platform consists of three columns with heave plates connected by braces. The turbine is placed in the center of the platform with support from braces only. No center column or active ballast system is used in this concept.

The concepts of WindFloat, DeeCWind and HiPRWind semi-submersible platforms are shown in Figure 1.4.

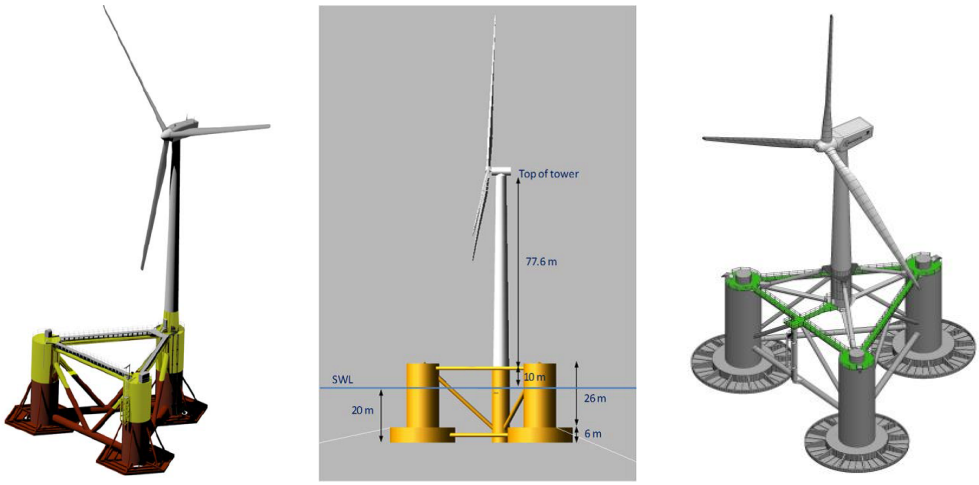

Figure 1.4: *The concept of WindFloat(left, courtesy of Principle Power), DeepCWind(middle, courtesy of DeepCWind Consortium) and the concept of HiPRWind(right, courtesy of Olav Olsen)*

It is clear from Figure 1.4 that all of these semi-submersible wind turbine platform concepts use brace system, which is however unfavourable for floating offshore structures because of fabrication difficulties and potential for fatigue failure. One famous example is the Alexander L. Kielland disaster [23, 24] in 1980, from which the offshore industry learned to avoid brace system. Therefore, it will be interesting to design and investigate a braceless type of semi-submersible platform for offshore wind turbines - the pontoon-type semi-submersible platform.

1.3 Mooring System

Mooring system is the traditional way to keep floating structure in position. Although sometimes thruster can also be used for station-keeping, they are not relevant for floating wind turbines.

[1]The HiPRWind project, http://www.hiprwind.eu/

A mooring system is made of a number of lines (chain, rope or combination of both) with their upper ends attached to different points of the floating structure and their lower ends anchored at the sea bed [25]. Typical types of mooring systems includes [26]:

Catenary Line Mooring. It obtains restoring force mainly by lifting and lowering the weight of mooring line. In a normal spread mooring, several pre-tensioned anchor lines are arrayed around the structure to keep it in position. This system requires significant length of anchor lines lie on the seabed to ensure the anchor be kept in position during operation. Chain and wire are most common for this mooring system.

Taut Line Mooring. The mooring system has a pattern of taut, light-weight lines radiating outward. The lines have a low net submerged weight, and the system gets its restoring force primarily from elastic stretch of the line itself. Synthetic fibers are most common for this type of mooring.

Tension Leg Mooring. This special mooring system is used for tension leg platforms (TLP). The buoyancy of the platform exceeds its weight and a net downward force is supplied by the vertically tensioned mooring, secured by deadweight or anchor piles at seabed.

Musial [27] has discussed the advantages and disadvantages of these mooring systems. For the catenary line mooring system and taut line mooring system, clump weights or buoys can be attached to the mooring lines to improve the system performance [28]. For more information, the reader can refer to design codes such as DNV-OS-E301 [29] and API RP 2SK [30].

Almost all of today's semi-submersible platforms use spread catenary line mooring system, and about 85% of all semi-submersible platforms use all chain systems [31]. It is more popular to use all chain system in shallow water (typically less than 600ft [32]), and to use a combination of chain and wire system in deeper water [30].

As for semi-submersible floating wind turbine platforms, only spread catenary line mooring system has so far been studied. WindFloat [13] initially uses 6 all chain catenary mooring lines at a water depth of 150m. A later modified version of the concept [11] uses 4 catenary mooring lines at a water depth of 319.9m, with each line consisting of two short sections of chain at the ends and one main section of polyester rope in the middle. The DeepCWind semi-submersible concept also uses catenary mooring system at a water depth of 200m. The mooring system consists of three spread lines with uniform properties [20]. The HiPRWind semi-submersible concept platform is moored by 3 all chain catenary lines at water depth of 80m [33].

Masciola [34] has assessed the importance of mooring line dynamics on global response of the DeepCWind semi-submersible platform. It is shown that the mooring line dynamics has limited influence in the heave and surge motion, but are important for calculating the mooring line tension in extreme conditions. López-Pavón [33] has studied the influence of second-order wave force on mooring system of the HiPRWind semi-submersible concept. It is shown that although the results with full quadratic transfer functions (QTF) give better results than those with Newman's approximation, both of them show a big difference with

the experiment. It is therefore alerted by the author regarding the difficulties in estimating slow-drift forces on this kind of structure.

Most of the studies are based on coupled dynamic simulation tools, more details of which will be addressed in the following section.

1.4 Tools for Coupled Dynamic Analysis of Floating Wind Turbines

A floating wind turbine system includes rotor, nacelle, tower, platform (floater) and mooring system. Unlike a fixed wind turbine system which could be treated by uncoupled dynamic analysis, Karimirad [35] shows that for a floating wind turbine system, the coupling of the top side and the floater is important. For the analysis of the floating wind turbine system, the key issue is how to combine the highly nonlinear and dynamic loading and responses of the rotor, nacelle, tower, floater and mooring lines [36]. This requires nonlinear stochastic time-domain analysis tools that can be used with hydro-elastic-aero-servo simulations [37]. Several numerical tools are available for the coupled dynamic analysis of floating wind turbines. Cordle [38] has provided a review of the available codes. Comparisons of different codes have been carried out through the IEA's Offshore Code Comparison Collaboration (OC3) [39] and Offshore Code Comparison Collaboration Continuation (OC4) [40].

In the following part of the section, selected numerical codes of FAST, HAWC2 and SIMO/RIFLEX are introduced. It should be noted that further development of each code and expansion of its capability in the future version is expected, the following introduction only applies to the tools at the time of writing.

FAST

FAST [41] is a public available code for nonlinear aero-servo-elastic analysis of fixed horizontal-axis wind turbines developed by National Renewable Energy Laboratory (NREL). Jonkman [17, 42] has extended it to include HydroDyn to enable hydro-elastic response calculation of floating wind turbines.

The extended FAST code uses a combined modal and multibody system dynamic representation to perform structural dynamic analysis. The blades and tower are modelled using linear modal representation with mode shapes obtained by a finite element preprocessor. The aerodynamic loads is calculated using the AeroDyn [43] module based on blade element momentum (BEM) theory or a generalized dynamic wake (GDW) model. Hydrodynamic forces are calculated by HydroDyn with hydrodynamic coefficients obtained from frequency domain radiation/diffraction preprocessor (such as WAMIT [44]). The mooring system is dealt with using a quasi-static approach.

This FAST tool has been applied to coupled dynamic analyses of many different kinds of floating wind turbines, including ITI Energy barge, MIT/NREL TLP and OC3-Hywind spar buoy [45] as well as the SWAY concept [46] and the DeepCWind semi-submersible concept [20].

In addition, the FAST code has been combined with many other dynamic programs to perform coupled dynamic analysis of floating wind turbines. Shim [47] has combined FAST with FEM program Charm3D to perform coupled dynamic analysis of a TLP floating wind turbine. Roddier [13] has combined FAST with TimeFloat to perform coupled dynamic analysis of the WindFloat concept.

HAWC2

HAWC2 [48] is an aeroelastic code intended for calculating wind turbine response in time domain developed by DTU Wind Energy. The structural part of the code is based on a multibody formulation, where each body is an assembly of Timoshenko beam elements such that complex structures and arbitrary large rotations of the body can be accounted for. The turbine is modelled by an assembly of bodies connected with constraint equations. The aerodynamic part of the code is based on extended BEM theory while the hydrodynamic part of the code is limited to Morisons equation. A second option of coupling the HAWC2 code to WASIM for the hydrodynamic loads calculation is currently under development. The mooring system is limited to a user defined force-displacement relationship, same as the FAST code.

Karimirad has used the HAWC2 code throughout his PhD career to perform coupled dynamic simulations of spar-type floating wind turbines with catenary and taut mooring systems, a list of the related research works can be found in his PhD thesis [37]. Jiang [49] has used the HAWC2 code to study the fault conditions of a spar-type floating wind turbine.

SIMO-RIFLEX-AeroDyn

SIMO [50] is a time domain simulation program developed by MARINTEK for multi-body system. RIFLEX [51] is a non-linear FEM program developed by MARINTEK for static and dynamic analysis of slender marine structures. SIMO-RIFLEX is the state-of-the-art tool for dynamic response analysis of moored offshore structures.

In order to overcome the shortcomings of the FAST and HAWC2 codes, and to address the need for large volume hydrodynamics and second order forces in floating wind turbine analysis, the code SIMO-RIFLEX is extended with AeroDyn by Bachynski [52] to form the SIMO-RIFLEX-AeroDyn (SRA) code.

In the SIMO-RIFLEX-AeroDyn code, the blades, tower and mooring lines are all modelled with flexible beams, while the hub, nacelle and floater are modelled as rigid bodies. Similar to the FAST code, the aerodynamic loads is again calculated by AeroDyn based on BEM or GDW model. The hydrodynamic forces are modelled by SIMO with the loads transfer functions and hydrodynamic coefficients again obtained by external frequency domain radiation/diffraction solver.

Bachynski has used the RIMO-RIFLEX-AeroDyn code for the analysis of TLP floating wind turbines, which is well documented in her PhD thesis [52]. The code was also used by Kvittem for the analysis of semi-submersible floating wind turbines [53, 54].

1.5 Scope of the Thesis

The aim of this thesis is to study the theoretical feasibility of supporting a 10MW wind turbine by a pontoon-type semi-submersible platform. As indicated by the title, the whole thesis includes two parts, namely design and analysis. It should be well noted that during the thesis, the design and analysis activities are coupled with each other.

The design part of the thesis includes:

- Initial design of a semi-submersible platform to support a 10MW reference wind turbine;
- Preliminary design of the mooring system.

The analysis part of the thesis includes models with different level of complexity:

First model. The wind turbine is presented only in the mass model and no mooring system is included, no wind loads is considered. Frequency domain hydrodynamic analysis of the platform under wave conditions is performed in HydroD. This model is used to check the initial design of the semi-submersible platform.

Second model. The wind turbine is still represented by a mass model, but the mooring system is modelled using beam elements, a constant thrust force is applied as wind loads. Time domain hydro-elastic dynamic analysis of the floater under wave conditions is performed in DeepC. This model is used to check the preliminary mooring system design.

Third model. Both wind turbine and mooring lines are modelled by beam elements in RIFLEX, constant wind or turbulent wind is modelled and aerodynamic loads are calculated by AeroDyn. Coupled time domain aero-hydro-servo-elastic simulations are performed in SIMO-RIFLEX-AeroDyn under combined wind and wave conditions. This model is developed to perform coupled dynamic analysis of the floating wind turbine system.

The thesis is organized in the following way:

In Chapter 1 the background of offshore wind energy and concepts of floating wind turbine platforms are introduced, followed by a literature review of mooring systems and coupled dynamic analysis codes.

In Chapter 2 basic theories of wind turbine aerodynamics, linear and second order floater hydrodynamics as well as the theory of coupled dynamic analysis are presented.

In Chapter 3 the DTU 10MW reference wind turbine is presented and compared with the NOWITEK 10MW wind turbine and the NREL 5MW baseline turbine. In addition, a Norwegian site is chosen as a reference site and three operational load cases and one survival load case has been selected.

In Chapter 4 the initial design of a pontoon-type semi-submersible platform is presented. The design is first made though upscaling of an existing 5MW semi-submersible platform design. The design is then checked against buoyancy, stability, hydrodynamic and strength criteria. In addition, a sensitivity analysis of main dimensions of the platform has been performed.

In Chapter 5 the mesh of the semi-submersible platform has been redesigned together with a new free surface mesh in order to obtain the second order difference quadratic transfer functions. Characteristics of the mean drift forces has been studied. Besides, a mesh convergence study has been performed.

In Chapter 6 the preliminary mooring system design is presented. Free decay test, load-displacement test has been performed to determine the characteristic of the mooring system. In addition, an extreme condition test with ULS check has also been performed.

In Chapter 7 the SIMO-RIFLEX-AeroDyn model is presented, extensive tests have been performed to check the model. Coupled dynamic analysis has been performed for the floating wind turbine system under different load conditions. Characteristic responses of the semi-submersible floating wind turbine are studied and compared to those of the land-based wind turbine. In addition, influence of second order wave force has been studied.

In Chapter 8 Conclusions of the thesis work and recommendations for future work have been made.

*Note: work presented in Chapter 4 was carried out during the specialized project TMR4590 at NTNU, which should be excluded for the master thesis TMR5950 at NTNU. While all the work together forms the complete thesis project (graduation package) at TU Delft.

Chapter 2

Theory

2.1 Wind Turbine Aerodynamics

Aerodynamic models for wind turbines range from the very simple 1D momentum theory to 3D Navier-Stokes solutions. Hansen [55] has provided a review of popular wind turbine aerodynamic models, who pointed out that blade element momentum (BEM) is still the most widely used method. As has been discussed in Section 1.4, currently most of the available coupled dynamic simulation codes for floating wind turbines are based on BEM to calculate aerodynamic loads including the SIMO-REFLEX-AeroDyn (SRA) code that will be used in this thesis. Therefore, in this section, the theory of BEM method will be introduced.

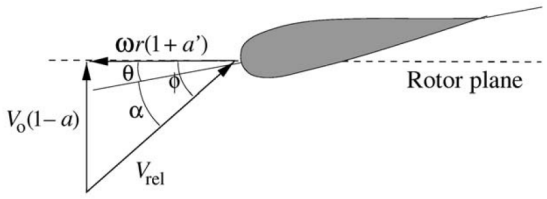

Figure 2.1: *Local flow past a section of wind turbine blade showing the construction of relative velocity and angle of attack (Ref [56])*

As shown in Figure 2.1, an airfoil section with local twist angle of θ (original section twist angle plus blade pitch angle) and distance of r to the center of rotation is rotating with angular velocity ω. The wind velocity V_0 is perpendicular to the rotor plane. The lift and drag coefficients are [56]:

$$C_L(\alpha) = \frac{f_L}{0.5\rho V_{rel}^2 c}, \quad C_D(\alpha) = \frac{f_D}{0.5\rho V_{rel}^2 c} \tag{2.1}$$

where f_L and f_D are lift and drag loads on the section respectively, ρ is air density, c is chord length of the section, V_{rel} is relative wind velocity, ϕ is the flow angle and α is the

angle of attack which is defined as:

$$\alpha = \phi - \theta \tag{2.2}$$

$$\tan\phi = \frac{V_0}{\omega r}\frac{1-a}{1+a'} \tag{2.3}$$

where a and a' are axial and rotational induction factors respectively, given by:

$$a = \left[1 + \frac{4\sin^2\phi}{\sigma C_n}\right]^{-1} \quad a' = \left[-1 + \frac{4\sin\phi\cos\phi}{\sigma C_t}\right]^{-1} \tag{2.4}$$

with solidity σ, normal force coefficient $C_n = C_L\cos\phi - C_D\sin\phi$ and tangential force coefficient $C_t = C_L\sin\phi - C_D\cos\phi$. The above derivation serves as the classic BEM method. Several corrections are important to make the method more reliable. These include the Prandtl's tip loss correction factor, which is a correction of the assumption of infinite number of blades during the derivation of above equations. Another correction is the Glauert factor which corrects that the momentum theory is not valid for large values of thrust coefficient. These corrections will slightly change the expression of Equation (2.4), which could be found in Ref [56].

The general procedure for the BEM method is to start with an initial estimation of a and a', then calculate the angle of attack α by Equation (2.3) and (2.2) and search for the corresponding aerodynamic coefficients C_L and C_D from a previous stored lookup table, which could be obtained from experiments or numerical simulations. Then update the value of a and a' using expression of Equation (2.4) with proper corrections. The procedure will have to iterate until equilibrium of the induced velocities is reached before moving to the next time step.

In order to apply the method to a floating wind turbine, the motion of the platform and the deformation of the tower and blades should also be taken into account. One will need to update Equation (2.3) to include these effects. A similar procedure of aerodynamic loads calculation for fixed wind turbines can be found in the AeroDyn Theory Manual [57]. Besides, the coupling of aerodynamic analysis to structural and hydrodynamic analysis in the SIMO-RIFLEX-AeroDyn code will be presented later.

2.2 Linear Floater Hydrodynamics

Most of the calculations and analysis in this project are based on potential theory. Details for the potential theory could be found through any fluid mechanics fundamental books, such as the one from Prof. White [58]. Reference is also made to Prof. Faltinsen [25] to clarify the problem.

2.2.1 Governing Equations

The basic assumptions for potential flow theory are that the fluid is inviscid, irrotational and incompressible. Combining these assumptions with linear theory, the linear wave

body interaction problem simplifies to find the velocity potential ϕ. Referring to Figure 2.2, where $\boldsymbol{n}$ is the normal vector pointing into the fluid, S_{0FS} is mean free surface, S_{SB} is seabed surface, S_{0B} is mean body wetted surface, Ω_0 is the mean fluid volume and $\boldsymbol{V_B}$ is body velocity:

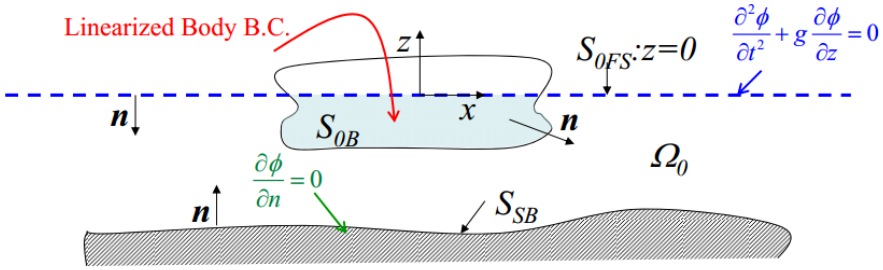

Figure 2.2: *Linear wave body interaction problem [59]*

Governing equation:

$$\nabla^2\phi = 0 \qquad \text{in } \Omega_0 \tag{2.5}$$

Sea bottom boundary condition:

$$\frac{\partial\phi}{\partial n} = 0 \qquad \text{on } S_{SB} \tag{2.6}$$

Body boundary condition:

$$\frac{\partial\phi}{\partial n} = \boldsymbol{V_B}\cdot\boldsymbol{n} \qquad \text{on } S_{0B} \tag{2.7}$$

Combined free surface condition:

$$\frac{\partial^2\phi}{\partial t^2} + g\frac{\partial\phi}{\partial z} = 0 \qquad \text{on } z = 0 \tag{2.8}$$

Equation (2.5) to (2.8) together with a far field condition that the waves are outgoing form the whole system of governing equation for the linear fluid structure interaction problem, which serves as the basis for frequency domain analysis.

2.2.2 Equations of Motion

According to Newtons second law, the equations of motion for the structure could be written as:

$$\sum_{k=1}^{6} M_{jk}\ddot{\eta}_k(t) = F_j(t) \qquad j = 1,\ldots,6 \tag{2.9}$$

where M_{jk} is one component of the mass matrix $\boldsymbol{M}$, $\ddot{\eta}_k$ is one component of the body acceleration vector $\ddot{\boldsymbol{\eta}}$ and F_j is one component of the force vector $\boldsymbol{F}$, j indicates the degree of freedom. The external load could be calculated by pressure integrating, combining with the linear Bernoulli equation, with the dynamic pressure being integrated on the mean

body surface S_{0B} and the static pressure being integrated on the instantaneous body surface S_B, we have:

$$F_j(t) = \int\limits_{S_{0B}} -\rho \frac{\partial \phi}{\partial t} \mathbf{n} dS + \int\limits_{S_B} -\rho g z \mathbf{n} dS \qquad j = 1, \ldots, 6 \tag{2.10}$$

The linear wave body interaction problem could be split into two sub-problems [25]:

- Diffraction problem, when the body is fixed and interacting with incident waves;
- Radiation problem, the body is forced to oscillate in its six dofs, no incident waves.

Using linear theory, the velocity potential ϕ in Equation (2.10) could be written as:

$$\phi(x, y, z, t) = \underbrace{\phi_0(x, y, z, t)}_{incident\ wave} + \underbrace{\phi_D(x, y, z, t)}_{diffraction} + \underbrace{\phi_R(x, y, z, t)}_{radiation} \tag{2.11}$$

The diffraction problem is involved with ϕ_0 and ϕ_D, the integration of which gives the wave excitation loads. The radiation problem is involved with ϕ_R and hydrostatic pressure, the integration of which gives the added mass, potential damping and restoring force.

Introduce the following equation:

$$\phi_R(x, y, z, t) = \Re \left\{ \sum_{k=1}^{6} \dot{\eta}_k \varphi_k(x, y, z) \right\} \tag{2.12}$$

where $\varphi_k(x, y, z)$ is the complex spatial velocity potential for the body oscillating with unitary speed in the kth dof. Then, it can be shown that Equation (2.10) could be rewritten into:

$$F_j(t) = \sum_{k=1}^{6} F_j^{exc}(t) - A_{jk} \ddot{\eta}_k(t) - B_{jk} \dot{\eta}_k(t) - C_{jk} \eta_k \qquad j = 1, \ldots, 6 \tag{2.13}$$

where A_{jk} is the added mass coefficient, B_{jk} is the potential damping coefficient and C_{jk} is the linear restoring coefficient:

$$A_{jk} = \Re \left[\rho \int\limits_{S_{0B}} \varphi_k n_j dS \right] \quad and \quad B_{jk} = -\omega \Im \left[\rho \int\limits_{S_{0B}} \varphi_k n_j dS \right] \tag{2.14}$$

Then, the equations of motion for the linear wave structure interaction problem could be rewritten as:

$$\sum_{k=1}^{6} \left(M_{jk} + A_{jk}(\omega) \right) \ddot{\eta}_k(t) + B_{jk}(\omega) \dot{\eta}_k(t) + C_{jk} \eta_k(t) \ = F_j^{exc}(t) \qquad j = 1, \ldots, 6 \tag{2.15}$$

Written in to matrix form:

$$\left(\boldsymbol{M} + \boldsymbol{A}(\omega) \right) \ddot{\boldsymbol{\eta}} + \boldsymbol{B}(\omega) \dot{\boldsymbol{\eta}} + \boldsymbol{C} \boldsymbol{\eta} = \boldsymbol{F} \tag{2.16}$$

In a linear system at steady state condition, the response oscillates with the frequency of the excitation and the amplitude of response is proportional to the excitation.

Therefore, it reasonable to assume the excitation loads $\boldsymbol{F}$ is proportional to the incident wave amplitude ξ_a and oscillate with frequency ω, written into complex form:

$$\boldsymbol{F}(t) = \Re\left\{\xi_a \boldsymbol{X}(\omega, \beta) e^{i\omega t}\right\} \tag{2.17}$$

Then the response could also be written into complex form:

$$\boldsymbol{\eta}(t) = \Re\left\{\boldsymbol{\eta}_a(\omega) e^{i\omega t}\right\} \tag{2.18}$$

Substitute Equation (2.17) and (2.18) into Equation (2.16) and avoid the time dependence, we have the equation of motion in frequency domain:

$$\left(-\omega^2 (\boldsymbol{M} + \boldsymbol{A}(\omega)) + i\omega \boldsymbol{B}(\omega) + \boldsymbol{C}\right) \boldsymbol{\eta}_a(\omega) = \xi_a \boldsymbol{X}(\omega, \beta) \tag{2.19}$$

The response amplitude operator (RAO) is then defined as following:

$$RAO = |\boldsymbol{H}(\omega, \beta)| = |\boldsymbol{\eta}_a(\omega)/\xi_a| = \left|\left[-\omega^2 (\boldsymbol{M} + \boldsymbol{A}(\omega)) + i\omega \boldsymbol{B}(\omega) + \boldsymbol{C}\right]^{-1} \boldsymbol{X}(\omega, \beta)\right| \tag{2.20}$$

2.2.3 Eigenvalue Analysis

For an undamped system with no excitation loads, Equation (2.19) could be simplified into the eigenvalue problem:

$$\left(-\omega^2 (\boldsymbol{M} + \boldsymbol{A}(\omega)) + \boldsymbol{C}\right) \boldsymbol{\eta}_a = 0 \tag{2.21}$$

Eigenfreqency for the six degree of freedom could be obtained by setting:

$$\det\left(-\omega^2 (\boldsymbol{M} + \boldsymbol{A}(\omega)) + \boldsymbol{C}\right) = 0 \tag{2.22}$$

The explicit expression for natural frequencies of the six dofs:

$$\omega_{nj} = \sqrt{\frac{C_{jj}}{M_{jj} + A_{jj}(\omega)}} \qquad j = 1, \ldots, 6 \tag{2.23}$$

2.2.4 Viscous Damping

The damping term in equation of motion (2.16) only includes the potential damping, which is associated with the wave generation ability. For the case of long waves, the wave generated by the wave structure interaction is small, which means the potential damping associated with long waves is small. Then large amplification of the motion will be expected at resonance as shown by Equation (2.20). In that case, as shown in Figure 2.3, viscous forces will become important.

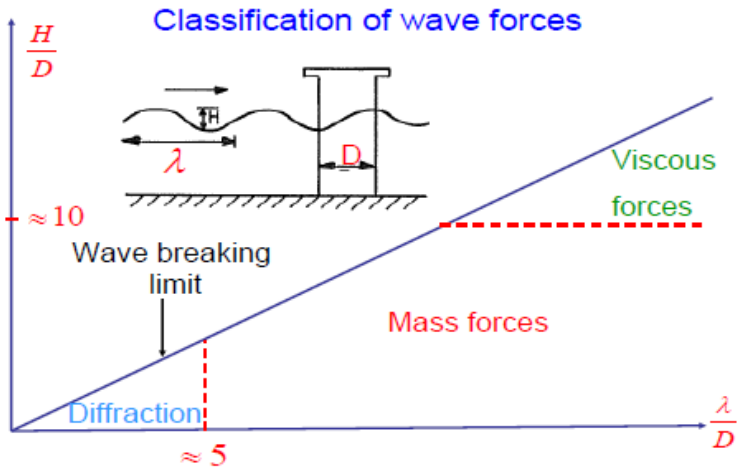

Figure 2.3: *Classification of wave forces [25]*

One main source of viscous damping is the drag force acting on the structure which is neglected by potential theory. According to Morison's equation, the drag force for a fixed cylinder with a diameter of D could be written as:

$$dF_{drag} = \frac{1}{2}\rho C_D D \left|u - \dot{\eta}\right| (u - \dot{\eta}) \tag{2.24}$$

It is seen that the drag force is a quadratic function of the relative velocity of the wave particle u and the structure $\dot{\eta}$. Therefore, linearization is needed before it could be used into the frequency domain analysis.

Linearization of the drag force

Assuming a regular wave with velocity:

$$u = u_a \sin(\omega t) \tag{2.25}$$

Then the response of the structure will be harmonic, but could be not in phase with the wave velocity:

$$\eta = \eta_1 \cos(\omega t) + \eta_2 \sin(\omega t) \tag{2.26}$$

The relative velocity can be written as:

$$u_r = u - \dot{\eta} = A \cos(\omega t + \phi) \tag{2.27}$$

where A is given by:

$$A = \sqrt{(u - \omega\eta_2)^2 + (\omega\eta_1)^2} \tag{2.28}$$

Neglecting the phase angle in Equation (2.27), the nonlinear drag force can be written as:

$$dF_{drag,NL} = \frac{1}{2}\rho C_D D A^2 \left|\cos(\omega t)\right| \cos(\omega t) \tag{2.29}$$

Assuming the linearized drag force has the following form, with a coefficient K_L:

$$dF_{drag,L} = \frac{1}{2}\rho C_D D K_L A \cos(\omega t) \tag{2.30}$$

The coefficient K_L can be found by setting work done by drag force over one period equal:

$$\int_0^T \left(dF_{drag,L} - dF_{drag,NL}\right) u_r dt = 0 \tag{2.31}$$

Solving the above equation, K_L could be obtained:

$$K_L = \frac{A\int_0^T |\cos(\omega t)| \cos(\omega t)^2 dt}{\int_0^T \cos(\omega t)^2 dt} = \frac{8A}{3\pi} \tag{2.32}$$

Then the linearized drag force is given by:

$$dF_{drag,L} = \frac{4\rho C_D D A}{3\pi}(u - \dot{\eta}) \tag{2.33}$$

The term related to the structure velocity can then be written to the left side of the equation of motion, which served as the linearized viscous damping term. Therefore, the viscous damping coefficient from linearized drag force is:

$$B_{visous} = \frac{4\rho C_D D A}{3\pi} \tag{2.34}$$

Where A is given by Equation (2.26), which depends on the motion of the structure. Therefore, the procedure to determine the linearized damping coefficient should be found iteratively.

2.3 Second Order Floater Hydrodynamics

For first order solutions, the loads/motions have zero mean value and oscillate with the frequency of the incident waves. When it comes to loads/motions of a semi-submersible platform, the slow drift motions caused by slowly-varying (slow drift) loads connected with second order difference frequency effect and mean drift effect become importance.

2.3.1 Method for Force Calculation

The force on a marine structure can be estimated in two ways: direct pressure integration and conservation of fluid momentum.

Direct pressure integration

The force is obtained by integrating the pressure along the instantaneous wetted surface S_B of the body:

$$\boldsymbol{F} = \int\limits_{S_B} p\boldsymbol{n}dS \tag{2.35}$$

where the expression of pressure up to the 2nd order is:

$$p = -\rho g z - \rho\frac{\partial\phi^{(1)}}{\partial t} - \rho\frac{\partial\phi^{(2)}}{\partial t} - \frac{1}{2}\rho\nabla\phi^{(1)}\cdot\nabla\phi^{(1)} \tag{2.36}$$

where $^{(1)}$ indicates the first order quantity and $^{(2)}$ indicates the second order quantity.

Conservation of fluid momentum

The force is obtained by solving the equation of fluid moment conservation inside a fluid control volume Ω:

$$\boldsymbol{F} = -\frac{d}{dt}\left(\int\limits_{\Omega}\rho\boldsymbol{V}d\Omega\right) - \int\limits_{S-S_B} p\boldsymbol{n}dS - \int\limits_{\Omega}\rho g\boldsymbol{k}d\Omega - \int\limits_{S}\rho\boldsymbol{V}(V_n - U_n)dS \tag{2.37}$$

The second method is generally more complicated than the first one. But in the case of horizontal mean drift force calculation, the expression (2.37) can be reduced to an integral on a far-field control surface that can be estimated more simply and correctly than direct pressure integration.

2.3.2 Low Frequency Second Order Force

Following Pinkster [60], the low frequency second order force can be written as a summation of five different components by direct pressure integration, where $\boldsymbol{R}$ is the rotation transformation matrix:

$$\begin{aligned}\boldsymbol{F}^{(2)} = &\underbrace{\oint\limits_{WL}\frac{1}{2}\rho g\left(\xi_r^{(1)}\right)^2\cdot\boldsymbol{n}\cdot dl}_{I} \underbrace{-\int\limits_{S_{0B}}\frac{1}{2}\rho\left(\nabla\phi^{(1)}\right)^2\cdot\boldsymbol{n}\cdot dS}_{II}\\ &\underbrace{-\int\limits_{S_{0B}}\rho\boldsymbol{\eta}^{(1)}\cdot\nabla\frac{\partial\phi^{(1)}}{\partial t}\cdot\boldsymbol{n}\cdot dS}_{III}\underbrace{-\boldsymbol{M}\cdot\boldsymbol{R}^{(1)}\cdot\ddot{\boldsymbol{\eta}}_G^{(1)}}_{IV}\\ &\underbrace{-\int\limits_{S_{0B}}\rho\frac{\partial\phi^{(2)}}{\partial t}\cdot\boldsymbol{n}\cdot dS}_{V}\end{aligned} \tag{2.38}$$

The contributions can be split into five components:

(I) First order wave relative elevation

(II) Pressure drop due to first order velocity

(III) Pressure due to product of gradient of first order pressure and first order motion

(IV) Contribution due to first order angular motions and inertia forces

(V) Contribution due to second order potentials

Components I to IV represent quadratic contributions of the first order solutions, which could be solved with the solution of first order problem. Component V is the contribution from second order potential, which is the most difficult part to compute. One of the consequences of this is the requirement to satisfy the second order free surface boundary condition, which requires an additional free surface mesh to solve the problem numerically.

The force represented by Equation (2.38) could also be written as:

$$F_j^{(2)} = \Re\left\{\sum_m \sum_n \xi_m \xi_n T_{mn}^j(\omega_m, \omega_n) e^{-i(\omega_m - \omega_n)t + (\varepsilon_m - \varepsilon_n)}\right\} \tag{2.39}$$

The function $T_{mn}^j(\omega_m, \omega_n)$ represents the complex difference frequency second order transfer function, known as the quadratic transfer function (QTF). It should be noted that the diagonal terms of the QTF corresponds to the mean-drift force.

Due to the difficulty in calculating the QTFs, some approximations has been proposed, mainly aiming to avoid the computation of the second order velocity potential $\phi^{(2)}$. One of the most widely used methods is Newman's approximation [61], which could be used to derive the QTF matrix based only on the mean drift forces which is depended only on first order solutions:

$$T_{mn}^{ic} = T_{nm}^{ic} = \frac{1}{2}\left(T_{mm}^{ic} + T_{nn}^{ic}\right) \tag{2.40}$$

$$T_{mn}^{is} = -T_{nm}^{is} = 0 \tag{2.41}$$

By using the Newman's approximation with geometric average and by introducing a sum frequency term into Equation (2.39), the expression could be further simplified [25]:

$$F_j^{(2)} = 2\left[\sum_{m=1}^{N} \xi_m \sqrt{T_{mm}^{ic}} \cos\left(w_m t + \varepsilon_j\right)\right]^2 \tag{2.42}$$

With the mean drift force transfer function being estimated either by direct pressure integration in 6-dofs or more simply by conservation of fluid momentum in the horizontal 3-dofs.

The Newman's approximation is good if the frequency difference is small [62], which is usually the case for horizontal motions of offshore structure in deep water, which normally have natural periods above 100s. For the case of shallower water or for the case of heave motion, which might be interesting for a semi-submersible floating wind turbine, the reliability in the application of Newmans approximation is uncertain.

2.4 Coupled Dynamic Analysis

In this thesis, coupled aero-hydro-servo-elastic dynamic response analysis of a catenary moored semi-submersible floating wind turbine is performed using the SIMO-RIFLEX-AeroDyn code. The blades, tower and mooring lines are modeled using nonlinear finite beam elements in RIFLEX. In the coupled analysis, the complete system of equations including the rigid body model of the floater and slender body models of blades, tower and mooring lines are solved simultaneously in time domain. Dynamic equilibrium of the system is achieved at each time step.

2.4.1 Equation of Motion in Time Domain

According to potential flow theory, the equations of motion of a floating platform can be written into the following form: (Note, this equation is the same as Equation (2.16), which is reproduced for the consistency of reading)

$$\left(\boldsymbol{M} + \boldsymbol{A}(\omega)\right)\ddot{\boldsymbol{\eta}} + \boldsymbol{B}(\omega)\dot{\boldsymbol{\eta}} + \boldsymbol{C}\boldsymbol{\eta} = \boldsymbol{F} \tag{2.43}$$

The most frequently used method for solving Equation (2.43) is the convolution integral, which will be introduced here [63]. Consider the radiation part of the problem (frequency dependent coefficients only):

$$\boldsymbol{RF}(t) = \boldsymbol{A}(\omega)\ddot{\boldsymbol{\eta}} + \boldsymbol{B}(\omega)\dot{\boldsymbol{\eta}} \tag{2.44}$$

Assuming that the right term varies sinusoidally at one frequency only, Equation (2.44) can be written into frequency domain:

$$\boldsymbol{RF}(\omega) = \left(-\omega^2\boldsymbol{A}(\omega) + i\omega\boldsymbol{B}(\omega)\right)\boldsymbol{\eta}_a(\omega) \tag{2.45}$$

Using the following relation:

$$\begin{aligned} \boldsymbol{A}(\omega) &= \boldsymbol{A}_\infty + \boldsymbol{a}(\omega), \quad \boldsymbol{A}_\infty = \boldsymbol{A}(\omega = \infty) \\ \boldsymbol{B}(\omega) &= \boldsymbol{B}_\infty + \boldsymbol{b}(\omega), \quad \boldsymbol{B}_\infty = \boldsymbol{B}(\omega = \infty) = 0 \end{aligned} \tag{2.46}$$

Equation (2.45) can be written into:

$$\boldsymbol{RF}(\omega) = -\omega^2\boldsymbol{A}_\infty\boldsymbol{\eta}_a(\omega) + \left(i\omega\boldsymbol{a}(\omega) + \boldsymbol{b}(\omega)\right)i\omega\boldsymbol{\eta}_a(\omega) \tag{2.47}$$

Applying the inverse Fourier transformation:

$$\boldsymbol{RF}(t) = \boldsymbol{A}_\infty\ddot{\boldsymbol{\eta}}(t) + \int_{-\infty}^{\infty}\boldsymbol{h}(t-\tau)\dot{\boldsymbol{\eta}}(\tau)d\tau \tag{2.48}$$

Physically, $\boldsymbol{h}(t-\tau) = \boldsymbol{0}$ for $t < 0$. And causality implies that $\boldsymbol{h}(t-\tau) = \boldsymbol{0}$ for $\tau > t$. So Equation (2.48) can be rewritten into:

$$\boldsymbol{RF}(t) = \boldsymbol{A}_\infty \ddot{\boldsymbol{\eta}}(t) + \int_0^t \boldsymbol{h}(t-\tau)\dot{\boldsymbol{\eta}}(\tau)d\tau \tag{2.49}$$

Substituting Equation (2.49) into Equation (2.43), we obtain the equation of motion in time domain:

$$(\boldsymbol{M} + \boldsymbol{A}_\infty)\,\ddot{\boldsymbol{\eta}} + \boldsymbol{C}\boldsymbol{\eta} + \int_0^t \boldsymbol{h}(t-\tau)\dot{\boldsymbol{\eta}}(\tau)d\tau = \boldsymbol{F} \tag{2.50}$$

where the retardation function $\boldsymbol{h}(\tau)$ is computed by a transform of the frequency dependent added mass and potential damping:

$$\boldsymbol{h}(\tau) = \frac{1}{2\pi}\int_{-\infty}^{\infty} (\boldsymbol{b}(\omega) + i\omega\boldsymbol{a}(\omega))\, e^{i\omega t}d\omega \tag{2.51}$$

Using $\boldsymbol{b}(\omega) = \boldsymbol{b}(-\omega)$ and $\boldsymbol{a}(\omega) = \boldsymbol{a}(-\omega)$:

$$\boldsymbol{h}(\tau) = \frac{1}{\pi}\int_0^{\infty} (\boldsymbol{b}(\omega)\cos(\omega\tau) - \omega\boldsymbol{a}(\omega)\sin(\omega\tau))\, d\omega \tag{2.52}$$

From causality $\boldsymbol{h}(\tau) = \boldsymbol{0}$ for $\tau < 0$; the process can not have any memory effect of the future. This means the two parts in the integral must be opposite for $\tau < 0$ and identical for $\tau > 0$, or mathematically:

$$\boldsymbol{h}(\tau) = \frac{2}{\pi}\int_0^{\infty} \boldsymbol{b}(\omega)\cos(\omega\tau)d\omega = -\frac{2}{\pi}\int_0^{\infty} \omega\boldsymbol{a}(\omega)\sin(\omega\tau)d\omega \tag{2.53}$$

Based on Equation (2.53), the retardation function can be found using either by frequency dependent potential damping coefficients or added mass coefficients.

2.4.2 Solution Technique

In order to form Equation (2.50), the force vector $\boldsymbol{F}$ needs to be determined:

$$\boldsymbol{F} = \boldsymbol{F^{(1)}} + \boldsymbol{F^{(2)}} + \boldsymbol{F}_{drag} + \boldsymbol{F}_{mooring} + \boldsymbol{F}_{wind} \tag{2.54}$$

The first order wave excitation loads $\boldsymbol{F}^{(1)}$ can be found based on Panel Method in HydroD [64]. HydroD solves the potential flow problem using the Wadam solver. The second order wave loads $\boldsymbol{F}^{(2)}$ can also be obtained in HydroD by solving the QTF functions with a free surface model. These wave loads are transformed into first order and second order transfer functions in SIMO. The nonlinear quadratic drag force can also be added

to the equations of motion by using Morison elements in SIMO. The relative velocity of water particles and the platform motion are considered for calculating the viscous forces. The mooring line force (calculated in RIFLEX) as well as the wind forces (Calculated in AeroDyn) are added to the right hand of the equation of motion at each time step.

The solution of Equation (2.50) in the time domain is based on an incremental procedure [65] using the dynamic time integration scheme, according to Newmark β family methods. The Newton-Raphson iteration is used to assure equilibrium between internal and external forces at every time step. The coupling between SIMO, RIFELX and AeroDyn in the integrated dynamic analysis is discussed in details in Chapter 7.

Chapter 3

Wind Turbine and Site Condition

3.1 The 10MW Reference Wind Turbine

3.1.1 Brief Introduction

Using a bigger turbine is one of the most effective ways to reduce the cost of energy of offshore wind turbines.

At the time of the thesis, there are two available 10 MW reference turbines (RWT), one is the DTU 10MW reference wind turbine developed by the department of Wind Energy at Technical University of Denmark (DTU), the other is the NOWITECH 10MW reference wind turbine developed by Norwegian University of Science and Technology (NTNU) and Marintek through the Norwegian Research Center for Offshore Wind Technology (NOWITECH). They are shown in Figure 3.1 below.

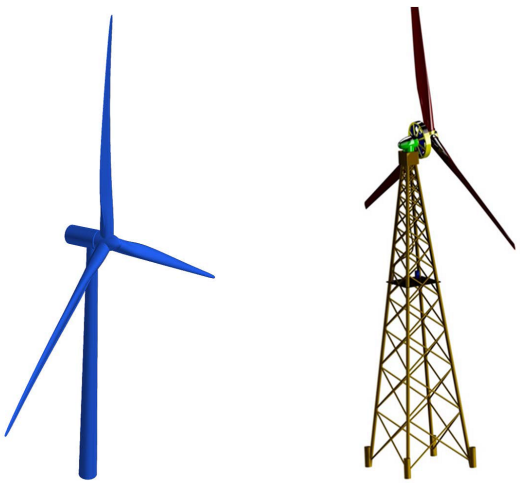

Figure 3.1: *The DTU 10MW RWT (left) and the NOWITECH 10MW RWT (right)*

Information of the DTU 10MW reference wind turbine can be found from the work of DTU Wind Energy [66]. General information regarding the NOWITECH 10MW wind turbine is provided by Dr. Merz, K.O. [67].

3.1.2 Comparison of General Properties

A general comparison between the DTU 10MW RWT and NOWITECH 10MW RWT are shown in Table 3.1. The information for the NREL 5MW RWT [17] developed by National Renewable Energy Laboratory is also included in the table, which is currently widely used in research. The NREL 5MW RWT also serves as the reference turbine for the upscaling of the DTU 10MW RWT.

Table 3.1: *Comparison between properties of DTU 10MW RWT, NOWITECH 10MW RWT and the NREL 5MW RWT*

Description	DTU 10MW	NOWITECH	NREL 5MW
General info			
Rating	10 MW	10 MW	5 MW
Configuration	Upwind, 3 blades	Upwind, 3 blades	Upwind, 3blades
Control	Collective pitch	Collective pitch	Collective pitch
Drivetrain	Multiple stage gearbox	Direct Drive	Multiple stage gearbox
Rated wind speed	11.4 m/s	13.25 m/s	11.4 m/s
Cut-in, Cut-out wind speed	4 m/s, 25 m/s	4 m/s, 30 m/s	3m/s, 25 m/s
Cut-in, Rated rotor speed	6 rpm, 9.6 rpm	5 rpm, 12.2 rpm	6.9 rpm, 12.1 rpm
Rated tip speed	90 m/s	90 m/s	80 m/s
Maximum Thrust	1500 kN	–	∼750 kN [68]
Geometry info			
Rotor, Hub diameter	178.3 m, 5.6 m	141.0 m, 5 m	126 m, 3m
Hub height	119 m	93.5 m	90 m
Tower height	115.63 m	–	87.6 m
Overhang, Shaft tilt	7.1 m, 5°	7 m [69], 5°	5m, 5°
Pre-cone	−2.5°	−2°	−2.5°
Mass			
Rotor mass	230.7 t	168.5 t	110 t
Nacelle mass	446.0 t	–	240 t
Tower mass	628.4 t	–	347.5 t
Total mass	1305.1 t	–	697.5 t
Overall CM[1]	(-0.3 m, 0 m, 85.5 m)	–	(-0.2 m, 0 m, 64.0 m)

It could be seen from Table 3.1 that the DTU 10MW RWT is mainly an upscaled NREL 5MW RWT with the same rated wind speed and an upscaled rotor. While the NOWITECH RWT applies a higher rated wind speed with shorter blades to achieve the rated power output.

Since there is no sufficient data about mass properties of the NOWITECH 10MW RWT, and the lattice tower designed for the NOWITECH RWT is not considered to be used in the floating structure in this project, the DTU 10MW RWT is therefore adopted in this project.

[1] Based on the tower coordinate system according to GL standards [70]

The corresponding power and thrust curves for DTU 10MW RWT are shown in Figure 3.2.

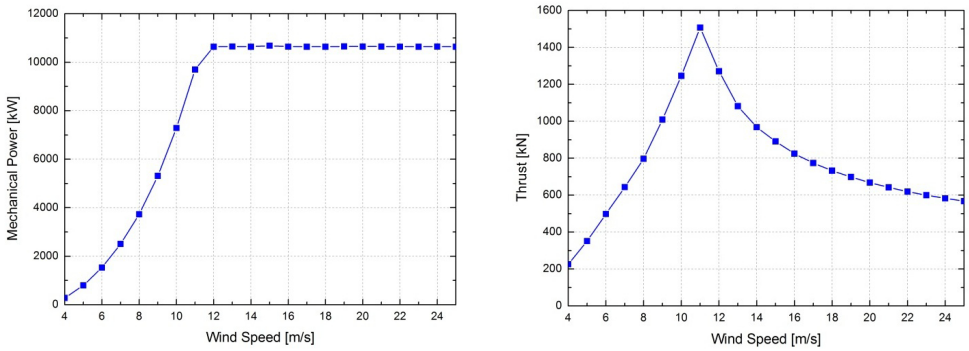

Figure 3.2: *Power and thrust curves of DTU 10MW RWT based on BEM method(Based on Ref [66])*

3.1.3 Tower of the DTU 10MW RWT

Tower property

The properties of tower for the DTU 10MW RWT is provided by DTU Wind Energy [66]. Some of the important aspectes are re-emphasized here.

The tubular tower is made from steel S355, as defined in the European standard DIN EN 10025-2. Material parameters are given in Table 3.2. For the calculation of the cross section mass properties the mass density was increased by approximately 8% (8500kg/m3) in order to account for the mass of secondary structures.

Table 3.2: *General properties of the DTU 10MW wind turbine tower*

Young's Elasticity Modulus	2.10E+11	Pa
Poisson's ratio	0.3	[-]
Effective Density	8500	kg/m^3
Structural Damping ratio(All modes)	6.28	%

The outer diameter of the tower varies linearly from $D = 8.3m$ at the bottom ($h = 0m$) to $D = 5.5m$ at the top ($h = 115.63m$). The tower was divided into 10 sections, where the wall thickness is constant in each section.

Special consideration of tower

It might be impractical to maintain the tower stiffness for the floating wind turbine design, as pointed out in the DNV standards [12], since the tower is designed and approved to be connected to a fixed foundation. Even when the mass and stiffness distributions over the height are kept the same as for the tower for an onshore wind turbine, the eigenfrequencies of the tower are altered when it is mounted on a floater due to more flexible support. If one would like to keep the eigenfrequencies of the tower unchanged, the tower should be made more flexible when it is supported by a floater.

Besides, due to the higher wind speed offshore, an offshore wind turbine in general requires a lower hub height than an onshore wind turbine to achieve the same power performance.

However, in this thesis, the tower for the floating wind turbine is taken identical to the one provided above without any modifications.

3.2 Site Condition

The Norway 5 site has been selected as a representative site for floating wind turbine, as shown in Figure 3.3. A generic water depth of 200m is used for this site.

Figure 3.3: *Location of the Norway 5 site (No.14 in the map, based on [21])*

The wind and wave data at the site has been fitted with analytical joint distributions by Li [21]. Therefore, it is possible to use the following procedure to choose operational loads cases:

1. First a mean wind speed at hub height is selected. Then the mean wind speed is transformed to reference height of 10m by applying a power law. It is also shown by Li that a power law profile with the exponent equal to 0.1 should be used for the present site.

2. Then the conditional distribution of significant wave height for given mean wind speed is applied, and the most probable value[2] of significant wave height is selected.

3. Finally, the conditional distribution of wave peak period for given significant wave height and mean wind speed is applied, and the most probable value of wave peak period is selected.

Three operational conditions covering below-rated, rated and above-rated wind speeds has been selected according to the above procedure. In addition, one extreme (parked) condition is also selected. The results are shown in Table 3.3. The extreme condition with a return period of 50 years is obtained by using the contour surface method [21].

[2]The value that is corresponding to the peak of the probability density function

The selected condition corresponds to maximum significant wave height on the contour line.

Turbulence intensity is defined at the IEC standard [71] as a function of mean wind speed, class C is used for offshore condition. Normal Turbulence Model (NTM) is used for operating cases while Extreme Wind Model (EWM) is used for parked condition. For all load cases, a power law is used for the wind speed profile as discussed above.

The operational case is the general power production case in which the blades are rotating and the control is active. The parked (idling) case is a nonoperational case in which the blades are pitched to feather and the turbine is shut down to avoid damage in extreme conditions. In the present thesis, the nacelle yaw angle is kept to be 0 degree in all cases.

Table 3.3: *Load cases for operational and extreme condition*

Load case number	Mean wind speed at hub height	Significant wave height	Wave peak period	Turbulence intensity	Turbine status
	[m/s]	[m]	[s]	[-]	
OP1	8	2	10.3	0.17	Operating
OP2	11.4	2.5	10.2	0.15	Operating
OP3	18	4.1	10.5	0.13	Operating
EX	40	15.6	14.5	0.11	Parked

Chapter 4

Initial Design

4.1 Design Requirements and Procedure

4.1.1 Standards

There is only one standard specific to floating wind turbine design, the recently released DNV standard - Design of Floating Wind Turbine Structures as a result of a joint industry project. In addition, the new version of GL standards also has a section related to floating wind turbines. Besides, there are several standards related to offshore fixed wind turbine that are widely used. In the initial design, the new DNV standard on floating wind turbine is frequently used.

1. Floating offshore wind turbine

    - DNV-OS-J103 Design of Floating Wind Turbine Structures, Det Norsk Veritas, June 2013
    - Guideline for the Certification of Offshore Wind Turbines, Germanischer Lloyd, 2012

2. Fixed offshore wind turbine

    - DNV-OSJ101 Design of Offshore Wind Turbine Structure, Det Norsk Veritas, January 2013
    - Guideline for the Certification of Offshore Wind Turbines, Germanischer Lloyd, 2012
    - IEC 61400-3. Wind turbines - Part 3: Design requirements for offshore wind turbines, International Electrotechnical Commission, 2009

4.1.2 Design Requirements

Although there exist several standards that could be used for the design of a new floating wind turbine platform, actually no detailed guidelines are provided for the design of the platform. Therefore, most of the work done in the project is based on general guidelines and experience on design of semi-submersible platform for oil & gas industry.

In order to achieve a proper initial design that could be adopted in time domain coupled dynamic analysis in the future, several requirements should be fulfilled.

General Requirements

In this thesis work, a semi-submersible floater should be designed to support this 10MW wind turbine. The semi-submersible will consist of one central column supporting the wind turbine and three side columns connected to the central column by three pontoons. There will be no braces considered in this concept. The semi-submersible will be made of steel with a proper distribution of water ballast.

This braceless concept offers a steel reduction result and avoids complex fabrication work as well as the fatigue issue with braces-platform connections.

Buoyancy

The buoyancy requirement requires that the floater could provide enough displacement to support the weight of the floating system at designed draft level. A proper ballast design should also be performed to achieve the desired draft.

Stability

There are two main challenges regarding stability of the floater due to the presence of the turbine:

1. The wind turbine will raise the center of gravity of the whole structure due to its large top mass (rotor and nacelle) high above the sea level.
2. The large aerodynamic thrust acting high above the sea level will introduce a very large overturning moment. Normally the thrust became largest when the turbine is operating at rated power output.

Both of the two items challenge the basic naval architecture principles to achieve stability.

Besides, wind turbines are usually designed to operate on a vertical tower. A large heeling angle of the platform means a big change of the projected rotor plane area to the wind as well as a big change of the angle of attach for all the blades sections, which might in turn result in a reduction of power output.

The DNV standard [12] provides stability requirements for general semi-submersible platforms, which are:

- The area under the righting moment curve to the angle of downflooding shall be equal to or greater than 130% of the area under the wind heeling moment curve to the same limiting angle;
- The righting moment curve shall be positive over the entire range of angles from upright to the second intercept.

A typical figure showing the curve of righting moment and the curve of heeling moment are shown in Figure 4.1.

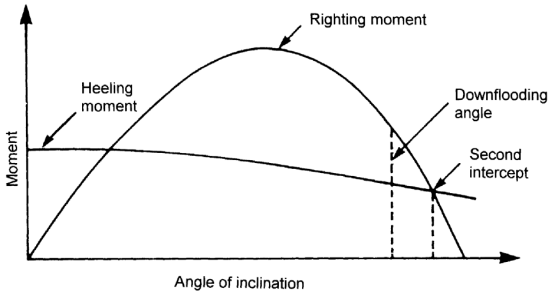

Figure 4.1: *Righting moment and wind heeling moment curves [12]*

Motion characteristic

Main considerations for motion characteristics of the semisubmersible platform are natural frequencies and response amplitude operators (RAOs). Depending on the location and sea state, ocean waves contain substantial energy in the spectral period range 5 to 25s. Therefore, for the design of a floater, the natural periods of motion should be kept out of the wave range to avoid resonance.

From previous experience, semisubmersible floaters for wind turbines usually have a natural period around 20 to 25s in heave motion and a natural period around 30s in pitch and roll motion. The natural periods for horizontal motions (sway, surge and yaw) are governed by the mooring system, which have a typical value around 100s.

Therefore, the key effort in the initial design of the semisubmersible platform in terms of motion characteristic is to achieve a proper heave natural period, and avoid large amplification of motions.

Other requirements

Beside buoyancy, stability and motion characteristics, there are some other requirements that need to be considered in the initial design.

- Fabrication. The hull weight should be kept small to reduce the material cost. Besides, the design should be kept simple and easy to fabricate. The overall size of the platform should be such that the platform is possible to be built in a shipyard dock.
- Transportation and installation. The semi-submersible wind turbine should be able to be wet-towed out in shallow water condition.

4.1.3 Design Procedure

The overall design procedure is summarized below:

1. A preliminary design is first performed by hand calculations with empirical formulas to estimate weight and buoyancy, static heeling angle and heave natural frequencies.
2. An initial design with hydrostatic and hydrodynamic analysis is then performed in HydroD with model built in GeiE. Results such as weight and buoyancy and stability curve are studied.
3. Hydrodynamic analysis is performed in HydroD (Wadam). Results of motion characteristics are studied.
4. Viscous damping is introduced into the model and sectional loads are then checked by design wave approach.
5. Sensitivity analysis is performed and results are summarized.

4.2 Preliminary Design

The preliminary design is first carried out by using hand calculation and empirical formulas and then verified by hydrostatic and hydrodynamic analysis using HydroD. Initial design data of a 5MW wind turbine floater 5-MW-CSC [72] is used as reference for the design of the 10MW wind turbine floater.

4.2.1 Main Dimension Design

The main consideration for main dimension design is to withstand the increased thrust force and corresponding overturning moment of the 10MW wind turbine as shown in Table 4.1. Due to the increased rated power and hub height, the overturning moment of the 10MW wind turbine is around 2.6 times larger than that of the 5MW turbine, which is the main challenge in this design.

Table 4.1: *Comparison of thrust and moment of 5MW and 10MW wind turbines*

Item	NREL 5MW RWT	DTU 10MW RWT	Ratio
Rated thrust [kN]	750	1500	2
Tower base overturning moment [kN*m]	67500	178500	2.6

Main dimensions for the 5MW wind turbine floater and the new 10MW wind turbine floater are provided in Table 4.2 and the design for the 10MW wind turbine floater is shown in Figure 7.20.

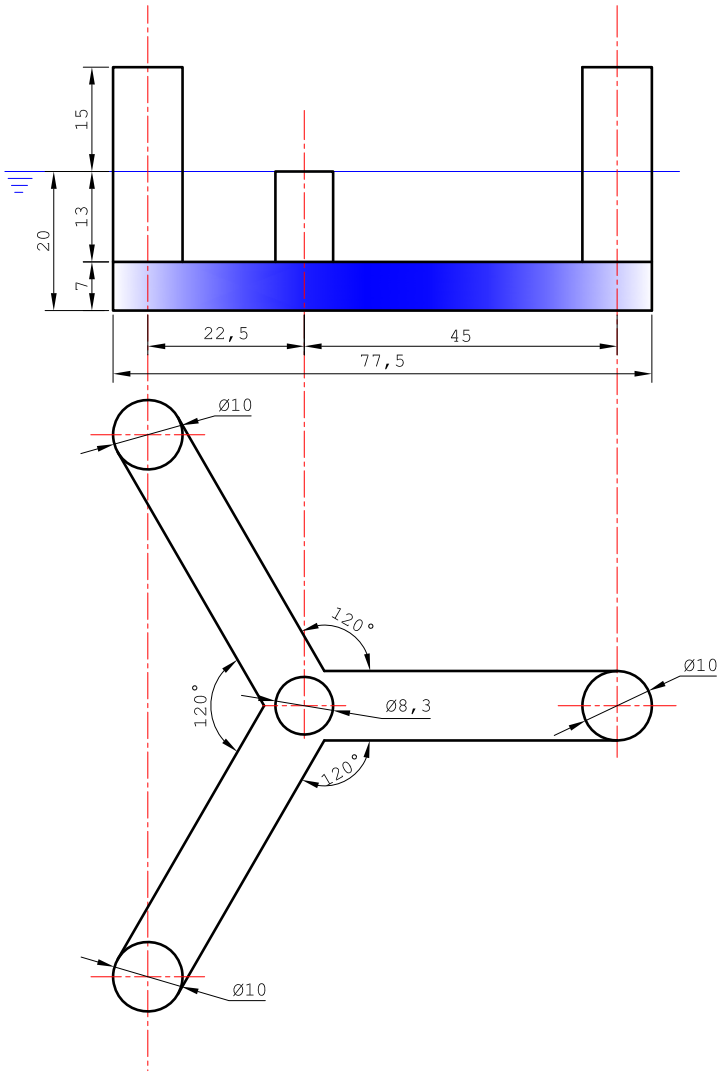

Figure 4.2: *Main dimensions for the 10MW wind turbine semi-submersible floater*

Table 4.2: *Main dimensions for 5MW and 10MW wind turbine floaters*

Main dimensions [m]	5MW	10MW
Draft	30	20
Freeboard	20	15
Center column diameter	6.5	8.3
Side column diameter	6.5	10
Column side to center distance	41	45
Pontoon height	6	7
Pontoon width	9	10
Thickness	–	0.04

The design process includes many iteration procedures, which could not be documented. However, the main considerations for dimension design are summarized in the following.

Draft

As mentioned in Section 1.2.2, one big advantage of semi-submersible platform comparing the spar the TLP design is the flexible draft which allows it to operate in different water depth. Besides, a semi-submersible platform is designed to be stabilized mainly by water area inertia rather than gravity (spar platform). Therefore, the author believes the design draft for the 5MW wind turbine floater is too large. And as for the initial design, the design draft is decreased to 20m.

Besides, a transient draft should also be designed to allow towing of the semi-submersible platform in shallow water. However, this is not considered in this initial design.

Freeboard

The freeboard is mainly used to increase the angle of zero restoring(downflooding) and thus increase the area under the restoring moment curve. In the current design, the side columns are designed to be water tight. Therefore, the main consideration would be to fulfil the stability requirement by the DNV standard, which is discussed in Section 4.1.2.

As confirmed by later calculations, a freeboard of 15m could fulfil the requirement with a proper safety margin.

Center column

Although the tower for a floater should be different from that for a fixed support as discussed in Section 3.1.3, the same tower for the DTU 10MW RWT are used for the floater design in this project. Moreover, the tower is assumed to be connected to the semi-submersible platform at sea level. Then, since the base diameter of the tower is 8.3m, the diameter of the center column is taken as the same value of the tower base diameter to keep consistency.

Side column

The diameter of side column and the distance between side and center columns are of key importance to provide enough water area inertia to counteract the increased overturning moment. Although increasing the distance between side and center columns is more efficient (inertia is proportional to the distance squared), it is limited from the fabrication point of view as pointed out in Section 4.1.2.

In this initial design the total incensement of water area inertia could be estimated ac-

cording to Table 4.2, which is shown in Equation (4.1):

$$\begin{aligned}\frac{I_{10MW}}{I_{5MW}} &\approx \frac{A_{10MW}}{A_{5MW}} \times \left(\frac{L_{s2c,10MW}}{L_{s2c,5MW}}\right)^2 \\ &= \frac{\pi/4 \times 10^2}{\pi/4 \times 6.5^2} \times \left(\frac{45}{41}\right)^2 \\ &= 2.8\end{aligned} \tag{4.1}$$

This value is larger than the ratio of overturning moment in Table 4.1, which is 2.6. Therefore, it is believed to give at least as good stability behaviour as the 5MW design.

Therefore, the diameter of side column is designed to be 10m and the distance between side and center column is chosen to be 45m.

Pontoon

Three pontoons are designed to connect side columns. They should be strong enough to withstand the external loads, and they should also provide enough space for ballast.

The pontoon width is design to be identical to the diameter of the side column to ensure a consistent and simple design. The pontoon height is designed to be such that enough space is provided for ballast. In this design, a pontoon height of 7m is chosen.

An overview of all the main dimensions are provided in Table 4.2 and Figure 7.20.

4.2.2 Coordinate System

The coordinate system of the wind turbine and semi-submersible is set according the GL standard [70]: with the origin being at the sea level, x-axis along wind direction and z-axis pointing upward, as Figure 4.3 shows. This is consistent with the definition of degrees of freedom for floating wind turbines by DNV [12], as shown in Table 4.3.

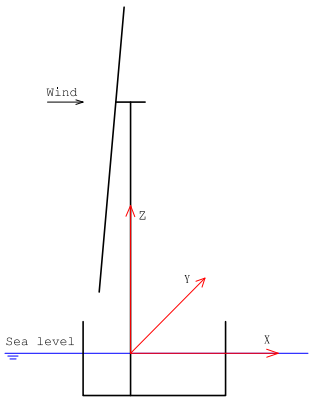

Figure 4.3: *Coordinate system for the turbine and semi-submersible platform*

Table 4.3: *Definition of degrees of freedom [12]*

Degree of freedom	Description
Surge	Translation along the longitudinal axis (main wind direction), x-axis
Sway	Translation along the lateral axis (transversal to the main wind direction), y-axis
Heave	Translation along the vertical axis, z-axis
Roll	Rotation about the longitudinal axis, x-axis
Pitch	Rotation about the lateral axis, y-axis
Yaw	Rotation about the vertical axis, z-axis

4.2.3 Weight Calculation

Weight calculation of the 10MW wind turbine and the semi-submersible platform are shown in Table 4.4. It is seen from the calculation that, the steel mass of the semi-submersible platform is about twice as that of wind turbine.

The overall center of mass is in the x-z plane due to symmetry. The x-coordinate of the center of mass is -0.1m due to the eccentric weight of rotor. However, this is a favourable result, since the corresponding moment will act to cancel part of the overturning moment induced by wind.

One major concern is the z-coordinate of center of mass, which is 22.3m above sea level. This will result in a very unstable system according to the basic naval architecture principle. This is due to the large top mass and large hub height of the wind turbine. However, by using ballast water with a low center of mass, this issue could be solved, as will be seen later.

Table 4.4: *Mass of the 10MW wind turbine and the semi-submersible platform*

	Component	mass [t]	x [m]	y [m]	z [m]
	Rotor	230	-7.1	0	119
	Nacelle	446	2.7	0	121.5
	Tower	628	0	0	47.6
WT	Overall	1305	-0.3	0	85.5
	Columns	1005	0	0	1.2
	Pontoons	1583	0	0	-16.5
Semi	Overall	2588	0	0	-9.6
Total	Total	3893	-0.1	0	22.3

4.2.4 Buoyancy Calculation

Buoyancy calculation is performed according to the design draft. It is shown from Table 4.5 that the buoyancy contributions from center column and side columns are almost balanced with the total weight shown by Table 4.4. However, the pontoons contribute to additional displacement, taking up to 72.6% of the total displacement, which need to be balanced by ballast. This is a big disadvantage regarding this pontoon type semi-submersible. This issue is discussed later.

Table 4.5: *Buoyancy calculation of the semi-submersible platform*

Buoyancy	Displacement [t]	x [m]	y [m]	z [m]
Center column	721	0	0	-6.5
Side columns	3140	0	0	-6.5
Pontoons	10221	0	0	-16.5
Overall	14081	0	0	-13.8

4.2.5 Ballast Design

As shown from Table 4.4 and Table 4.5, there is much more buoyancy than weight in this structure. The difference is 10188 tones, which needs to be balanced by ballast.

In this concept, sea water is used as ballast. Therefore, the volume required for ballast can be calculated as:

$$V_{ballast} = \frac{Displacement - Weight}{\rho_{sea\ water}} = 9940m^3 \tag{4.2}$$

Table 4.6: *Available space for ballast*

Space	Volume [m^3]	Used as ballast?
Center column	690	No
Side columns	6492	No
Pontoons	9770	Yes
Total	16952	9770

From Table 4.6 it is clear that the semi-submersible is able to provide enough space for ballast. As mentioned before, the ballast water could also be used to lower the center of gravity. Therefore, space in pontoons would be the first choice. By taking all the space in the pontoons for ballast, it will still need 170m^3 sea water to fully balance the buoyancy. However, this extra space is not taken in this initial design for the following considerations:

- The relative error for the buoyancy, weight in balancing is 1.7% which is an acceptable error for initial design. The default error in the software HydroD is 5%.

- In later design, there would be additional weight from mooring lines which is not considered in this initial design. Therefore, it's advisable to left some buoyancy.

In reality, the semi-submersible will be divided into several compartments to allow for flexible draft operation. In the initial design, they are assumed to be one big compartment in the pontoon that is fully filled with sea water.

The final weight with ballast, vertical center of gravity(VCG) and vertical center of buoyancy(VCB) are summarized in Table 4.7.

Table 4.7: *Summary of weight and displacement after ballast design*

Weight	3893	t
Displacement	13908	t
Vertical center of gravity	-5.7	m
Vertical center of buoyancy	-13.8	m

4.2.6 Hydrostatic Consideration

One important parameter from hydrostatic point of view is the static heeling angle. This angle should be kept small for the wind turbine to operate in a nearly vertical plane. This angle corresponds to the situation when the overturning moment is balanced by the restoring moment, which is indicated as the first cross point of the heeling moment and righting moment in Figure 4.1.

Assuming the center of rotation is the same as the center of buoyancy, the overturning moment/heeling moment could be estimated as:

$$\begin{aligned} M_{overturning} &= Thrust \times (z_{hub} - z_b) \\ &= 1500 \times (119 + 13.8) \\ &= 194897kN \cdot m \end{aligned} \tag{4.3}$$

The pitch restoring coefficient C_{55} could be calculated by [25]:

$$C_{55} = \rho g V \left(\underbrace{\int_{A_w} x^2 dS/V}_{(1)} + \underbrace{z_b - z_G}_{(2)} \right) = \rho g V \overline{GM}_L \tag{4.4}$$

where V is the displaced volume, A_w is the water plane area, z_b is the vertical center of buoyancy, z_G is the vertical center of gravity and $\overline{GM}_L$ is the longitudinal gravity metacentric height. As shown by Equation (4.4), there are two contributions to the longitudinal metacentric height, one from the inertia of water area and the other from the vertical distance between buoyancy and gravity. The calculation of water area inertia is summarized in Table 4.8.

Table 4.8: *Calculation of water area inertia*

Item	Diameter [m]	Distance to rotation center [m]	I_principle [m^4]	I_rotation center [m^4]
Center column	8.3	0	233	233
Side column I	10	45	491	159534
Side column II	10	22.5	491	40252
Total				240270

Table 4.9: *Calculation of metacentric height and the restoring coefficient*

Contribution(1) [m]	Contribution(2) [m]	GM (1)+(2) [m]	C_{55} [kN*m/rad]
17.7	-8.1	9.6	1309594

Then, the calculation of gravity metacentric height and finally the restoring coefficient are summarized in Table 4.9.

Therefore, the static heeling angle could be calculated by using Equation (4.3) and (4.4):

$$\begin{aligned}\theta = \eta_5 &= \frac{M_{overturning}}{C_{55}} = \frac{194897}{1309594} \times \frac{180^\circ}{\pi} \\ &= 8.5^\circ\end{aligned} \tag{4.5}$$

This angle is acceptable in the initial design.

4.2.7 Hydrodynamic Consideration

As discussed in Section 4.1.2, the heave natural period of the structure is of main concern. The heave natural period of the structure could be calculated as:

$$T_{n3} = 2\pi\sqrt{\frac{M + A_{33}}{C_{33}}} \tag{4.6}$$

In this design, the restoring force associated with the heave motion is due to the change in displaced volume. The restoring coefficient could be obtained by:

$$C_{33} = \rho g A_w \tag{4.7}$$

At a first step, the added mass is assumed to be identical to the displacement (weight with ballast). Therefore the natural period could be calculated by:

$$\begin{aligned}T_{n3} &= 2\pi\sqrt{\frac{2M}{\rho g A_w}} \\ &= 2\pi \times \sqrt{\frac{2 \times 13908}{1.025 \times 9.81 \times \frac{\pi}{4}\left(10^2 \times 3 + 8.3^2\right)}} \\ &= 19.4s\end{aligned} \tag{4.8}$$

This period corresponds to a wave with wave length around 600m which could be possible in realimprove the prediction sea state. However, as will be shown in the later calculation, the pontoon may have to a larger added mass coefficient than unit. Besides, the pontoon could provide viscous damping which could limit the response at resonance. Therefore, as an initial design, this value is accepted.

4.2.8 Summary

Key parameters from the preliminary design of the new semi-submersible floating wind turbine are summarized in Table 4.10.

Table 4.10: *Key parameters for the draft semi-submersible wind turbine design*

Geometry			Property		
Turbine Power	10	MW	Turbine mass	1305	t
Hub height	119	m	Semi mass	2588	t
Side column diameter	10	m	Displacement	13908	t
Center column diameter	8.3	m	Center of gravity	-5.7	m
Pontoon length	45	m	Center of buoyancy	-13.8	m
Width overall	77.5	m	Heeling angle	8.5	deg
Operation draft	20	m	Heave natural period	19.4	s

4.3 Hydrostatic Analysis

The hydrostatic performance is calculated by DNV SESAM software HydroD. The 3D model of the platform and turbine (both the panel model and the mass model) is built by GeniE, which is then discretized into finite elements and imported into HydroD for static calculation. Details regarding modeling using HydroD and GeniE could be found in the user manuals [64, 73].

4.3.1 Rotation Axis

Due to yaw capability of wind turbine, the rotor plane is assumed to be always perpendicular to the wind direction (when neglecting the shaft tilt angle).

The first thing before stability analysis is to examine the most dangerous rotation axis (pitch/roll motion), in other words, the axis of smallest metacentric height. However, since the geometry is rotational symmetry with respect to the z-axis as defined in Figure 4.4, one would expect that metacentric heights for different rotation axis in the horizontal plane are the same. This is proved in the following.

As shown in Figure 4.4, three point masses m are considered. The distance from the point mass to the rotational center is L. The angle between every point mass is 120° with respect to the rotational center. β is a random angle. The mass moment of inertia for

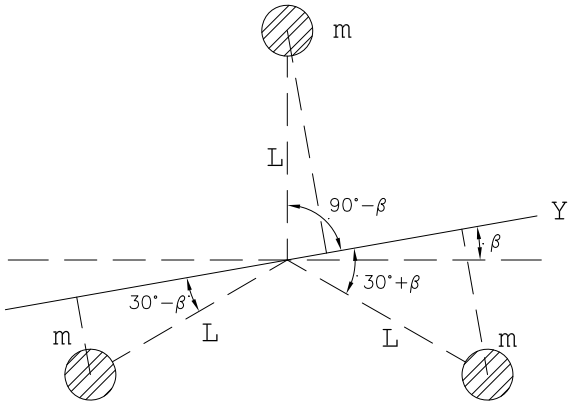

Figure 4.4: *Illustration of rotation axis with three point masses*

the system about the axis Y can be calculated:

$$\begin{aligned} I_Y &= m \cdot L^2 \cdot \left(\sin^2(90° - \beta) + \sin^2(30° - \beta) + \sin^2(30° + \beta)\right) \\ &= m \cdot L^2 \cdot \left(\cos^2(\beta) + (\sin(30°)\cos(\beta) - \cos(30°)\sin(\beta))^2\right. \\ &\quad \left.+(\sin(30°)\cos(\beta) + \cos(30°)\sin(\beta))^2\right) \\ &= m \cdot L^2 \cdot \left(\cos^2(\beta) + \frac{1}{2}\cos^2(\beta) + \frac{3}{2}\sin^2(\beta)\right) \\ &= \frac{3}{2} m L^2 \end{aligned} \tag{4.9}$$

It is seen from Equation (4.9) that the mass moment of inertia for the three point mass about the random axis is a constant value, which is not related to the angle β.

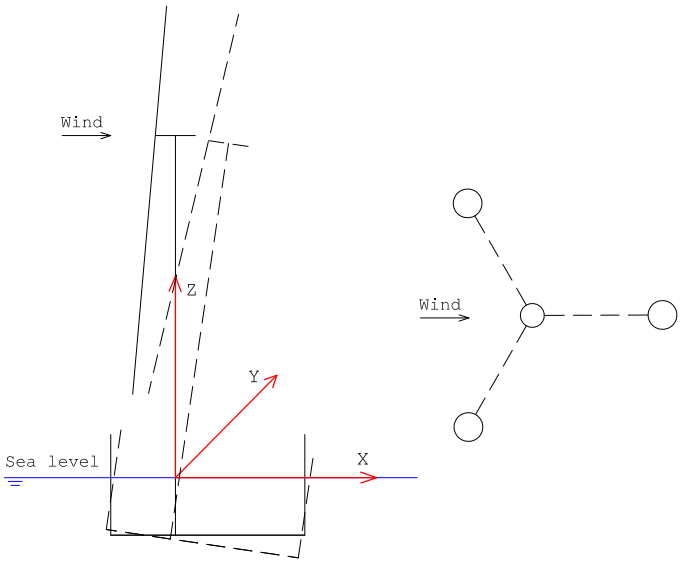

Figure 4.5: *Most unfavorable situation with respect to stability*

This result could be used in the calculation of the semi-submersible water area inertia. Since the principle area moment of inertia is a constant value, then the total area mo-

ment of inertia about the rotation axis will be a constant value for the reason that is discussed above. Therefore, the metacentric height for this structure will remain constant for different rotational axis. Then the most important issue regarding stability is the downflooding angle. The most unfavorable situation would then be the wind direction parallel with one of the pontoon, blowing from the two columns side to the single column side. This situation is illustrated in Figure 4.5. All the future calculations will be based on this situation. However, a sensitivity study for different wind/wave attacking angle will be carried out later.

4.3.2 Panel Model

A panel model is used for stability calculation and for calculation of 3D wave potential in Wadam. All wetted surfaces (that will receive hydro pressure) in the panel model are discretized by finite elements. As required by the software, the element diagonal in the panel model shall not exceed wave length/4, which means: For square element:

$$l_{mesh} < \frac{1}{4\sqrt{2}}\lambda \approx \frac{1}{6}\lambda \tag{4.10}$$

Usually, wave energy is mainly distributed in the wave period region from 5s to 25s. In the initial design, wave periods from 3s to 30s are taken into analysis. Therefore, the largest mesh length (assuming a cubic element and deep water) is limited by:

$$l_{mesh,\max} < \frac{1}{4\sqrt{2}}\lambda_{\min} = \frac{1}{4\sqrt{2}}\frac{gT_{\min}^2}{2\pi} = 2.5m \tag{4.11}$$

The semi-submersible platform with two lower sections of the tower defines the possible wet surface, and is discretized by shell elements. Mesh density of 2m is applied which results in a total number of 2377 panel elements. Figure 4.6 shows the final result. A mesh convergence study is also performed, the results of which is described in Section 4.5. The convergence study proves that the mesh density of 2m is a good choice in terms of balance of computational time and accuracy in the initial design.

4.3.3 Mass Model

A mass model contains all the information regarding mass distribution of the whole structure. In this case, the mass model is built in GeniE and discretized into finite elements before being implemented into HydroD.

The tower and semi-submersible platform is modelled using shell elements while the blades are modelled using beam elements. The hub and nacelle are represented by point mass and are connected to the other elements by weightless beam element.

The ballast water inside the pontoon is modelled by increase the density of the material associated to these pontoons. Although some error could be introduced by this procedure, the correct distribution of mass along the pontoon is ensured which is believed to contribute the most of the inertia of the pontoon ballast system, while the detailed geometrical property of the cross-section of the pontoon ballast system is of secondary importance. Figure 4.7 represents the final mass model.

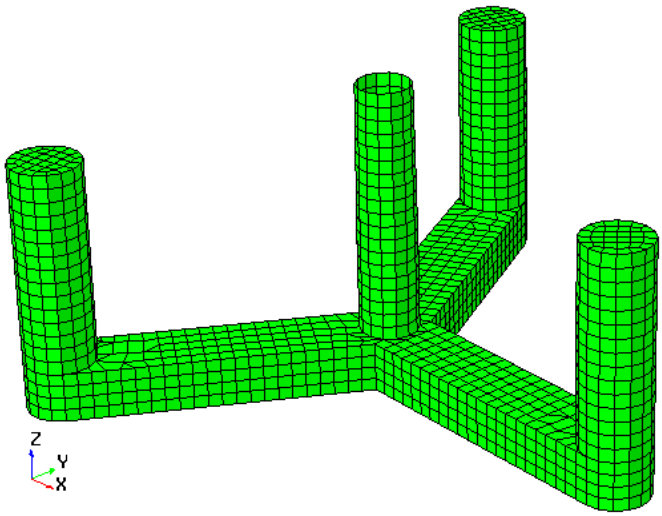

Figure 4.6: *Panel model of the semi-submersible floating wind turbine*

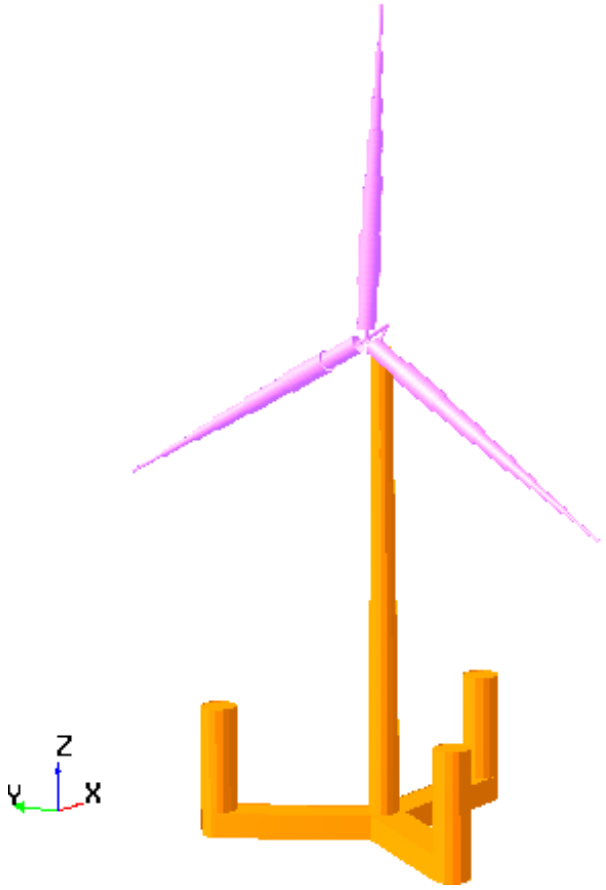

Figure 4.7: *Mass model for the semi-submersible floating wind turbine (purple: rotor, orange: semi and tower), mesh is not shown*

4.3.4 General Properties of Whole System

General information of the whole semi-submersible floating wind turbine is provided in Table 4.11 after the stability analysis by HydroD. It is shown that the results calculated by hand have a good agreement with results from HydroD.

Table 4.11: *Comparison of general properties by Hydro and by hand calculation*

Property	Unit	HydroD	Hand Calc.	Relative Error
Displacement	t	13955	13908	0.30%
VCG	m	-5.66	-5.65	0.20%
VCB	m	-13.81	-13.76	0.40%

4.3.5 Stability behaviour

In the stability analysis, the overturning moment is estimated in the same way as hand calculation, shown in Equation (4.3). It means that only the contribution from maximum thrust is taken into account.

Results for the stability analysis by HydroD are summarized through Figure 4.8 and Table 4.12. It is seen from Figure 4.8 that, there are two intercept angles of the righting moment curve and the heeling moment curve. The first intersection angle is denoted as static heeling angle as shown in Table 4.12. The righting moment reaches its maximum at an angle around 20 degree which is corresponding to the state of immersion of the side column deck.

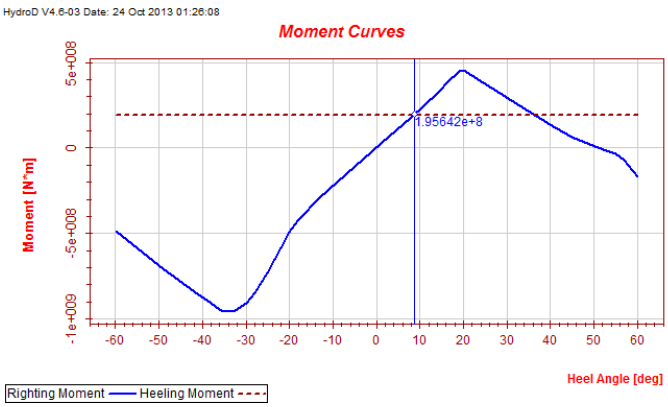

Figure 4.8: *Moment curve by stability analysis of HydroD*

Table 4.12: *Comparison of stability calculation by HydroD and by hand*

Stability Property	Unit	HydroD	Hand Calc.	Relative Error
GM	m	9.0	9.6	6.70%
Heeling angle	deg	8.7	8.5	2.30%

It is shown from the table that hand calculation overpredicted the gravity metacentric height, resulting in an underpredicted heeling angle. The reason is that Equation (4.4) is

based on the assumption of small angle of inclination [74]. The prediction error increases with the heeling angle. Therefore, theory of large angle stability should be used to improve the prediction of stability performance.

Stability check against DNV rule is performed in Table 4.13, as discussed in Section 4.1.2.

Table 4.13: *Stability rule check*

Downflooding angle [deg]	Area under righting moment curve [MN*m]	Area under heeling moment curve [MN*m]	Area ratio	DNV rule
36.2	172.3	123	140%	130%

Since the side column is water tight, the downflooding angle is chosen to be identical to the second intercepting angle. It is seen from Table 4.13 that the area under the righting moment curve to the angle of downflooding is 40% greater than the area under the wind heeling moment curve to the same limiting angle. Besides, the righting moment stays positive from upright to the second intercept. Therefore, the design satisfies the intact stability requirement from DNV.

4.4 Frequency Domain Hydrodynamic Analysis

HydroD (Wadam) is used to perform hydrodynamic analysis of the semi-submersible floating wind turbine without mooring lines. Wadam is based on 3D potential flow theory as discussed in Chapter 2.

4.4.1 Eigenfrequency analysis

Natural Frequency of floater

Due to symmetry of the geometry, pitch and roll motion characteristics are the same. Since no mooring lines are considered in the initial design, horizontal motions are not discussed which are usually determined by the properties of mooring system. Therefore, only heave and pitch motion are discussed in this section.

It is seen from Figure 4.9 and Figure 4.10 that the added mass is a function of excitation frequency. However, the variation is not that much, and when the wave period become very large, the added mass converges to a constant value.

Natural frequencies of heave and pitch motion could be obtained by using Equation (2.23), results of calculations are shown in Table 4.14.

It is seen that the natural period for heave motion is a little higher than that predicted by hand calculation (which is 19.4s). That is due to the fact that the Wadam analysis gives an added mass coefficient that is larger than the previously assume value 1.0, which is clear from Table 4.14.

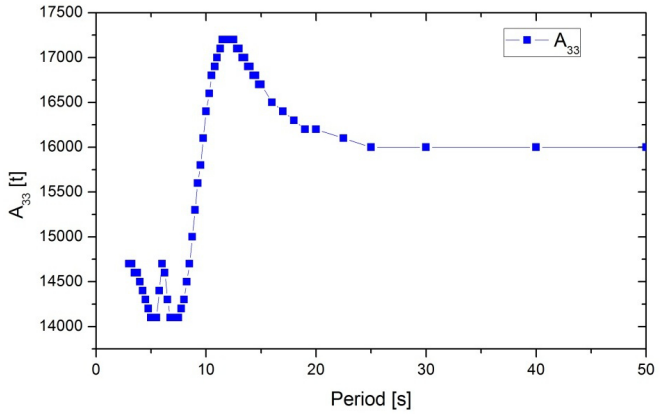

Figure 4.9: *Added mass of heave motion as a function of wave period (head sea)*

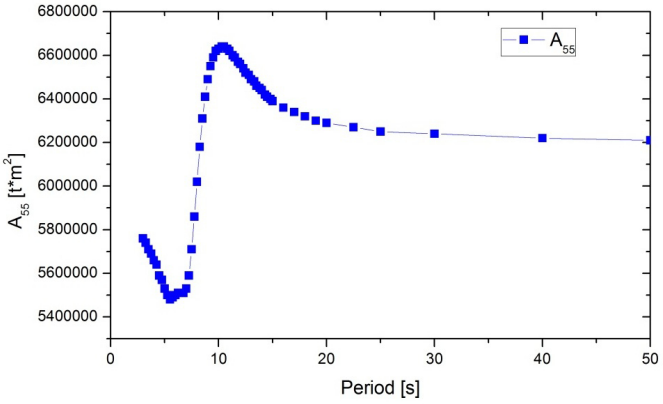

Figure 4.10: *Added mass of pitch motion as a function of wave period (head sea)*

1P and 3P of wind turbine

For wind turbines, the rotational frequency 1P and blade passing frequency 3P are important characteristic frequencies. The coupling of the 1P and 3P with natural frequencies of the whole semi-submersible platform should be avoided.

It is seen from Table 4.15 that the 1P and 3P frequencies of wind turbine are less than 10s, which are well out of the range of natural frequencies of the semi-submersible platform. Therefore, coupling of the motion of the whole system with the rotation of blades is negligible.

Table 4.14: *Eigenfrequency calculation for heave and pitch motion*

Degree of Freedom	Heave	Pitch
Body mass [kg, kg*m2]	1.40E+07	2.15E+10
Added mass [kg, kg*m2]	1.61E+07	5.76E+09
Restoring [N/m, N*m]	2.83E+06	1.24E+09
Natural Period [s]	20.47	29.48

Table 4.15: *1P and 3P frequency of DTU 10MW RWT*

Frequency	Minimum	Maximum
Rotational Frequency	6 rpm	9.6 rpm
1P	6.25 s	10.00 s
3P	2.08 s	3.33 s

4.4.2 Motion Analysis

RAO

Figure 4.11 and Figure 4.12 show the results of heave and pitch response amplitude operator. It is seen that for heave motion, resonance occurs at wave period around 20s, while for pitch motion resonance occurs at wave period around 30s. These results are in agreement with the results of eigenfrequency analysis. Some facts should be noted: 1)The response at resonance goes to infinity; 2)There is cancellation effect for heave motion. These effects are analyzed in the following sections.

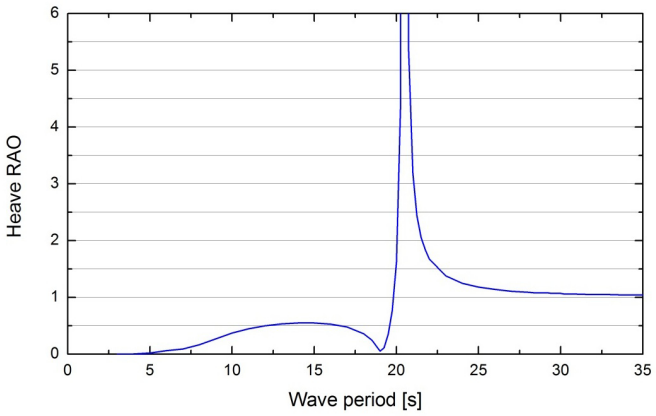

Figure 4.11: *Heave RAO (head sea)*

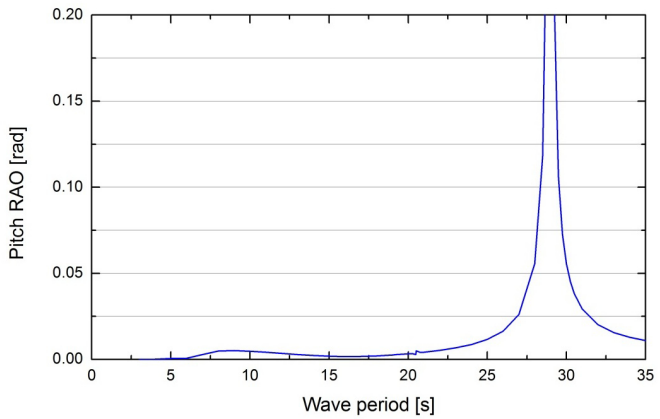

Figure 4.12: *Pitch RAO (head sea)*

Analytical solution & Cancellation effect

From Figure 4.11, it is obvious that there is cancellation effect in the heave RAO before the resonance, at the wave period around 18s. This is corresponding to the condition that the pressure acting on the top and bottom area of the pontoon generates the same force with opposite directions.

This issue is discussed in details here. An illustration is provided in Figure 4.13 for the problem. In the following derivation, subscript $_B$ means the bottom face of pontoon and subscript $_T$ means the top face of pontoon.

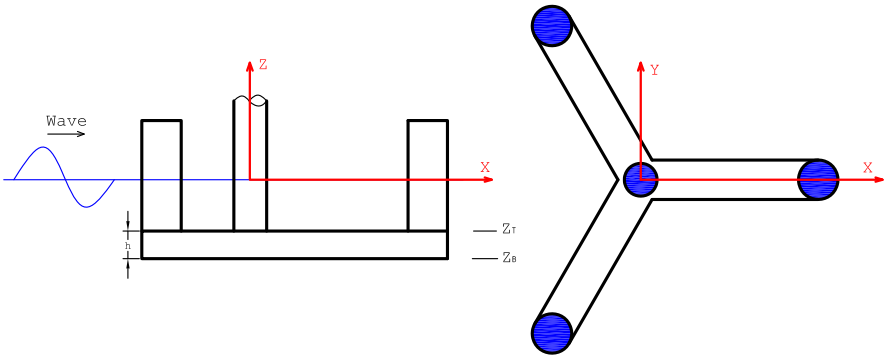

Figure 4.13: *Semi-submersible platform with regular head sea incident wave*

Assumptions:

- Linear potential theory with regular deep water wave
- Long wave approximation
- Steady-state condition
- Heave motion is not coupled to other dofs

From the first assumption, the linear velocity potentialϕ_0, dynamic pressure p_0 and vertical acceleration of wave particle a_{03} are given by:

$$\phi_0 = \frac{g\xi_a}{\omega} e^{kz} \cos(\omega t - kx) \tag{4.12}$$

$$p_0 = -\rho \frac{\partial \phi_0}{\partial t} = \rho g \xi_a e^{kz} \sin(\omega t - kx) \tag{4.13}$$

$$a_{03} = \frac{\partial^2 \phi_0}{\partial z \partial t} = -\omega^2 \xi_a e^{kz} \sin(\omega t - kx) \tag{4.14}$$

where k is the wave number.

Radiation damping can be neglected for long waves, then the equation of motion for heave has the following form:

$$(m + A_{33})\,\eta_3 + C_{33}\eta_3 = F_{exc,3}(t) = F_{FK,3}(t) + F_{D,3}(t) \tag{4.15}$$

where F_{FK} is the Froude-Krylov force and F_D is the diffraction force.

(i) Froude-Friloff force (take $x = 0$)
Pressure on the bottom of the pontoon:

$$p_{0B} = \rho g \xi_a e^{kz_B} \sin(\omega t) \Rightarrow Force : F_{FK,B} = p_{0B} A_B \tag{4.16}$$

Pressure on the top of the pontoon:

$$p_{0T} = \rho g \xi_a e^{kz_T} \sin(\omega t) \Rightarrow Force : F_{FK,T} = -p_{0T} (A_B - A_w) \tag{4.17}$$

Then the vertical force acting on the pontoon is:

$$F_{FK,3} = \rho g \xi_a \left(e^{kz_B} - e^{kz_T} \right) \sin(\omega t) A_B + \rho g \xi_a e^{kz_T} \sin(\omega t) A_w \tag{4.18}$$

Using Taylor expansion for e^{kz} about the mean depth of pontoon $z_m = \frac{1}{2}(z_T + z_B)$, the above equation could be simplified to:

$$F_{FK,3} = \rho g \xi_a e^{kz_m} \sin(\omega t) \left(e^{k(z_T - z_m)} A_w - k A_B h \right) \tag{4.19}$$

(ii) Diffraction force
Using long wave approximation, the diffraction force could be easily obtained:

$$F_{D,3} = A_{33} a_{03} = -gk \xi_a e^{kz_m} \sin(\omega t) A_{33} \tag{4.20}$$

(iii) Total force
By using the Taylor expression of $e^{k\Delta z}$ about $\Delta z = z_T - z_m = 0$, and $m = \rho (A_w z_T - A_B h)$ the total force could be written into:

$$\begin{aligned} F_{exc,3} &= F_{FK,3} + F_{D,3} \\ &= \xi_a e^{kz_m} \sin(\omega t) \left[\rho g A_w - \rho \omega^2 A_w z_m - \omega^2 (m + A_{33}) \right] \end{aligned} \tag{4.21}$$

(iv) Response
Heave response of the system could be obtained by assuming:

$$\eta_3 = \eta_{3a} \sin(\omega t) \tag{4.22}$$

The heave RAO is then:

$$\begin{aligned} \left| \frac{\eta_{3a}}{\xi_a} \right| &= \left| \frac{e^{kz_m} \left[\rho g A_w - \rho \omega^2 A_w z_m - \omega^2 (m + A_{33}) \right]}{\left(1 - \frac{\omega^2}{\omega_{n3}^2} \right) \rho g A_w} \right| \\ &= \left| \frac{e^{kz_m}}{\left(1 - \frac{\omega^2}{\omega_{n3}^2} \right)} \left(1 - k z_m - \frac{\omega^2}{\omega_{n3}^2} \right) \right| \end{aligned} \tag{4.23}$$

(v) Cancellation effect
The cancellation effect will take place when $kz_m = 1 - \frac{\omega^2}{\omega_{n3}^2}$, that is:

$$\omega_C = \frac{\omega_{n3}}{\sqrt{1 - \left|\frac{z_m}{g}\right| \omega_{n3}^2}} \qquad where, \omega_{n3} = \sqrt{\frac{C_{33}}{m + A_{33}}} \tag{4.24}$$

Using the value obtained by Wadam as shown in Table 4.14, we can get the wave period corresponding to the cancellation effect, $T_C = 18.8s$.

So, weve now obtained the analytical solution to the heave RAO, which is Equation (4.23). A comparison with the numerical solution by Wadam is shown in Figure 4.14.

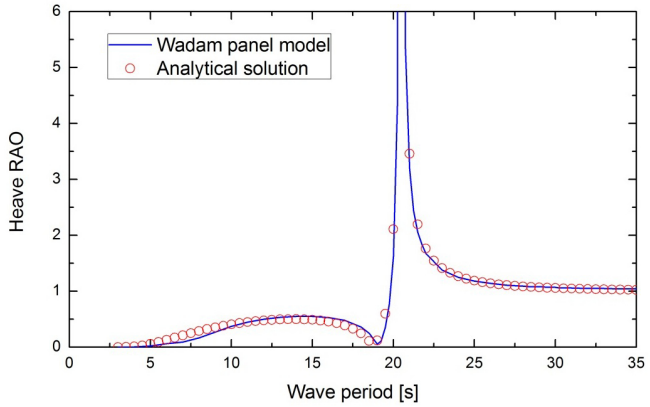

Figure 4.14: *Comparison of the analytical solution of heave RAO with numerical solution from Wadam panel model*

It is seen from Figure 4.14 that the numerical results and the analytical solution in general agree with each other very well. Some difference in small wave period may due to the fact that long wave approximation will no longer hold for small wave period and potential damping is neglected in the derivation of analytical solution.

Potential damping

It is seen from the heave and pitch RAO that at resonance, the amplitude of heave and pitch motion goes to infinity. This fact indicates that there is almost zero damping at the resonance frequency.

The potential damping associated with heave and pitch motion are shown in Figure 4.15 and Figure 4.16. It is clear that for both degree of freedoms, the associated potential damping are banded to wave period between 5s and 15s. For wave periods smaller than 5s and larger than 15s, the potential damping is negligible.

As discussed in Chapter 2, the potential damping is associated with the capability of the body to generate waves. For the case of long waves, the structure tries to follow the wave rather than interact with the wave, then the waves generated by wave structure

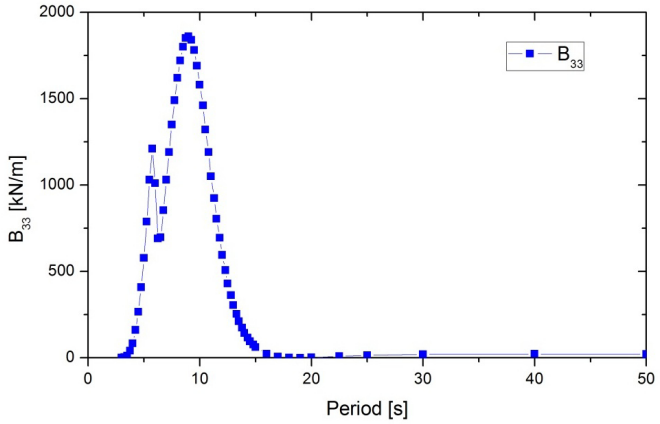

Figure 4.15: *Potential damping associated with heave motion (head sea)*

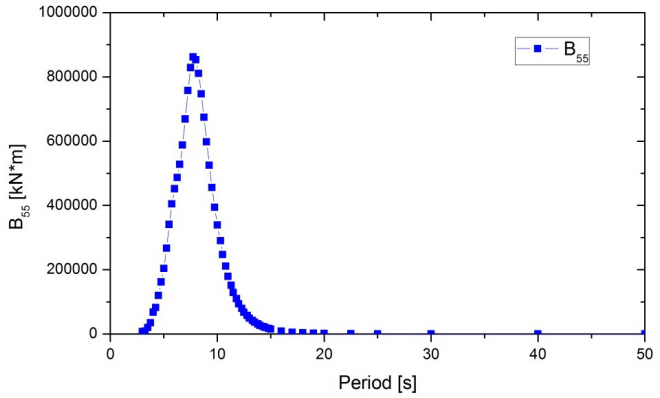

Figure 4.16: *Potential damping associated with pitch motion (head sea)*

interaction are small, which means the potential damping of the semi-submersible wind turbine platform at resonance is very small.

Therefore, in the case of resonance, viscous damping becomes very important to limit the amplification effect. As discussed in Section 2.2.4, viscous damping from linearized drag force should be included into the model. This is discussed in the following section.

4.4.3 Viscous Damping

Viscous damping is needed to better describe the system behavior at resonance. As already discussed in Section 2.2.4, linearization of viscous drag force is used as an estimation of viscous damping in the system.

Sea state

As shown in Equation (2.34), the viscous damping coefficient is related to a specific sea state. The site condition has been discussed in Section 3.2, load case EX is used here.

The 50-year sea condition at the site is summarized in Table 4.16.

Table 4.16: *Extreme sea conditions for site 14 Norway 5*

Parameter	Value (50 year return period)
Significant Wave Height, H_S [m]	15.6
Peak Frequency, T_p [s]	14.5

Spectrum

JONSWAP spectrum is most suitable to describe the sea state at the chosen site, as shown in Figure 4.17. Parameters for the spectrum is chosen according to Table 4.16 and DNV standard [75].

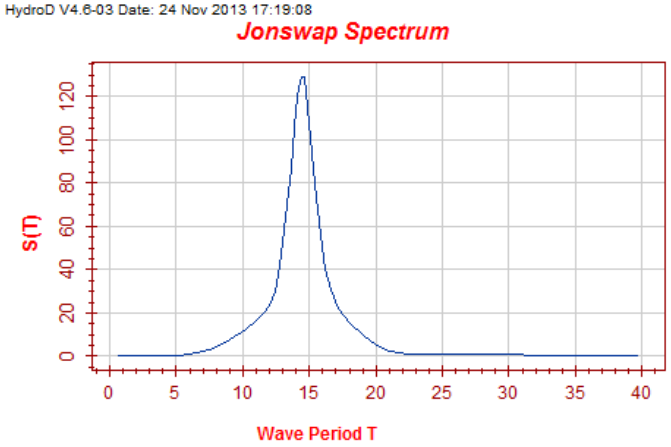

Figure 4.17: *The JONSWAP spectrum for the extreme sea state*

Morison Model

In order to use the Composite Model in HydroD to linearize viscous drag force, a Morison model is needed. Unlike a Dual Model, where the software applies the potential theory to the Panel Model and get the corresponding drag force from Morison Model, the Morison Model in a Composite Model will also contribute to buoyancy and inertia load. Therefore, special treatment is needed to solve the issue.

The drag force has a form of $\frac{1}{2}\rho C_D D\dot{x}\,|\dot{x}|$. In order to avoid any contribution to buoyancy from the Morison model, the dimension should be scaled down:

$$D' = 0.1\%D \tag{4.25}$$

Then, in order to keep the drag force unchanged, the drag coefficient should be scaled up accordingly:

$$C_D{}' = \frac{C_D D}{D'} = 1000 C_D \tag{4.26}$$

In this case, the additional volume introduced by Morison model is negligible:

$$V' = A'L = \frac{\pi}{4}D'^2L = (0.1\%)^2V \tag{4.27}$$

By setting the added mass coefficient to zero, the inertia load introduced by Morison Model is then also proportional to D'^2 which is quite small. Then it is sure that, the Composite Model will give a correct drag load while having almost no influence on the buoyancy and inertia load of the structure.

Drag Coefficients

The drag coefficients are chosen according to the DNV standard [76].

For cylindrical columns the drag coefficients are chosen to be $C_D = 1.0$.

For the rectangular shaped pontoon, the drag coefficient depends on the ratio of height and width of the cross-section. The drag force for vertical motion is chosen to be $C_D = 2.38$, while for horizontal motion, the drag coefficient is $C_D = 1.942$.

4.4.4 Motion with Viscous Damping

RAOs

In this section, Composite Model in HydroD is used to calculate the response of the semi-submersible platform. Results of heave and pitch RAOs are compared to the pure Panel Model, as shown in Figure 4.18 and Figure 4.19.

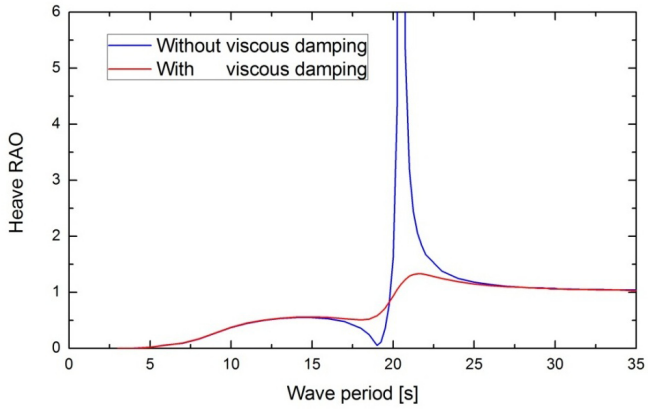

Figure 4.18: *Comparison of heave RAO with and without viscous damping*

It is seen that, with viscous damping, the amplitude of motion at resonance is significantly reduced. It is also noted that the RAO at wave period far away from resonance is not affected, which mean the implementation of the Morison model is successful. However, it should also be noted that when viscous damping is introduced, there is no cancellation effect in heave motion. This issue is discussed in details here.

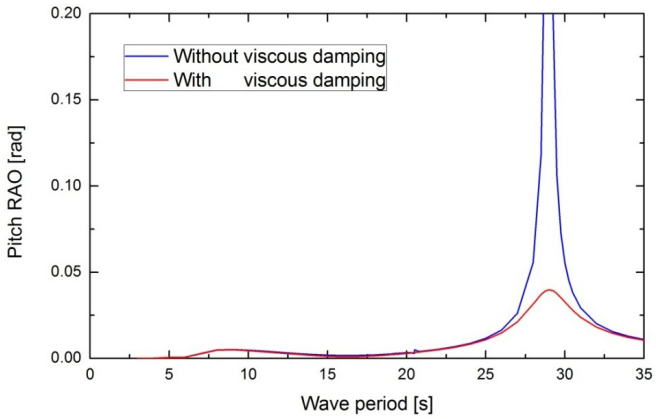

Figure 4.19: *Comparison of pitch RAO with and without viscous damping*

Cancellation Effect

As shown in Equation (2.33), the linearized the drag force is based on the relative velocity of the wave kinematics and the structure. For simplicity, it is assumed to have the following form:

$$F_{drag,3} = B_{viscous,3}\left(u_{03} - \dot{\eta}_3\right) \tag{4.28}$$

Then Equation (4.15) could be written into:

$$\left(m + A_{33}\right)\eta_3 + B_{viscous,3}\dot{\eta}_3 + C_{33}\eta_3 = F_{FK,3}\left(t\right) + F_{D,3}\left(t\right) + B_{viscous,3}u_{03} \tag{4.29}$$

Write the total excitation load into complex form (note that there is a phase angle of 90° between wave particle velocity and acceleration):

$$\begin{aligned} F_{exc,3} &= F_{FK,3} + F_{D,3} + B_{viscous,3}u_{03} \\ &= \xi_a \underbrace{e^{kz_m}\left[\rho g A_w - \rho\omega^2 A_w z_m - \omega^2\left(m + A_{33}\right)\right]}_{A}\sin\left(\omega t\right) + \xi_a \underbrace{\omega e^{kz_m} B_{viscous,3}}_{B}\cos\left(\omega t\right) \\ &= \xi_a\left(A\sin\left(\omega t\right) + B\cos\left(\omega t\right)\right) \\ &= \Im\left[\xi_a\left(A + Be^{i\frac{\pi}{2}}\right)e^{i\omega t}\right] \end{aligned} \tag{4.30}$$

If we also write the response in the complex form, then we have:

$$\left|\frac{\eta_{3a}}{\xi_a}\right| = \left|\frac{A + Be^{i\frac{\pi}{2}}}{\underbrace{C_{33} - \omega^2\left(m + A_{33}\right)}_{C} + i\underbrace{\omega B_{drag,3}}_{D}}\right| = \frac{A^2 + B^2}{C^2 + D^2} > 0 \tag{4.31}$$

The above equation means that when viscous damping is included in the system, the amplitude of heave response is non-zero. Therefore, there will be no cancellation effect for heave RAO with viscous damping, as shown in Figure 4.18.

4.4.5 Sectional Loads

Section Location

In order to check whether the initial design is appropriate with respect to stress level, sectional loads are calculated on three parallel sections along the pontoon. The locations of sections are chosen such that one is in the middle of the pontoon, one is close to the center of the structure and the other is close to the side column. Details of the section positions are shown in Table 4.17 and Figure 4.20.

Table 4.17: *Position of sections*

Section Label	Section Center Coordinate
Section 1	(10.0m, 0.0m, -16.5m)
Section 2	(22.5m, 0.0m, -16.5m)
Section 3	(35.0m, 0.0m, -16.5m)

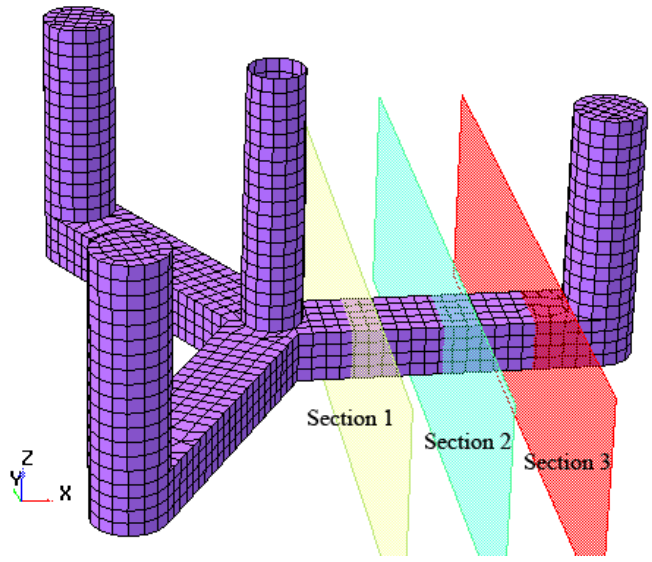

Figure 4.20: *Locations of sections on the pontoon*

Due to rotational symmetry of the semi-submersible platform, it is only required to set the three sections along one pontoon with different wave directions (from 0 degree to 180 degree) to cover all the loading conditions.

Sectional Loads

For the purpose of design check, only the sectional loads that contribute to the axial stress are considered (although other load cases may also be interest such as torsion, they are neglected), they are axial force along x-axis, F_x, bending about y-axis, M_y and bending about z-axis, M_z. They are plotted in Figure 4.21 and Figure 4.22 for the case of head sea. (M_z is zero due to symmetry)

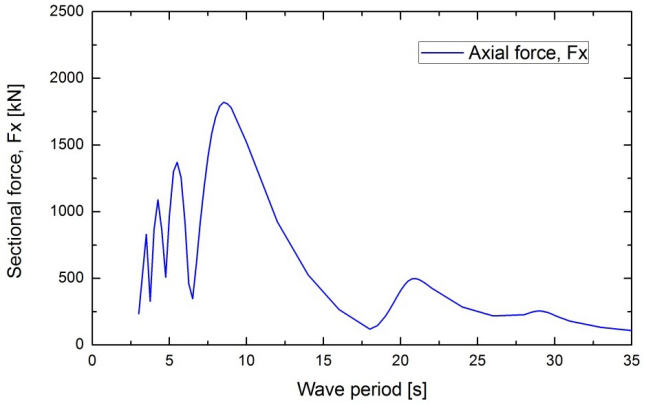

Figure 4.21: *Sectional force, F_x as a function of wave period (head sea, Section 1)*

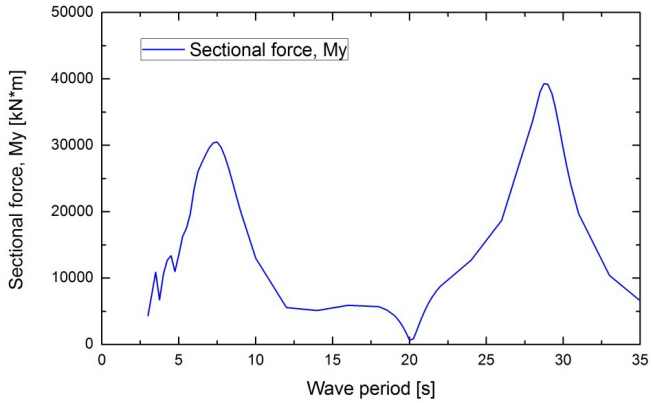

Figure 4.22: *Sectional force, M_y as a function of wave period (head sea, Section 1)*

It is seen from these figures that there are some strange variation of sectional force for small wave period. This issue is analyzed in the following section.

Cancellation at small wave period

In order to examine the cause of the oscillation of the sectional force at small wave period, the results are first compared with the results from pure Panel Model (without viscous effect), as shown in Figure 4.23 and Figure 4.24.

First of all, it is seen from the comparison that the cancellations at small wave period are not influenced by viscous damping. A detailed examine of the wave length associated with these periods with regarding to the characteristic length of semi-submersible platform is shown in Table 4.18. The locations are referred to Figure 4.20. The characteristic length of the semi-submersible platform in head sea is taken as the distance between the center of side columns along the x-axis, which is $Lc = 67.5m$ as shown in Figure 4.25.

As shown by Figure 4.25 and Table 4.18, the oscillation of the sectional force at small wave period is due to the cancellation effect of small waves. Location B, C and D correspond to

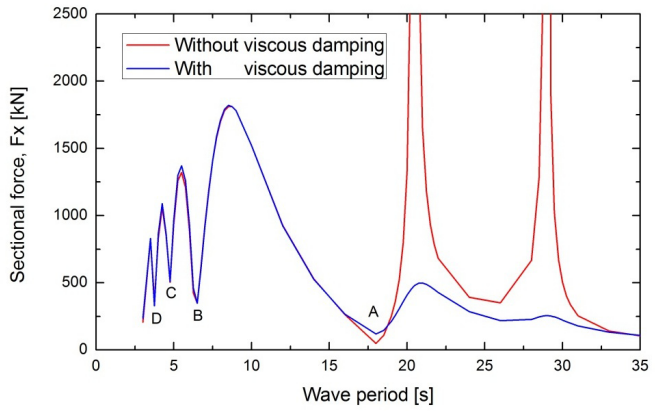

Figure 4.23: *Comparison of sectional force F_x with and without viscous damping (head sea, Section 1)*

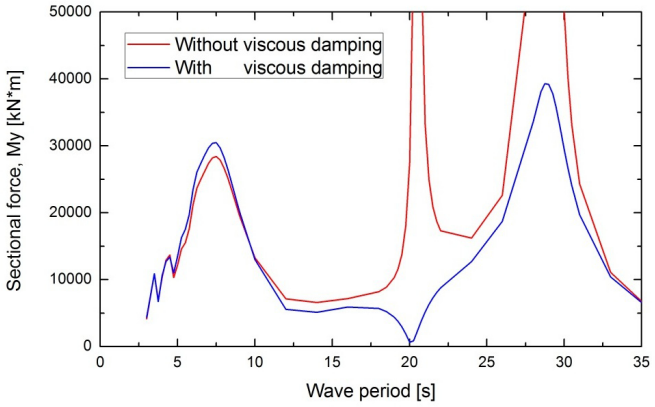

Figure 4.24: *Comparison of sectional force M_y with and without viscous damping (head sea, Section 1)*

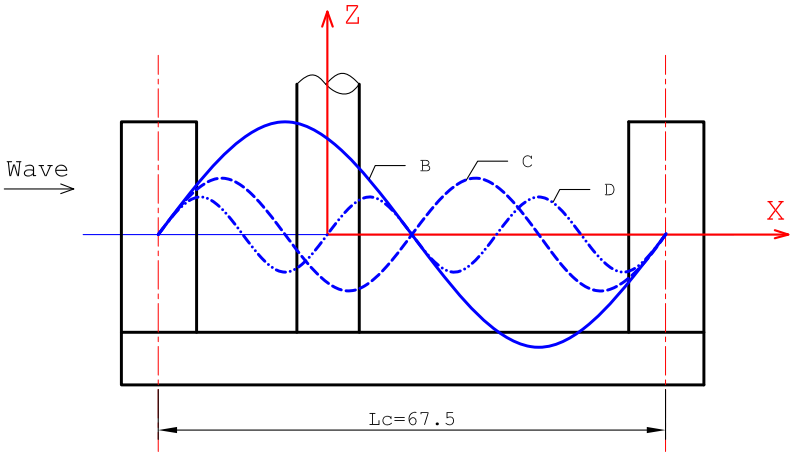

Figure 4.25: *Wave lengths for location B, C and D compared to characteristic length of semi-submersible (head sea)*

Table 4.18: *Examination of the cancellation effects*

Location	Wave Period [s]	Wave Length [m]	Remark
A	18	–	Tc=18.4s
B	6.5	66	1.0*Lc
C	4.75	35	1/2*Lc
D	3.75	22	1/3*Lc

one, two and three waves within the characteristic length of the semi-submersible platform respectively.

Besides, it is also observed that the sectional force M_z with viscous damping, has cancellation effect at resonance, which is quite different from the pure Panel Model. This effect is, however, not explained by the author at this stage.

Sectional Stress

Only axial stress along the x-axis is considered in the initial design phase. Due to symmetry of the cross section, the largest stress may occur at one of the four corners of the cross section, as shown in Figure 4.26.

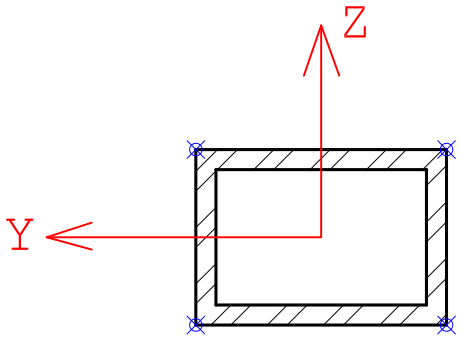

Figure 4.26: *Cross section of pontoon with possible positions for largest axial stress*

The axial stress σ_x at these four points could be obtained by applying the following expression:

$$\sigma_x = \frac{F_x}{A} + \frac{M_y}{I_y}y + \frac{M_z}{I_z}z \tag{4.32}$$

In the case of head sea, there is no contribution from M_z, therefore, only locations in the top edge and bottom edge are studied. Axial stresses at the three sections for different wave periods (wave amplitudes are set to 1m) are shown in Figure 4.27 to Figure 4.29.

From the shape of the stress spectrum, it could be confirmed that the main contribution to the axial stress in the pontoon is the bending of the pontoon about the y-axis, M_y. There is also no surprise that the stress exhibits the same oscillatory behavior at small wave period.

From these figures, it is confirmed that, stress level at the top edge is higher than the bottom edge and the stress level at Section 1 is larger than others due to the larger level arm.

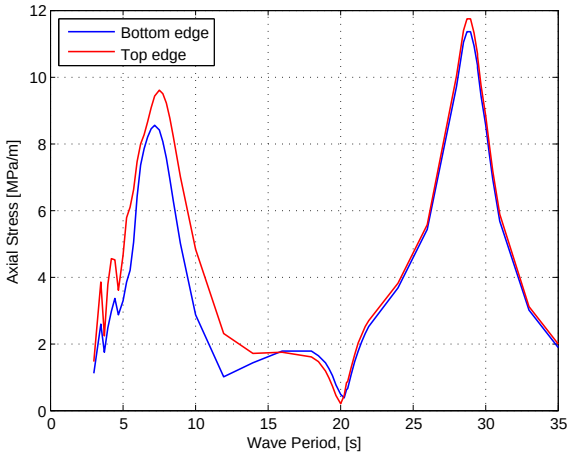

Figure 4.27: *Axial stress spectrum at section 1 (head sea)*

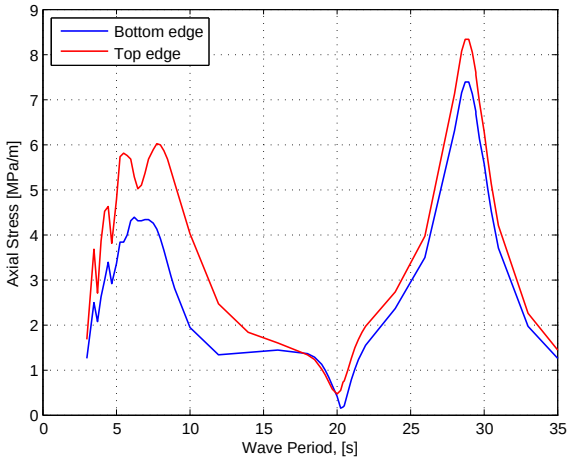

Figure 4.28: *Axial stress spectrum at section 2 (head sea)*

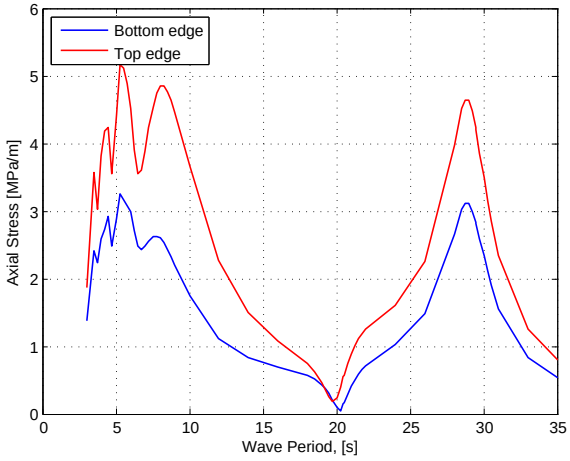

Figure 4.29: *Axial stress spectrum at section 3 (head sea)*

4.4.6 Design Wave Check

For simplicity, the 50 year extreme condition EX is used to check the initial design. According to DNV standard [76]:

$$H_{\max,50} = 1.86 H_{s,50} = 1.86 \times 15.6 = 29.02m \tag{4.33}$$

$$14.0s = 11.1\sqrt{\frac{H_{s,50}}{g}} \leq T \leq 14.3\sqrt{\frac{H_{s,50}}{g}} = 18.0s \tag{4.34}$$

From Figure 4.27, it is seen that the stress level for $T = 14.0s - 18.0s$ is relative low. The largest axial stress associated with the maximum 50 year wave will then be:

$$\begin{aligned} \sigma_{x\,\max,50} &= \sigma_x\,(T = 16.0s) \times \frac{H_{\max,50}}{2} \\ &= 1.72 \times 14.51 \\ &= 24.95MPa \end{aligned} \tag{4.35}$$

This value is well below the yield stress for normal steel. Therefore, the structure could stand this design wave.

However, as indicated above, this design wave approach cannot always give the most dangerous situation. To improve the prediction, long term scatter diagram should be used to better describe the sea state, which is not dealt in this thesis.

4.5 Sensitivity Analysis

4.5.1 Mesh Convergence Study

Three mesh density levels are used to check the convergence of mesh size of the Panel Model, from coarse mesh (4m), medium mesh (2m, corresponding to the mesh density used in the initial design) to fine mesh (1m). This study is performed before the initial design procedure, but it's included in this chapter for ease of readying.

The different meshes are shown in Table 4.19 and Figure 4.30, the medium mesh of the Panel Model could be viewed from Figure 4.6.

Table 4.19: *Mesh levels for the convergence study*

Mesh Level	Mesh Density [m]	Number of Panel Elements
Coarse Mesh	4	576
Medium Mesh	2	2377
Fine Mesh	1	8937

Since in this study the mass model is kept the same, the only difference lies in the mesh of Panel Model, which determines the geometry of the semi-submersible and receives

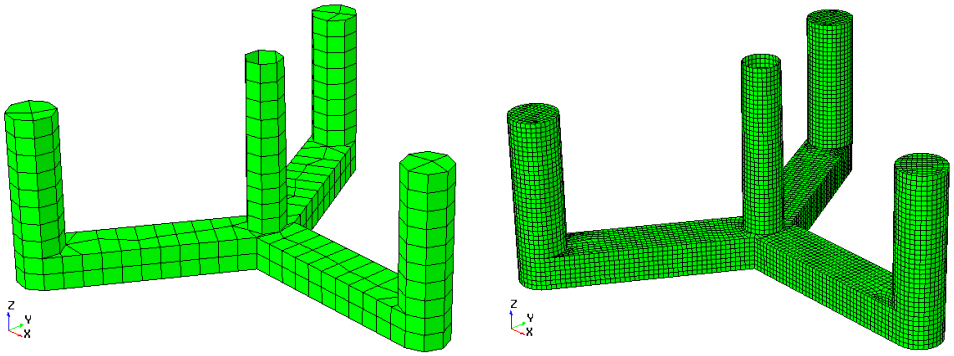

Figure 4.30: *Mesh for the Panel Model (Left: Coarse Mesh, Right: Fine Mesh)*

pressure from the water. In this thesis, due to limited time, only convergence study on hydrostatic behavior is performed.

For hydrostatic performance, three parameters that are mainly associated with the Panel Model are studied: Metacentric Height GM, Vertical Center of Buoyancy and Displacement. Results and relative errors to the results of fine mesh are shown in Table 4.20.

Table 4.20: *Mesh convergence study of hydrostatic behavior of the semi-submersible platform*

	GM [m]		VCB [m]		Displacement [t]	
Mesh Density	Value	Relative Error	Value	Relative Error	Value	Relative Error
Coarse	8.01	14.0%	-13.96	1.4%	13591172	3.3%
Medium	9.05	2.8%	-13.81	0.3%	13955497	0.7%
Fine	9.31	0.0%	-13.77	0.0%	14049702	0.0%

It is seen from the above table that the relative error between medium mesh and the fine mesh is less than 3%, which is already smaller than the default error (5%) in the HydroD software for stability analysis. Therefore, from the consideration of balance of computational time and accuracy, the medium mesh with mesh density 2m is chosen in all the previous analysis.

4.5.2 Wave Direction

As discussed in Section 4.3.1, wave direction will not affect metacentric height of the semi-submersible platform. Therefore, there is no need to perform a sensitivity study about wave directions on stability behaviour.

In this section, the sensitivity of hydrodynamic performance of the semi-submersible platform to different wave directions is studied. Due to the yaw capability of the wind turbine, the wind direction is assumed to be always align with the wave direction, i.e. no wind wave misalignment is considered. The wave direction varies from 0° (head sea, along positive x-axis) to 180° with a step of 30°.

It is seen from Figure 4.31 that, heave RAO does not change for different wave directions. It is reasonable since heave motion is associated with hydrodynamic loads acting on the

vertical direction, which is not related to the wave direction.

However, from Figure 4.32, it is seen that pitch RAO varies for different wave directions. It is interesting to notice that, the pitch RAO curves overlaps for wave directions of 0° and 180°, 30° and 150° and 60° and 120°. Besides, the pitch RAO is smallest for wave direction of 90°, and increases with the wave direction is further away from 90°. This is because that the pitch motion is associated with moment about the rotational axis that is normal to the wave direction. Therefore, pitch RAO is related to the projection width normal to the wave direction. As indicated in Figure 4.33, the effective width reaches minimum at 90°.

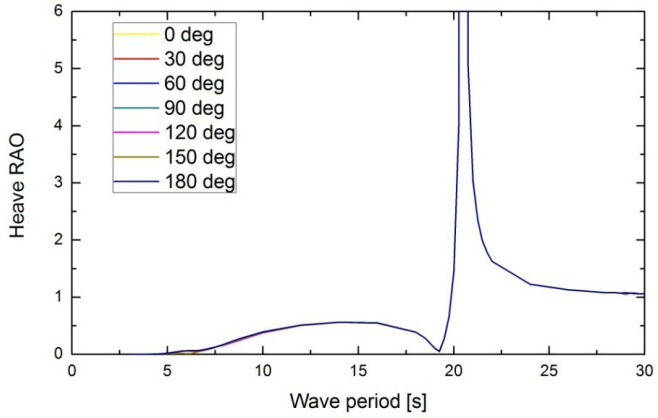

Figure 4.31: *Sensitivity analysis of heave RAO on wave directions, without viscous*

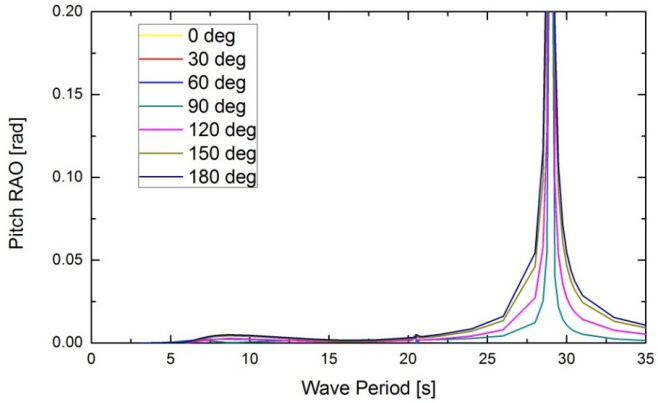

Figure 4.32: *Sensitivity analysis of pitch RAO on wave directions, without viscous*

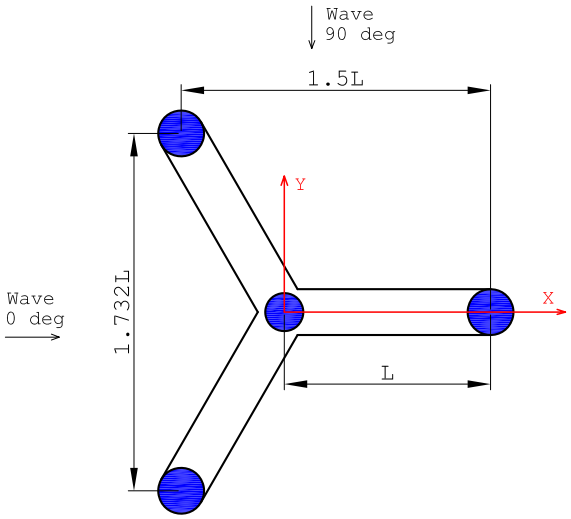

Figure 4.33: *Effective width of semi-submersible platform for different wave directions*

4.5.3 Main Dimension

The sensitivity analysis of the main dimensions of the semi-submersible is a must before future optimization of the semi-submersible platform design. In this section, the dimension of pontoon length, pontoon width, pontoon height, operation draft and side column diameter are varied respectively, and their influence on semi mass, displacement, static heeling angle and heave natural period are analyzed. In all the sensitivity analysis, the design is accepted when the difference of mass and buoyancy is less than 5% (default value in HydroD), otherwise the ballast design will be changed to meet the criteria. Due to limited time, the analysis is performed based on hand calculations as have been done previously in the preliminary design.

Pontoon Length

Pontoon length influences the pontoon volume, which will affect the semi mass and displacement resulting in larger mass (also added mass) thus larger heave natural period. More importantly, the change of pontoon length will lead to a big change of water area inertia due to the change of level arm, which will affect the static heeling angle greatly.

The results are shown in Figure 4.34, results are presented as relative error to the initial value (value from initial design). It can be confirmed that the change of pontoon length has a much larger influence on static heeling angle than other studied characteristics. It should also be noted that the influence on the static heeling angle has a different sign, which means the static heeling angle decreases when the pontoon length increases.

Pontoon Width

Pontoon volume is affected by the change of pontoon width, while the water area and water area inertia are kept the same. It would also have some influence on the added mass

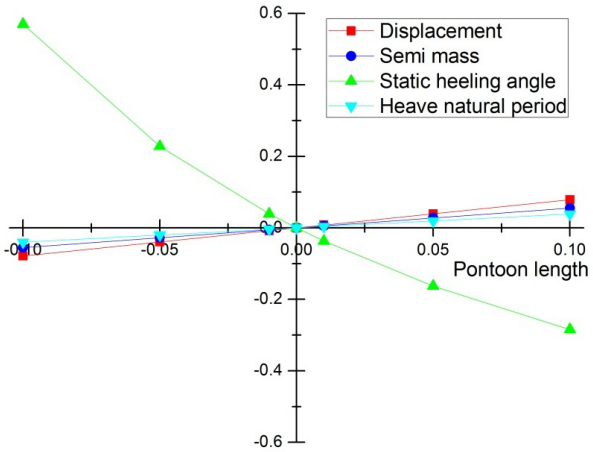

Figure 4.34: *Sensitivity analysis of pontoon length (relative error)*

coefficient as well as the drag coefficient, which are neglected in this sensitivity analysis.

It can be seen from Figure 4.35 that displacement changes with the same speed of pontoon width, while semi mass and heave natural period changes with half of the speed. The static heeling angle changes a lit bit due to the slight change of vertical center of gravity.

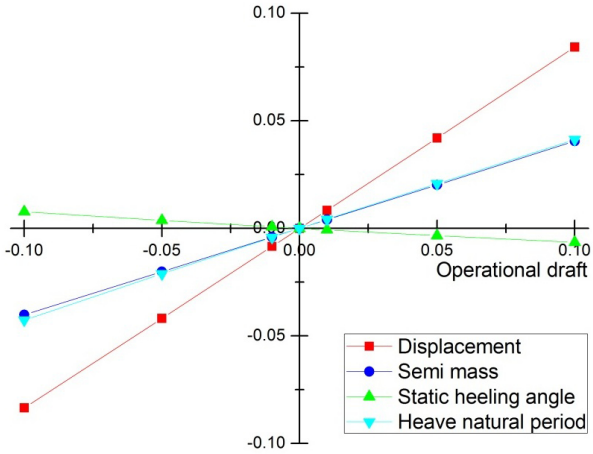

Figure 4.35: *Sensitivity analysis of pontoon width (relative error)*

Pontoon Height

Pontoon height has an influence of pontoon volume and relative larger effect on the vertical center of gravity and buoyancy than other pontoon dimensions.

From Figure 4.36, it can be learned that the influence of pontoon height is similar to that of pontoon width.

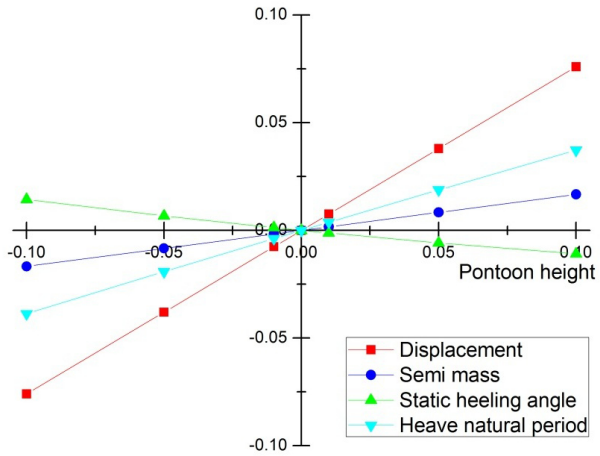

Figure 4.36: *Sensitivity analysis of pontoon height (relative error)*

Operational Draft

The operational draft will mainly influence the submerged volume and the center of gravity and center of buoyancy. It will also affect the free board, which is not discussed in the sensitivity analysis.

It is noted from Figure 4.37 that the different draft does not affect the semi mass, but changes the displacement due to the change of submerged volume (as a results of ballast water). The change will also have an effect on the static heeling angle due to the change of relative vertical distance between center of gravity and center of buoyancy.

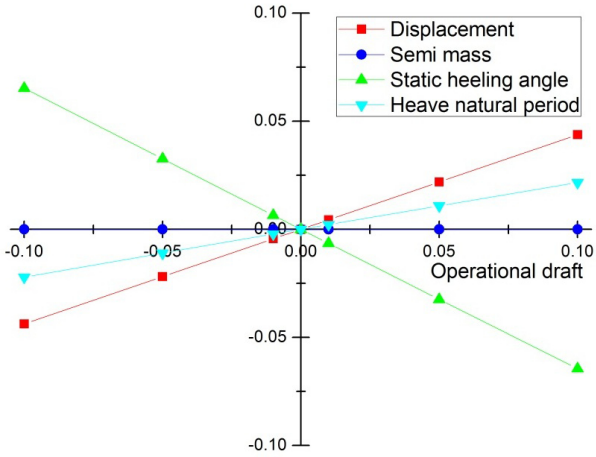

Figure 4.37: *Sensitivity analysis of operational draft (relative error)*

Side Column Diameter

Side column diameter influences the submerged volume, as well as the water area which will affect the static heeling angle and heave restoring coefficient. The change of water

area will also affect the hydrodynamic force acting on the semi-submersible platform, which is not discussed in this sensitivity analysis.

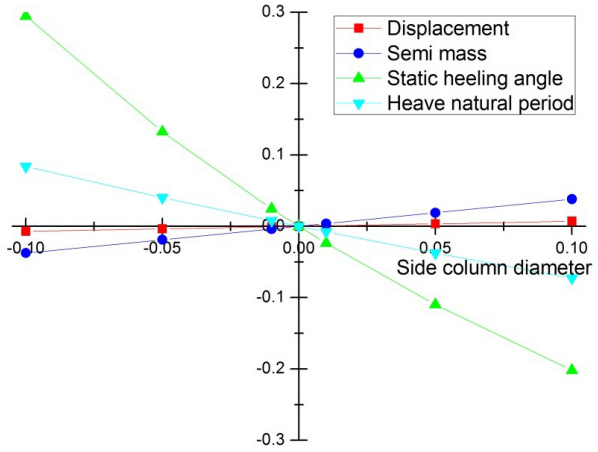

Figure 4.38: *Sensitivity analysis of side column diameter (relative error)*

It can been confirmed from Figure 4.38 that, the change of side column diameter mainly influences the static heeling angle and heave natural period due to the change of water area as discussed above. It should be noted from the figure that the static heeling angle and heave natural period are inversely proportional to the side column diameter.

Summary

In this summary, the influence of change of dimensions on each characteristic is collected.

It can be concluded from Figure 4.39 that:

- Displacement is sensitive to the pontoon dimensions, but no sensitive to the column diameter.
- Semi mass is generally not that sensitive to the change of dimensions.
- The static heeling angle is inversely proportional to all studied variables, which is most sensitive to the pontoon length and secondly side column diameter.
- Heave natural period is most sensitive to the side column diameter.

It should be well noted that the conclusions obtained in this section are based on hand calculations using simplified formulas. However, it still provides some insight into the relation between dimensions of the semi-submersible platform and its characteristics.

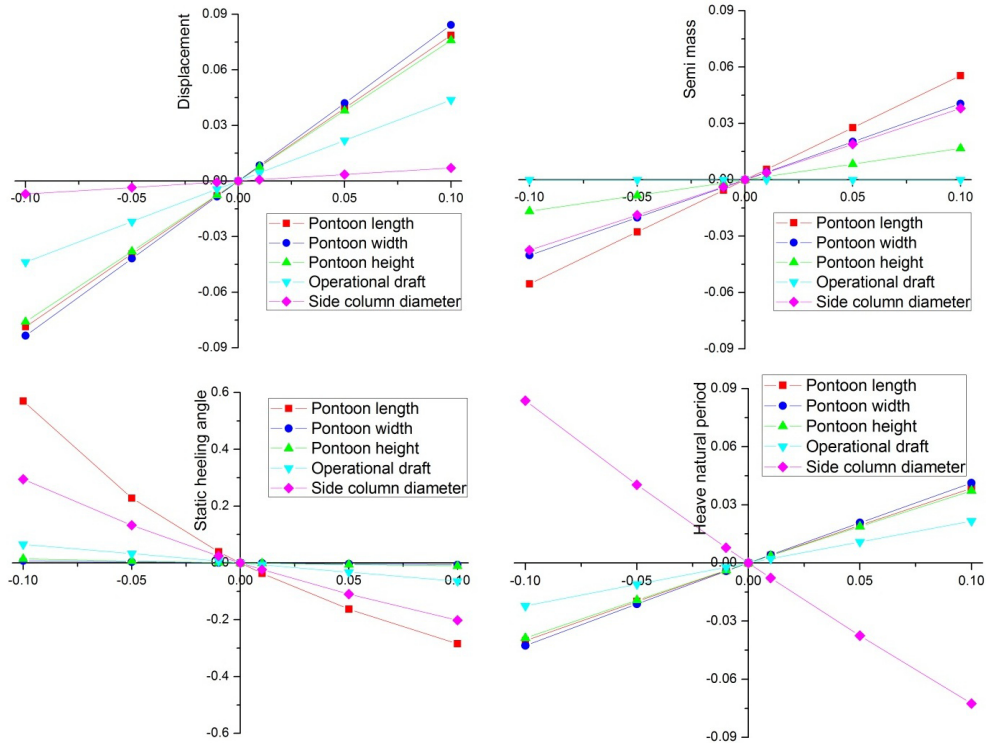

Figure 4.39: *Sensitivity analysis of semi-submersible platform characteristics (upleft: Displacement; upright: Mass; downleft: Static heeling angle; down right: Heave natural period)*

4.6 Summary

So far, an initial design of the semi-submersible platform to support the 10MW wind turbine has been successfully carried out. A summary of the main parameter and characteristics of the initial design is provided in Table 4.21.

Table 4.21: *Key parameters of the initial design of the semi-submersible wind turbine*

Dimension			Property		
Turbine Power	10	MW	Turbine mass	1305	t
Hub height	119	m	Semi mass	2588	t
Side column diameter	10	m	Displacement	13955	t
Center column diameter	8.3	m	VCG	-5.7	m
Pontoon length	45	m	VCB	-13.8	m
Pontoon height	7	m	GM	9	m
Characteristic length	67.5	m	Static heeling angle	8.7	deg
Operation draft	20	m	Heave natural period	20.5	s
Free board	15	m	Pitch natural period	29.5	s

Chapter 5

Implementation of Second Order Wave Loads

5.1 New Mesh Design

As mentioned in Section 2.3.2, in order to estimate the contribution from second order velocity potential, a free surface mesh is required together with the panel mesh of the semi-submersible platform. In order to make sure that the meshes match each other exactly along the water line, the free surface mesh and the semi-submersible platform mesh need to be designed at the same time. Besides, the second order force calculation usually requires higher mesh quality and resolution as the second order terms are more sensitive to mesh size and thus much more difficult to evaluate.

Therefore, the original panel mesh used in initial design need to be redesigned together with the new free surface mesh.

5.1.1 New Mesh for Free Surface Model

To begin with, a coarse mesh for the free surface is designed. The boundary of the free surface is designed to be a circle with a diameter set equal to the water depth, 200m. Due to the rotational symmetry of the whole model, mesh of the 1/6 model is enough to establish final mesh for the whole model.

First of all, the free surface domain is divided into two zones. The inner zone, which has a diameter of 80m from the semi-submersible platform center, is designed to have finer elements than the outer zone. Only first order quad elements are used in the meshing to improve the efficiency and accuracy of later computations. Besides, featured edges with number of elements specified along each edge are used to control the mesh density and quality. Additionally, a linear expansion of element size is used along all straight featured edges to smooth the transition of element size and to reduce the total number of elements. While the ratio of expansion at the inner zone is calculated by the software, the expansion

ratio along the featured edge of the outer zone is set to 1.25 with 9 elements to reach the final required diameter of 200m.

The mesh of the 1/6 free surface model together with featured edges is shown in Figure 5.1. An enlarged figure showing details of the inner zone is also provided. For the meshing of the inner zone, it should be well noted that only for certain combination of number of elements along each featured edges will give good results (no triangle elements). In the presented case, the numbers of elements along featured edges in the inner zone are shown in Figure 5.1: 2 elements along the 1/6 center column (Cen-col); 8 elements along the 1/2 side column (Sid-col); 18 elements along the 1/6 circle between the inner and outer zones (Curve); 15 elements and 6 elements along the bottom lines (Down1 and Down2) and 25 elements along the oblique side (Up). Elements along curves are uniformly distributed while elements along straight lines are linearly distributed. In addition, two layers of fine mesh are designed close to the columns to improve the mesh quality of the free surface close to the structure. The total number of elements for the first mesh of the 1/6 free surface model is 292.

Then the mesh of the 1/2 free surface model can be obtained by rotating and mirroring the mesh of the 1/6 model, which is shown in Figure 5.2. The total number of elements reaches 876, which is well below the limit of 3000 as set by the DNV software HydroD [64].

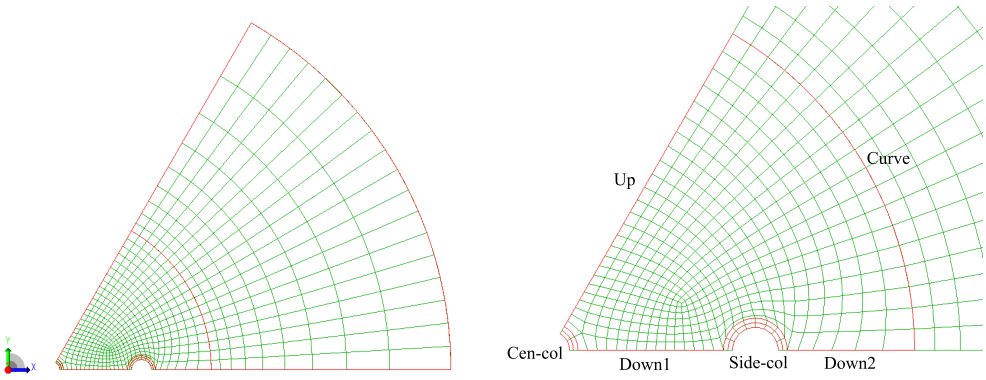

Figure 5.1: *New mesh of the 1/6 free surface model (red lines are featured edges. The right figure shows the enlarged inner zone with featured edge names)*

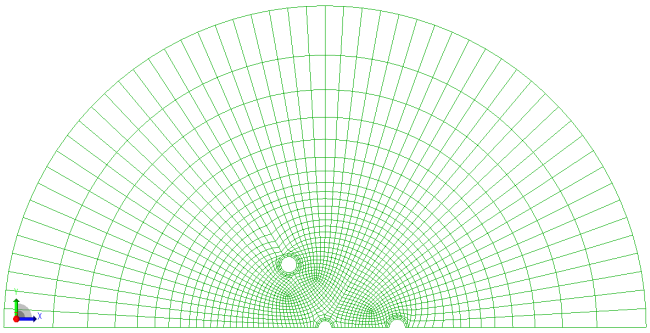

Figure 5.2: *New mesh of the 1/2 free surface model*

5.1.2 New Mesh for Semi-submersible Platform

The mesh of the semi-submersible platform model is re-designed to match the mesh nodes of the free surface model exactly at water line. Similarly, a 1/6 model is used to design the mesh that can be later used to establish the 1/2 model. The mesh quality and density are also controlled by featured edges. In practice, the same featured edges at water line are used in both free surface model and semi-submersible platform model to ensure the generated mesh of the semi-submersible platform model matches exactly that of the free surface model.

The mesh of the 1/6 semi-submersible platform model with featured edges is shown in Figure 5.3. The mesh of the 1/2 semi-submersible platform model is obtained in the same way as the mesh of the 1/2 free surface model, which is shown in Figure 5.4. Overall panel element size for this model is around 2m*2m. The total number of panel elements for this 1/2 model is 1263.

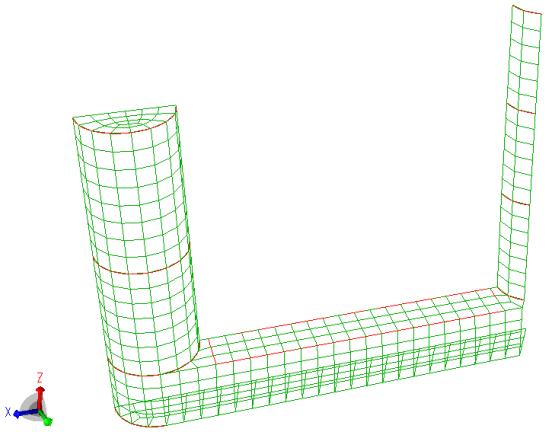

Figure 5.3: *New mesh of the 1/6 semi-submersible platform model (red lines are featured edges)*

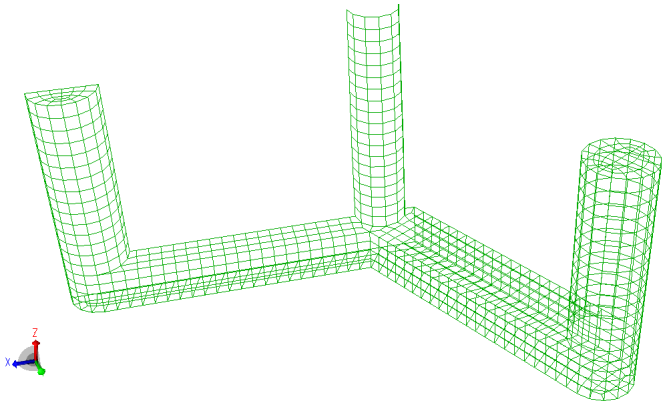

Figure 5.4: *New mesh of the 1/2 semi-submersible platform model*

5.1.3 New Mesh for the Whole Model

Figure 5.5 gives an overview of the free surface mesh and the floating wind turbine at the initial position. Figure 5.6 and Figure 5.7 show the details of the contact area of the semi-submersible platform with the free surface. It can be confirmed from these graphs that the mesh of the free surface model matches the mesh of the semi-submersible platform at water line.

The whole mesh is regular and with good shape, except for few skewed elements (higher relative Jacobi) around the side columns. It is therefore accepted that the mesh quality is good enough to be used to carry out later calculations.

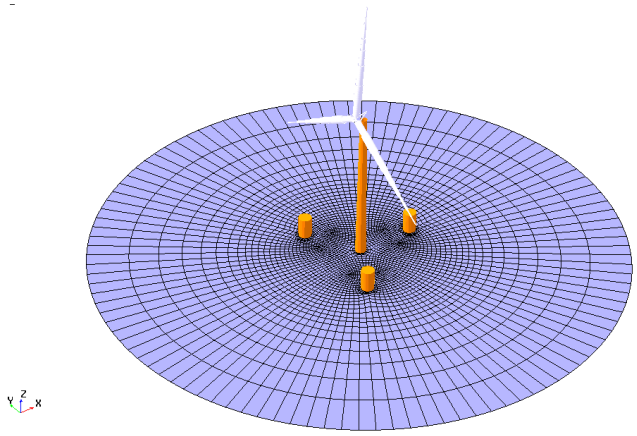

Figure 5.5: *Overview of the whole model (only mass model and free surface model are shown)*

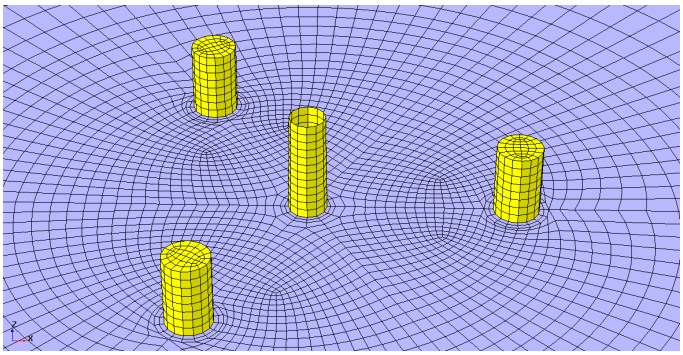

Figure 5.6: *Mesh of the free surface with the semi-submersible platform (topview)*

5.2 Mean Drift Force with Mesh Convergence Study

5.2.1 Mean Drift Force for the New Mesh Design

The mean drift force on the semi-submersible platform are investigated by applying the conservation of fluid momentum (CFM) with far field solution (first order solution, based on momentum conservation in three horizontal dofs) as well as the direct pressure integration (DPI) (corresponding to diagonal terms of QTF). The calculations are performed

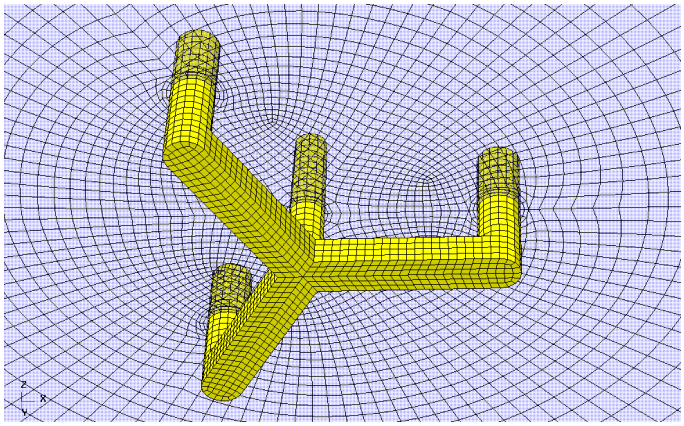

Figure 5.7: *Mesh of the free surface with the semi-submersible platform (bottomview)*

by HydroD. Results of mean drift wave loads on the semi-submersible platform by CFM in three horizontal dofs and by DPI in six dofs are shown in Figure 5.8. Results of mean drift wave loads in wave direction of 30° and 60° by CFM are shown in Figure 5.9. A detailed comparison of mean drift force in surge by the two different methods is shown in Figure 5.10. Results from these figures are discussed in details in the following paragraph.

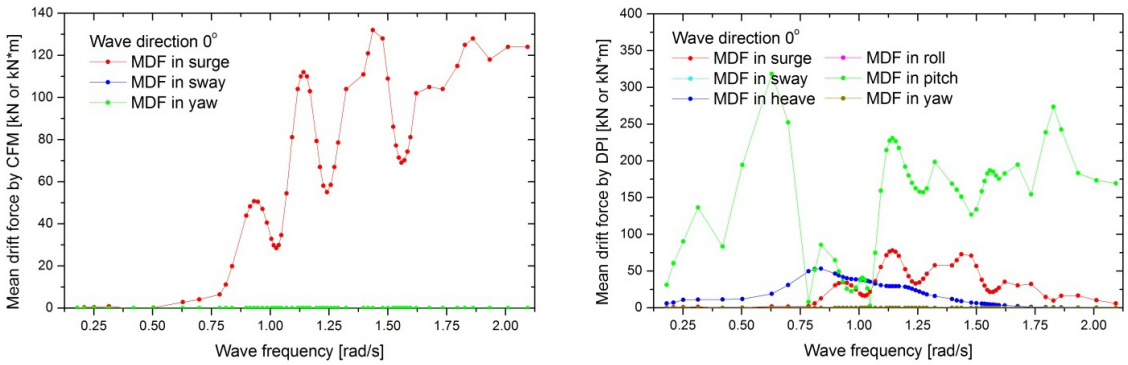

Figure 5.8: *Mean drift force in wave direction of 0° (left: conservation of fluid momentum, CFM; right: direct pressure integration, DPI)*

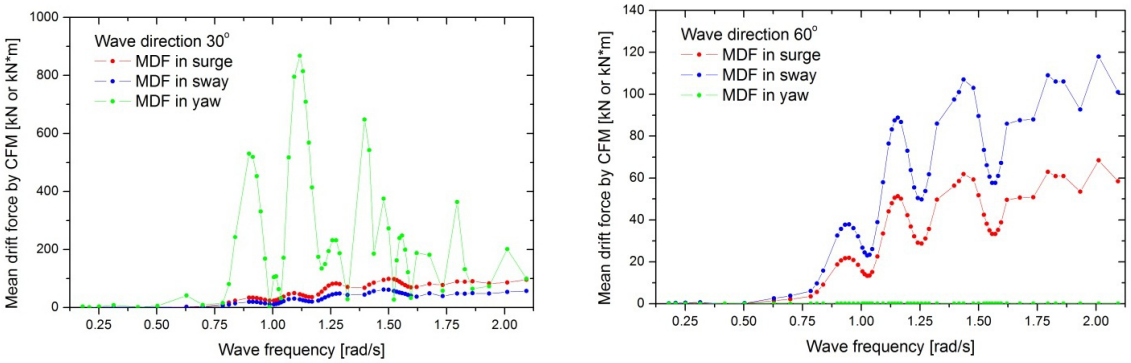

Figure 5.9: *Mean drift force in wave direction of 30° and 60° by CFM*

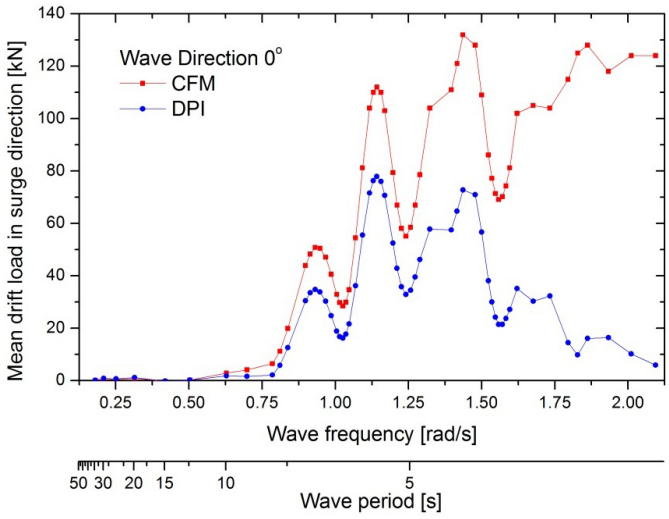

Figure 5.10: *Comparison of mean drift force in surge by CFM and DPI*

Asymptotic value

First of all, it is observed that the mean drift force is only significant for high wave frequencies (>0.75rad/s, as shown in Figure 5.10). That is because mean drift force is associated with body's capability in generating waves. For long waves, the body tends to follow the waves, diffraction effects are small, mean drift force is close to zero. Consequently, at high frequencies (short waves) the waves are reflected completely and the mean drift force has a finite asymptotic value.

This value could be checked by analytical formulas. For short waves with wave amplitude ξ_a, the mean drift force could be estimated by using the extended Maruo's formula [25]:

$$\overline{F_i} = \frac{\rho g \xi_a^2}{2} \int_L [\sin(\theta + \beta)]^2 n_i dl \quad i = 1, 2, 6 \tag{5.1}$$

In the case of a cylinder with radius r, the maximum mean drift force in surge/sway reads:

$$\overline{F_i} = \frac{2}{3} \rho g r \xi_a^2 \quad i = 1, 2 \tag{5.2}$$

Therefore, the analytical solution to this problem would be (neglecting shadow effect):

$$\begin{aligned} \overline{F} &= \frac{2}{3} \rho g r \xi_a^2 = \frac{2}{3} \times 1025 \times 9.81 \times (3 \times 5 + 4.15) \times 1^2 \\ &= 128kN \end{aligned}$$

This result agrees quite well with the numerical results of mean drift force obtained by CFM as shown in Figure 5.10. As indicated by Equation (5.2), the total mean drift force is independent of wave directions, which could be proved in Figure 5.9 by examining the surge and sway force in 30° and 60° direction.

Wave directions

From Figure 5.8, it is seen that mean drift loads in sway, roll and yaw become zero at wave direction of 0°. Also from Figure 5.9, it is observed that mean drift loads in yaw become zero when the wave direction is along one of the pontoons. All these fact confirms that the established computational model is able to reproduce the symmetric property of the semi-submersible platform.

Cancellation effects

Additionally, cancellation effects on the mean drift loads are observed in surge/sway, which is clear from Figure 5.10. This is similar to what happens when calculating the sectional loads in the initial design. The cancellation takes place when the characteristic length of the platform covers several full wave lengths. However, due to the complexity of the platform, the characteristic length Lc of the platform in surge direction can range from 57.5m (excluding the radius of side columns) to 77.5m (including the radius of side columns). This effect is tabulated in Table 5.1 (cancellation frequencies are obtained from Figure 5.10).

Table 5.1: *Comparison of wave lengths corresponding to cancellation of mean drift force in surge/sway with characteristic length of the platform*

Cancellation frequency [rad/s]	Wave length [m]	Lc/wave length (Lc=57.5m)	Lc/wave length (Lc=77.5)	Remark
1.026	58.6	1	1.3	1*Lc
1.241	40	1.4	1.9	2*Lc
1.558	25.4	2.3	3.1	3*Lc

CFM and DPI

Finally, as shown in Figure 5.10, a big deviation in the mean drift force in high wave frequency region is observed by the two different methods, CFM and DPI. As discussed in Section 2.3.1, in the case of mean drift loads in horizontal dofs, CFM reduced to a far-field solution which could be estimated more simply and accurately than DPI. Moreover, as indicated by Faltinsen [25], the expression for DPI involves terms that counteract each other and may make it difficult to estimate the loads accurately.

In order to obtain reasonable results of QTFs (based on DPI method) for later time domain simulations, the results of mean drift force by DPI with regard to CFM must be improved. This calls for a mesh refinement of the model and a mesh convergence study of the mean drift force by DPI.

5.2.2 Mesh Convergence Study

In this mesh convergence study, the meshes of the semi-submersible model and the free surface model are refined step by step to reach a final convergence. The mean drift force

in surge in wave direction of 0° by CFM is used as a target for this convergence study.

Before the mesh convergence study, a sensitivity study is carried out to examine the most important factors that influence the mean drift force obtained by DPI.

Influence of free surface domain

The influence of free surface domain size on the mean drift force is estimated by increasing the free surface domain radius from 200m to 400m by adding 6 extra layers of coarse mesh to the boundary of the original mesh. Results of the mesh and the mean drift force obtained by DPI are shown in Figure 5.11.

It can be seen that free surface domain has no influence on the mean drift loads on the semi-submersible platform. It might be the reason that the mean drift loads is independent on the free surface domain, or it could be concluded that increase of free surface domain size will not improve the DPI mean drift loads results.

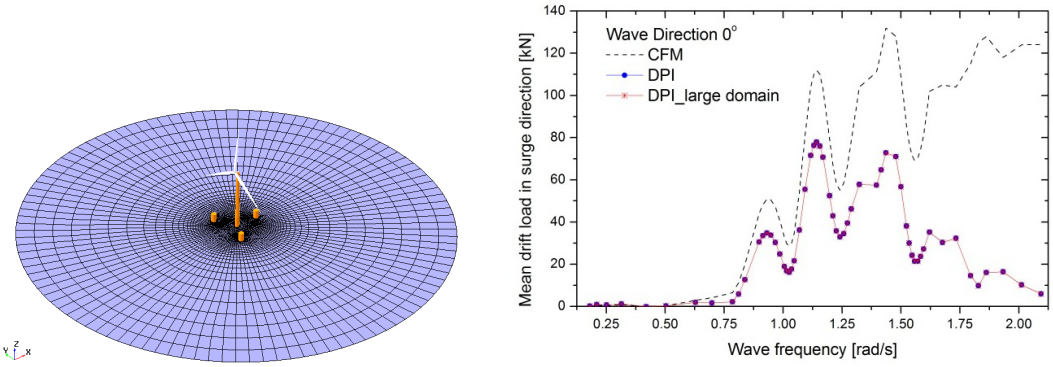

Figure 5.11: *Mesh for the increased free surface domain (left), influence of free surface domain size on mean drift load (right)*

Influence of order of numerical integration

Generally speaking, there are two ways of improving the accuracy of FE results, one is to reduce element size, and the other is to increase the order of numerical integration. By default one node Gauss quadrature is used in the estimation of Greens function and its derivatives. The influence of numerical integration is studied by using a four node Gauss quadrature. Results are shown in Figure 5.12.

It is seen that the result of four node Gauss becomes more unstable for large wave frequencies. This may be caused by the complexity of the model. Therefore, it should be concluded that the increase of order of numerical integration will not improve the results of mean drift loads by DPI.

Influence of pontoon elements size

As indicated by Equation (5.2), theoretically the mean drift force only dependent on the mesh of columns at free surface. Therefore, the mesh of pontoons could be designed to

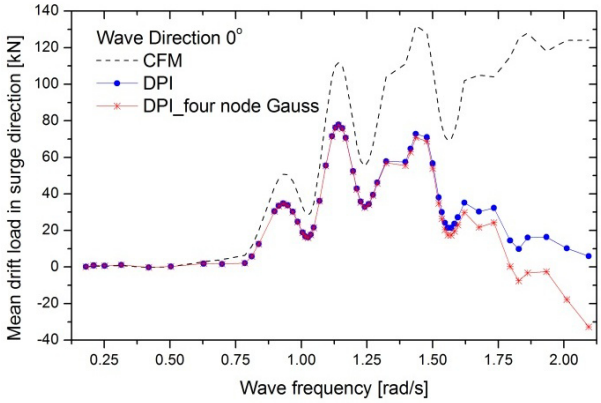

Figure 5.12: *Influence of order of numerical integration on mean drift load*

be coarser than the columns to reduce computational cost. This theoretical conclusion is investigated with different element size on pontoons as shown in Figure 5.13. Results are shown in Figure 5.14.

It is seen from Figure 5.14 that the refinement of pontoon mesh has almost no influence on mean drift load, which proofs the theoretical conclusion discussed above. Therefore, it is advisable to use coarser mesh at pontoons to reduce computational time.

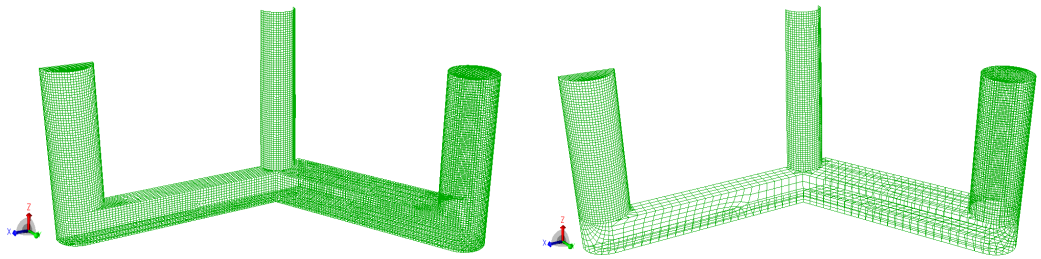

Figure 5.13: *Two sets of mesh of the 1/2 semi-submersible platform model (left: fine pontoon mesh; right: coarse pontoon mesh)*

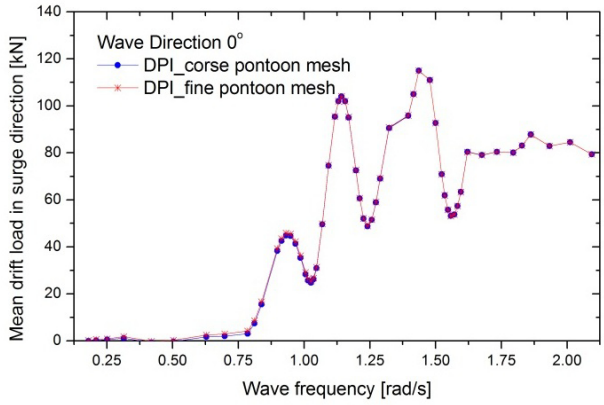

Figure 5.14: *Influence of pontoon mesh size on mean drift load*

Influence of column element size (mesh convergence study)

From previous discussion it can be concluded that none of the modifications including free surface domain size, order of numerical integration or element size of pontoons could help improve the results of mean drift force calculation by DPI. After some trial and error, it is believed that the number of elements at center column and side columns are the two key factors that will influence the results of mean drift load significantly. A corresponding mesh convergence study is carried out in this section.

To start with, the mesh of the free surface model with featured edges is reproduced in Figure 5.15 for the convenience of reading. Four levels of mesh are designed with regard to different element numbers at center column (Cen-col) and side columns (Sid-col). Element numbers at other featured edges are chosen to ensure quality of the overall free surface mesh. The elements of the semi-submersible platform are changed accordingly to match the free surface mesh exactly. As discussed in the previous section, the mesh density of pontoons is kept unchanged during the mesh convergence study to reduce the computational time. Table 5.2 provides an overview of the mesh setup for the mesh convergence study.

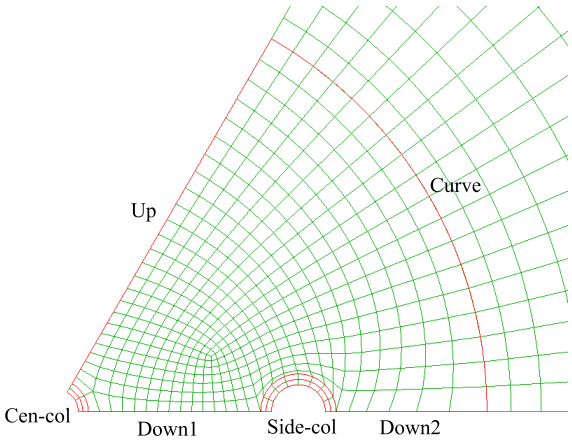

Figure 5.15: *Mesh of the 1/6 free surface model (showing the featured edge)*

Table 5.2: *Number of elements specified on featured edges for different mesh levels*

Mesh Level	Mesh density of columns [m]	Number of elements at Cen-col	Number of elements at Sid-col	Number of elements of 1/2 surface model	Number of elements of 1/2 semi model
1	2	2(12)[1]	8(16)	876	1263
2	1	4(24)	16(32)	1926	2913
3	0.5	8(48)	32(64)	2757	8463
4	0.4	10(60)	40(80)	2799	12684

[1]Here, 2 refers to the element number in the 1/6 model and (12) refers to the element number in the full model

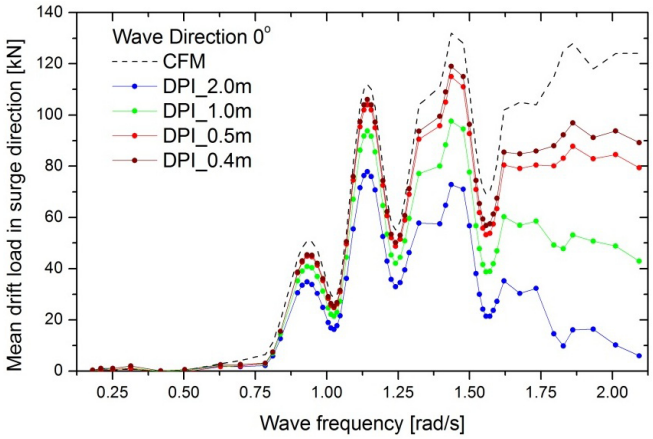

Figure 5.16: *Results of mean drift force in surge direction from mesh convergence study*

Results of the mesh convergence study with regard to mean drift force in surge are shown in Figure 5.16. It is seen that with the refinement of column element size, the results of mean drift force by DPI improves significantly. Taking into account both accuracy and computational cost, the mesh level 3 with column mesh density of 0.5m is accepted and would be used in all further computations.

5.2.3 Final Mesh

The final mesh setup for the free surface model and semi-submersible model is tabulated in Table 5.3. For the free surface model, as shown in Figure 5.17, mesh level 3 is adopted resulting in a total number of elements of 2757.

The same mesh level is adopted for the semi-submersible platform, but only for the mesh of columns, which is further limit to a region ±5m around the design water line (corresponding to the design draft). For the rest region of the semi-submersible platform, mesh level 2 is used. A transition zone is applied to smooth the change of mesh density. This modification is believed not to influence the accuracy much since it is shown from previous study that the mean drift force only depends on the mesh resolution at water line. At the meantime, by limiting the region of mesh refinement, the total number of elements for the semi-submersible platform model reduces from 8463 to 5620, which saves a lot of computational cost. The final mesh of the semi-submersible platform is shown in Figure 5.18

Table 5.3: *Final mesh setup*

Model	Number of elements at featured edge					Mesh density	
1/6 free surface	Cen-col 8	Sid-col 32	Down1 14	Down2 12	Up&Curve 23	Columns 0.5m	
1/6 semi-submersible	Cen-col 8	Sid-col 32	Cen-col*[1] 4	Sid-col* 16		Refined zone 0.5m	Elsewhere 1m

[1]* corresponding to featured edge in the coarse mesh zone, refer to Figure 5.18

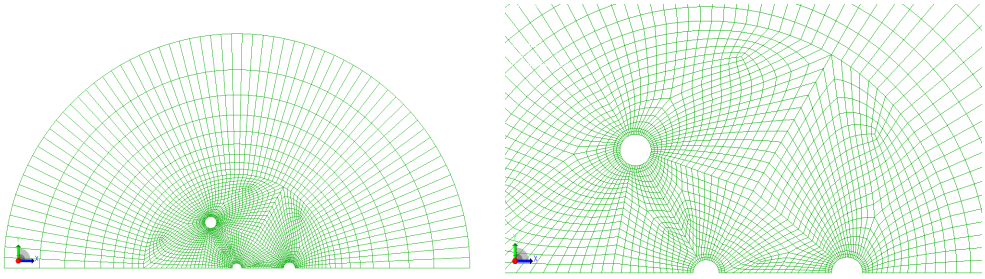

Figure 5.17: *Final mesh of 1/2 free surface model (left: overall mesh; right: enlarged inner zone)*

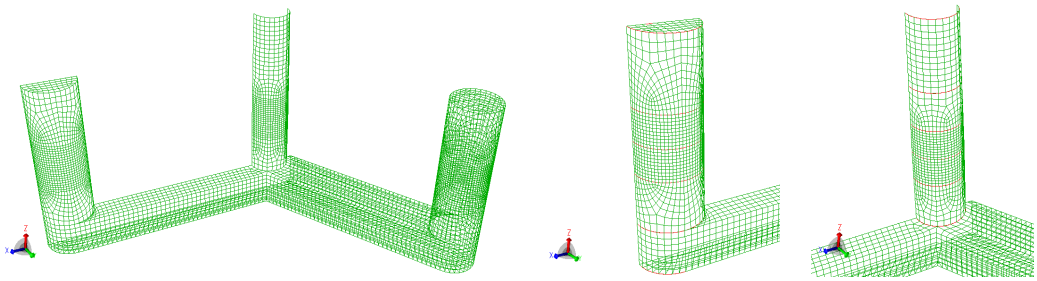

Figure 5.18: *Final mesh of the 1/2 semi-submersible model (left: overall mesh; middle: mesh of side column; right: mesh of center column)*

5.3 Quadratic Transfer Function

Based on the final mesh obtained in the previous section, second order difference frequency quadratic transfer functions (QTF) can be obtained. The computation is performed in HydroD. Wave frequency range of 0.025rad/s to 1.25rad/s with step of 0.025rad/s is chosen for the QTF calculation. It should be noted that the QTF calculation is around 20 times more time consuming than that of the first order hydrodynamic force. It should also be noted that, it is important to include difference frequencies that corresponds to the natural frequencies of the floating wind turbine. However, since in this thesis QTF calculations are performed before the mooring system design, platform natural frequencies are not considered when choosing the frequency range. The natural frequencies used in the following are obtained after the mooring system design.

The second order difference frequency surge QTF is shown in Figure 5.19. It is seen that the off-diagonal QTF terms become larger for higher frequencies. Besides, it is also observed that the change of QTF from the diagonal to near surge natural frequency (indicated by the dashed lines) is not small, which makes the validity of Newman's approximation into question. Similar results are also found by Bachynski [52] for a TLP floating wind turbine.

Also in Figure 5.19, second order difference frequency surge force on the semi-submersible platform at surge natural frequency by Newman's approximation is compared with that by QTF. It is seen that Newman's approximation underpredicted the surge force for incoming wave frequencies 0.3 rad/s to 0.6 rad/s and for wave frequencies 0.8 rad/s to 1.25 rad/s Newman's approximation either underpredicted or overpredicted the force.

The difference frequency heave and pitch QTFs are shown in Figure 5.20. It is seen that, comparing to the surge QTF, the heave and pitch QTFs changes more quickly near the natural frequencies of heave and pitch respectively. All these results call into questions the validity of Newman's approximation in calculating the second order difference wave forces. This issue will be discussed in the coupled dynamic analysis.

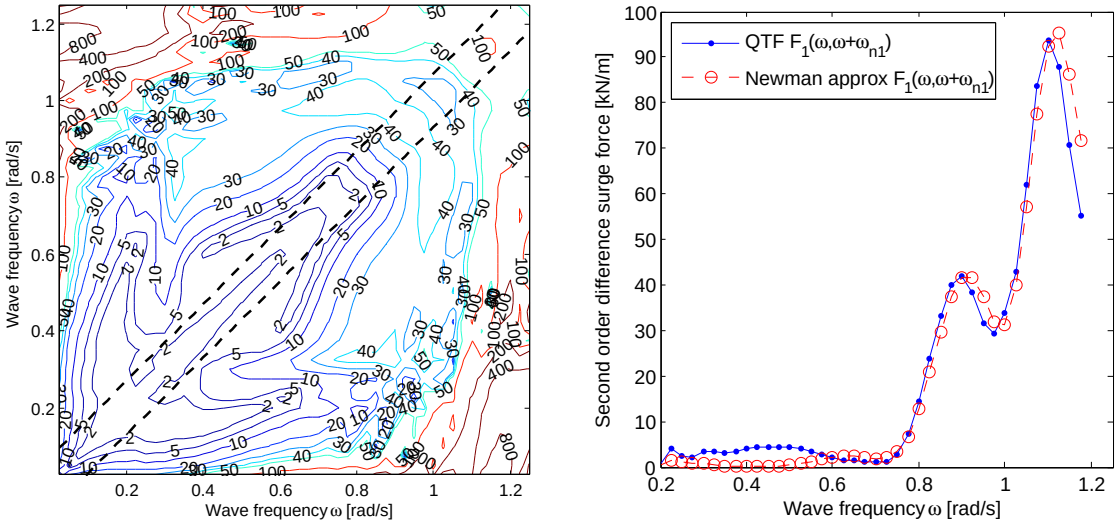

Figure 5.19: *(left) Difference frequency surge QTF, (kN/m). The surge natural frequency is indicated by the dashed lines. (right) Difference frequency surge force at surge natural frequency ω_{n1}, based on QTF and Newman's approximation for the floating wind turbine*

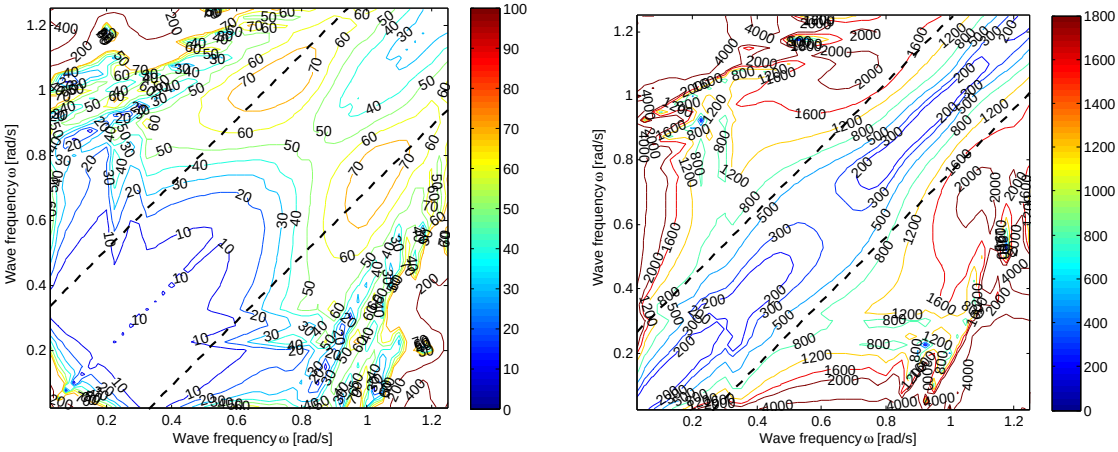

Figure 5.20: *Difference frequency heave QTF (left, kN/m) and pitch QTF (right, kN). The heave and pitch natural frequencies are indicated by the dashed lines*

Chapter 6

Mooring System Design

6.1 Preliminary Design

So far, the design and analysis of the semi-submersible platform are carried out without the mooring system.

In this section, a preliminary mooring system design of the semi-submersible wind turbine is performed. As discussed in Section 1.3, a spread catenary mooring system is chosen for the semi-submersible wind turbine.

6.1.1 The Catenary Theory

For the preliminary mooring system design, only linear static analysis is performed. Furthermore, the effect of elasticity of the mooring line is neglected, which reduced the problem into the classic catenary equations. Following Faltinsen [25] the classic catenary solution could be described by Figure 6.1.

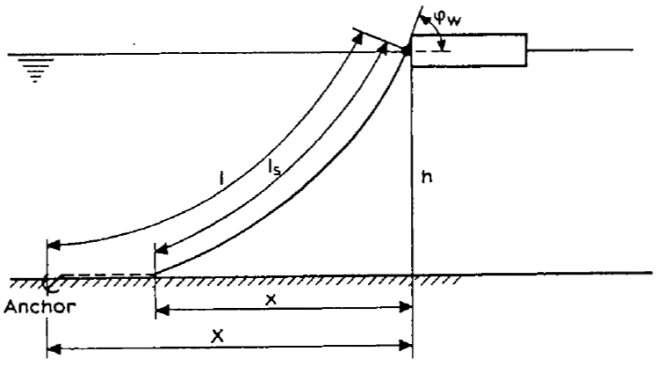

Figure 6.1: *Vessel moored with one anchor line [25]*

In the figure, h is the depth from fairlead to seabed, x is the horizontal distance from fairlead to the contact point of the mooring line with seabed, X is the horizontal distance

between fairlead and anchor, ls is the length of the mooring line that is hanging in water, l is the mooring line total length and φ_w is the mooring line angle at fairlead.

Some key results of the catenary equation are:

$$ls = a \sinh\left(\frac{x}{a}\right) \tag{6.1}$$

$$h = a\left[\cosh\left(\frac{x}{a}\right) - 1\right] \tag{6.2}$$

where

$$a = \frac{T_H}{w} \tag{6.3}$$

T_H is the pretension of the mooring line, corresponding to the horizontal component of the maximum tension $T_{\max}$ at fairlead, while w is the unit weight of mooring line in water:

$$T_{max} = T_H + wh \tag{6.4}$$

The horizontal distance X can be expressed by:

$$X = l - ls + x \tag{6.5}$$

By combining Equation (6.1) and (6.2), we see that

$$ls^2 = h^2 + 2ha \tag{6.6}$$

If no vertical force is allowed at anchor, by setting $ls = l$ in the above equation, we obtain the uplimit value for a:

$$a_{lim} = \frac{l^2 - h^2}{2h} \tag{6.7}$$

And the corresponding uplimit value for the horizontal distance X could be obtained by using Equation (6.2), realizing that $X = x$ in this extreme case:

$$X_{lim} = a_{lim}\sinh^{-1}\left(\frac{ls}{a}\right) \tag{6.8}$$

Then the allowable offset of the vessel could be obtained by using Equation (6.8) and (6.5):

$$\Delta x = X_{lim} - X \tag{6.9}$$

When considering only linear restoring effect, the restoring coefficient of the spread mooring system could be written into:

$$C_{11} = \sum_{i=1}^{n} k_i \cos^2\varphi_i \tag{6.10}$$

where φ_i is the angle between two adjacent lines, and the linear restoring coefficient for one mooring line k_i could be written into:

$$k_i = w\left[\frac{-2}{\left(1 + 2\frac{a}{h}\right)^{\frac{1}{2}}} + \cosh^{-1}\left(1 + \frac{h}{a}\right)\right]^{-1} \tag{6.11}$$

6.1.2 Preliminary Design Requirment and Procedure

The main requirements for the preliminary mooring system include:

Stiffness requirement. The stiffness of the mooring line system should be adequate to keep the offset of the platform within a limit (no vertical force on the anchor), and to keep the natural frequencies of horizontal motions at proper low values.

Strength requirement. The mooring lines should be strong enough to maintain structural integrity (maximum tension of the mooring line should not exceed its breaking strength).

The step by step preliminary design procedure is summarized below:

1. Assume a natural period for surge (80s for this platform) and calculate the required restoring coefficient C_{11}.
2. Use Equation (6.10) to get the linear restoring coefficient for one mooring line k_i after the arrangement of mooring line has been designed (number of mooring lines and the angles between mooring lines).
3. A proper value for the unstreched mooring line length l is assumed. In the current case, $l = 880m$ is initially assumed after some study on the mooring system of the DeepCWind semi-submersible platform at the same water depth [20].
4. Use Equation (6.7) and (6.8) to obtain the uplimit value a_{lim} and X_{lim}. Then a proper value of a is chosen to ensure an adequate offset according to Equation (6.9). An allowable offset around 20% of the water depth is adopted.
5. Use Equation (6.11) to calculate the required weight w. Once w is known, the mooring line properties (chain grade, nominal diameter, stiffness and breaking strength etc.) can be obtained according to offshore guidances, such as DNV-OS-E302 [77] or CMPT [31].
6. Use Equation (6.3) and (6.4) to obtain the pretension and maximum tension.
7. Then, a decay test is performed to check the natural periods of the system. And extreme condition test is also performed to check the strength and offset of the vessel.
8. Modify the parameters until the requirements are satisfied.

6.1.3 Preliminary mooring line design

According to the procedure above, a preliminary mooring line design is performed. Results are summarized in Table 6.1 and a sketch of the mooring system is provided in Figure 6.2.

A uniformly distributed three-line spread mooring system is designed. The fairleads are located at the outside of side columns, at a depth of 15m below the SWL and at a radius of 50m from the platform center. The anchors are located at a water depth of 200m

and at a radius of 879.6m from the platform center. The mooring lines are made from studless grade 4 chain, with a chain nominal diameter of 153mm. Each of the three lines has an unstretched length of 880m, a submerged unit mass of 0.447t/m, an axial stiffness of 2100MN and a catalogue breaking strength of 20MN. All hydrodynamic coefficients are based on the chain nominal diameter. The drag coefficients are obtained from DNV-OS-E301 [29] and the added mass coefficients are assumed by the author according to this DNV standard. Table 6.2 shows the comparison of the mooring system properties with those of the DeepCWind concept [18, 20]. It is shown that the main difference is the increased mooring line diameter and unit mass in the presented design.

Table 6.1: *Preliminary mooring system properties*

Mooring line configuration		
Number of mooring lines	3	[-]
Angel between adjacent lines	120	deg
Water depth	200	m
Depth from fairlead to seabed	185	m
Radius to anchors from platform center	879.6	m
Radius to fairlead from platform center	50	m
Unstretched mooring line length	880	m
Mooring line angle at fairlead	43	deg
Pretension	2190	kN
Mooring line properties		
Chain type	Studless grade 4	
Chain nominal diameter	153	mm
Mooring line unit mass in water	0.447	t/m
Mooring line axial stiffness	2.10E+06	kN
Catalogue breaking strength	2.00E+04	kN
Transversal drag coefficient of mooring line	2.4	[-]
Longitudinal drag coefficient of mooring line	1.15	[-]
Transversal added mass coefficient of mooring line	2	[-]
Longitudinal added mass coefficient of mooring line	1	[-]

Table 6.2: *Comparison of mooring system properties with the DeepCWind concept*

Item	DeepCWind	Presented design	Unit
Wind Turbine	NREL 5MW	DTU 10MW	
Hub height	77.6	119	m
Platform displacement	14265	13955	t
Number of mooring lines	3	3	[-]
Water depth	200	200	m
Depth from fairlead to seabed	186	185	m
Radius to anchors from platform center	837.6	879.6	m
Radius to fairlead from platform center	40.9	50	m
Unstretched mooring line length	835.5	880	m
Equivalent mooring line diameter	76.6	153	mm
Mooring line unit mass in water	0.109	0.447	t/m
Mooring line axial stiffness	753.6	2100	MN

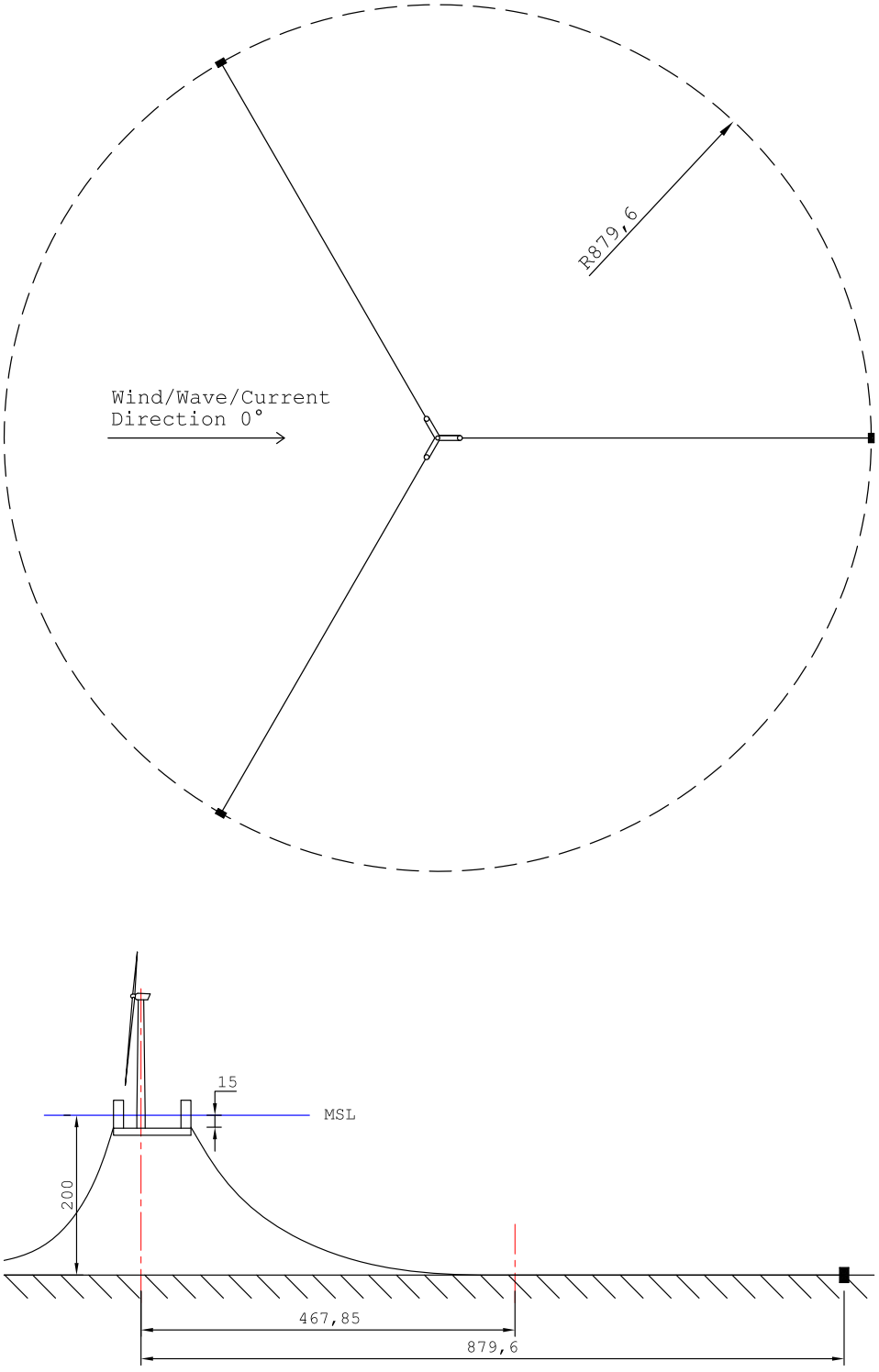

Figure 6.2: *Preliminary mooring line system configuration (topview and sideview)*

6.2 Free Decay Test

Free decay tests in six dofs are performed to check the natural periods of the system. The test is performed at the undisturbed position. Since a prescribed displacement is not supported in DeepC, instead a constant force/moment at the dof is specified to achieve a certain initial displacement, then the force/moment is released to let the platform free vibrate. Results are shown in Figure 6.3 and natural periods are listed in Table 6.3.

It should be well noted that due to coupling of different dofs (especially surge - pitch and sway - roll), the platform will always have some motions in other dofs when performing the free decay test. For the surge free decay test, the largest amplitude in pitch is around 0.5°, while for the pitch free decay test, the largest amplitude in surge is around 1.2m. Similar results are found for the sway and roll free decay tests. These values are not so large comparing to those in the dofs that is being tested. Therefore, results obtained from the free decay tests are believed to be reasonable. The wind turbine in these tests is not modelled, but the correct mass distribution is included in the mass model.

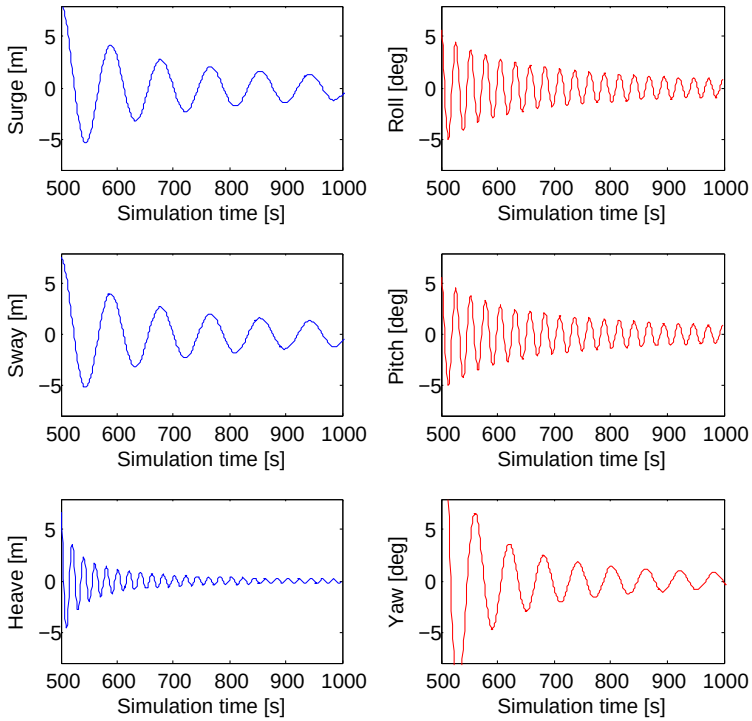

Figure 6.3: *Free decay test of 6 dofs*

Table 6.3: *Natural periods of the platform in 6 dofs*

Degree of freedom	Natural period [s]
Surge/Sway	88.3
Heave	20.3
Roll/Pitch	26.3
Yaw	60.4

The natural period of surge motion from the test is 88.3s, which is close to the value specified (80s) in the preliminary design process. One possible reason for the difference is that nonlinear restoring and elasticity of the mooring line is neglected in the preliminary design process. However, few nonlinear effects are expected since the displacement used in the decay test is small. Another possible cause for the difference is the coupling between surge and pitch motions (mainly due to the coupled added mass terms), as has been previously discussed. More effort will be needed to take this issue further.

Besides, the natural periods of pitch and roll is slightly smaller than the previous value (29.5s) due to the additional stiffness from the mooring system. However, the natural period of heave stays almost unchanged, which means that the mooring system has limited restoring contribution in the heave dof.

6.3 Load-Displacement Test

The load displacement test is performed in surge direction for the mooring system, result is shown in Figure 6.4. It should be noted that due to the arrangement of the mooring lines as shown in Figure 6.2, the mooring line stiffness in 0° direction and 180° direction are different, which is clear from Figure 6.4. The stiffness in 0° direction is approximately 1/2 of the stiffness in 180° direction. This also applies to the limits on excursion defined by Equation (6.9), also shown by red dashed lines. The limit on excursion in 0° direction is 46.5m, while the limitation on excursion in 180° direction is 24.2m.

The linear stiffness in surge at the undisturbed position could be estimated from the curve, which is around 126kN/m. This will give an estimation of the surge natural period of 86s, which is close to the value obtained from the decay test.

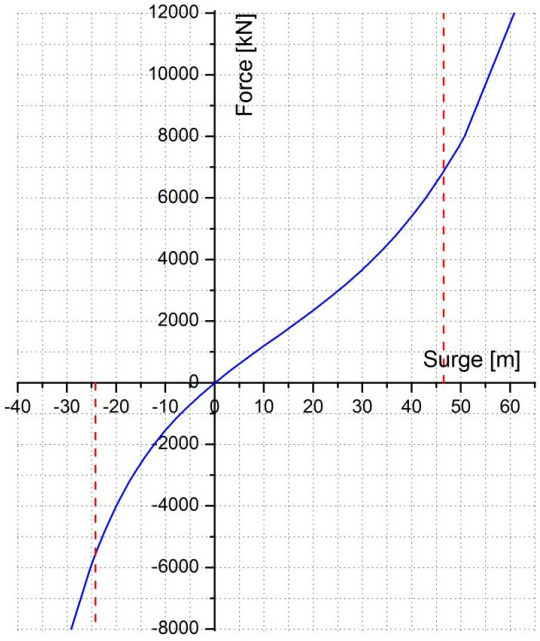

Figure 6.4: *Load excursion curve in surge (two red dash lines show the limits of the offset)*

6.4 Extreme Condition Test

Extreme condition tests are performed to check the extreme mooring line tension as well as vessel offset. As mentioned in Section 6.1.2, the vessel offset should be within the allowable range to avoid vertical forces on the anchor, and the mooring line strength should meet the ULS requirements, here the DNV-OS-E301 [29].

The load case EX is used as 50-year extreme condition for the floating wind turbine system. 20 simulations with each simulation last for 3 hours have been run in DeepC. In these simulations the response of the platform and mooring lines are coupled, while the aerodynamic force is represented by a constant thrust force at hub height. Second order quadratic transfer functions are used to calculate second order forces. Only head wave is considered, no current is specified.

6.4.1 Extreme motion

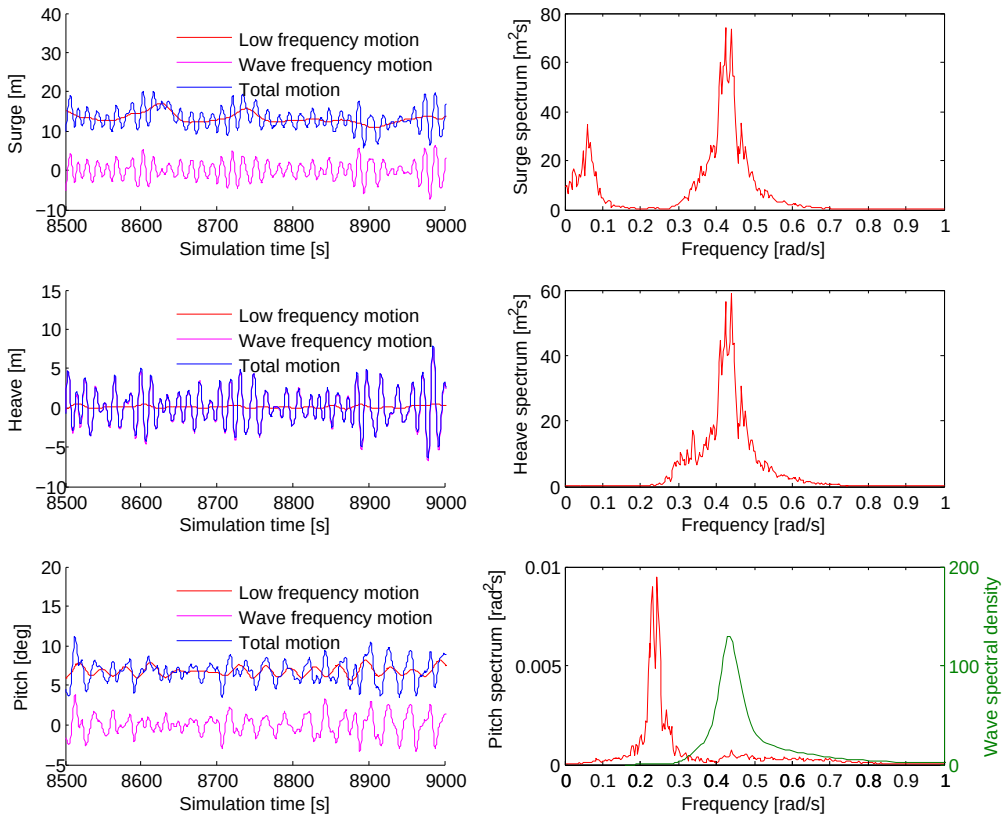

Figure 6.5: *Response of the semi-submersible wind turbine under extreme condition (left: time history of surge, heave and pitch motion respectively; right: spectrum of surge, heave and pitch motion respectively), the JONSWAP spectrum is shown together with the pitch spectrum*

The extreme responses of the semi-submersible platform in surge, heave and pitch are shown in Figure 6.5 together with the JONSWAP spectrum, which is shown in the pitch spectrum. It is clear from these figures that:

- For the surge response, in addition to the wave frequency component, there are also a non-zero mean drift and a low frequency component. It is seen that the wave frequency response is significant from 0.3 rad/s to 0.6 rad/s, which matches the wave spectrum very well. The low frequency response is concentrated around 0.08 rad/s, which is corresponding to surge resonance.

- For the heave response, wave frequency response is dominating. Which means the second order wave effect in heave direction is negligible.

- For the pitch response, there is a clear non-zero mean component, which comes from the constant thrust force plus the second order wave effect. Different from the other two responses where the wave frequency component is significant, the pitch response is concentrated around 0.25 rad/s, which is the pitch natural frequency. However, it is clear from the figure that the pitch resonance frequency is out of the range of the wave spectrum. More analysis will be required before come to a conclusion.

It is seen from Table 6.4 that both surge and pitch motion has a non-zero mean value, while heave does not. All the maximum values are within reasonable range. For the surge motion, the maximum offset multiplied by a safety factor of 1.5 is around 72% of the allowable offset $\Delta x = 46.5m$ as shown by Figure 6.4. This means the stiffness of mooring line is almost just enough if we also taken some material factor into account. Anyway, the total mooring line length could always be increased to increase Δx, vice versa, if needed.

Table 6.4: *Response of the floating wind turbine under extreme condition*

Degree of freedom	Mean value	Maximum value	Unit
Surge	12.8	22.2	m
Heave	0.1	8.3	m
Pitch	6.8	12	deg

6.4.2 Extreme tension (ULS check)

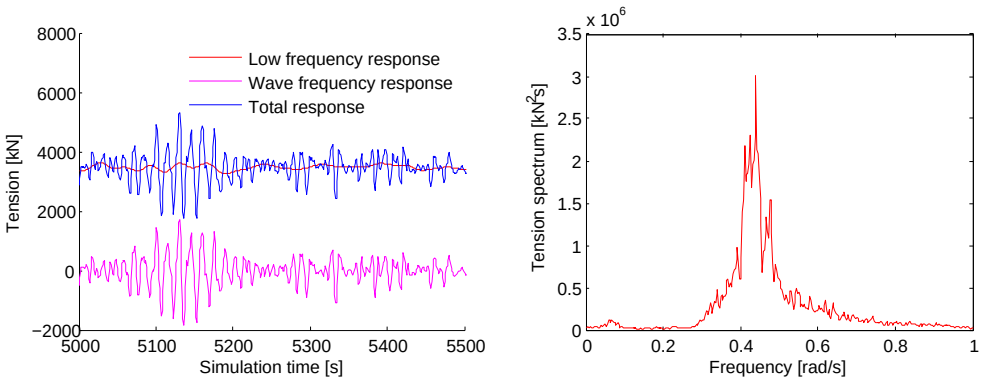

Figure 6.6: *Mooring line tension response of the semi-submersible wind turbine under extreme conditions(left: time history of mooring line tension; right: spectrum of mooring line tension)*

The mooring line tension of one simulation is shown in Figure 6.6. Comparing to the surge response, it is seen that the difference wave frequency contribution to mooring line tension is small. The spectrum is dominated by wave frequency response. This is because under extreme condition the second order wave force (order of 100kN) for this semi-submersible platform is much smaller than the first order wave force (order of 5000kN).

Following DNV-OS-E301 [29], the design for ULS is governed by the utilization factor:

$$u = \frac{T_{C-mean}\gamma_{mean} + T_{C-dyn}\gamma_{dyn}}{S_C} \leq 1 \tag{6.12}$$

where, T_{C-mean} and T_{dyn} are the mean tension and the dynamic tension of the mooring line respectively. γ_{mean} and γ_{dyn} are partial safety factors with $\gamma_{mean} = 1.1$, $\gamma_{dyn} = 1.5$. S_C is the characteristic strength of the mooring line which equals to 0.95 times of the Catalogue breaking strength. Therefore, the main problem is to find T_{C-mean} and T_{dyn}.

T_{C-mean} is found by averaging mean tensions of the 20 simulations. $T_{dyn} = T_{MPM} - T_{C-mean}$, with most probable max (MPM) tension T_{MPM} to be found as the MPM value of the extreme value distribution (Gumbel distribution) for the line tension. Practically, after each simulation, the maximum mooring line tension is stored. Then the 20 maximum values are fitted with Gumbel distribution to find the MPM value, as shown in Figure 6.7.

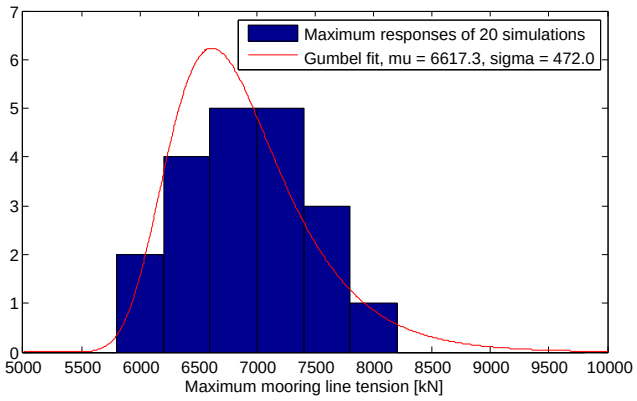

Figure 6.7: *Gumbel fit of the maximum mooring line tension*

The results of ULS check is summarized in Table 6.5. It is seen that the utilization factor is less than 0.5, which means the strength of the mooring line is more than enough. However, as discussed in the previous section, the utilization factor for the mooring line stiffness is relative high. This is not good from an economical point of view. Therefore, if further optimization should be performed, clump weight could be considered to be attached to the mooring lines. Then the use of mooring lines with much smaller nominal diameter is possible to achieve the same stiffness.

Table 6.5: *ULS check of the mooring line tension*

T_{C-mean}	γ_{mean}	T_{dyn}	γ_{dyn}	*total*	S_C	u
(1)	(2)	(3)	(4)	(1)*(2)+(3)*(4)	(5)	total/(5)
3489.9	1.1	3127.4	1.5	8530	1.87E+04	0.46

Chapter 7

Coupled Dynamic Analysis

7.1 The SIMO-RIFLEX-AeroDyn Model

The coupled dynamic analysis is performed by the code SIMO-RIFLEX-AeroDyn (SRA). As shown in Figure 7.1, this coupled tool is developed by Bachynski [52] for the analysis of TLP floating wind turbines. The tool takes advantage of the nonlinear beam element models in RIFLEX, hydrodynamics models in SIMO and aerodynamic models in AeroDyn together with an external controller.

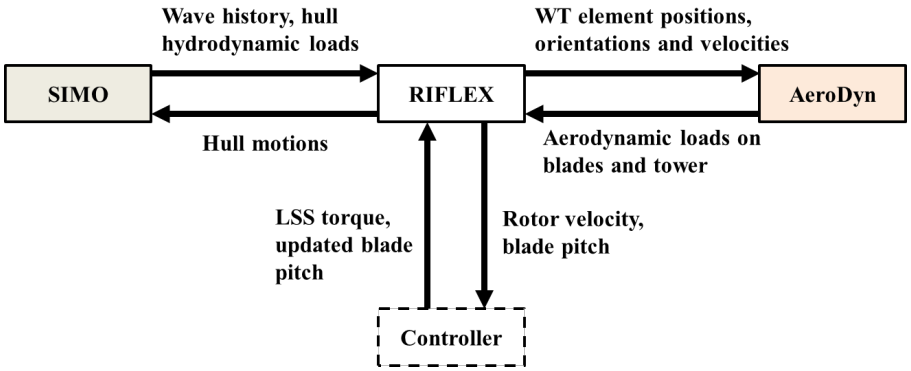

Figure 7.1: *Illustration of the coupling between SIMO, RIFLEX, AeroDyn and the controller(based on Ref [52])*

Following Bachynski [52], an overview of the structural and external load model for a typical semi-submersible floating wind turbine is shown in Figure 7.2.

The hull, hub and nacelle are modelled as rigid bodies. The hull location acts as the master node for the fairleads (pinned) and the bottom of tower (fixed). Hydrodynamic loads are applied to the hull, but no external loads are applied to hub and nacelle.

The mooring lines, tower, shaft and blades are modelled by flexible beam elements. Each mooring line consists of about 45 uniform beam elements with cross sectional property

obtained from the previous mooring system design. Each blade consists of 26 beam elements with cross sections specified with two stiffness axes, which are then rotated according to the twist angle of the blade section. 10 beam elements are used to model the tower. All the properties of the beam cross sections of the blades and tower are based on the DTU 10MW RWT description [66].

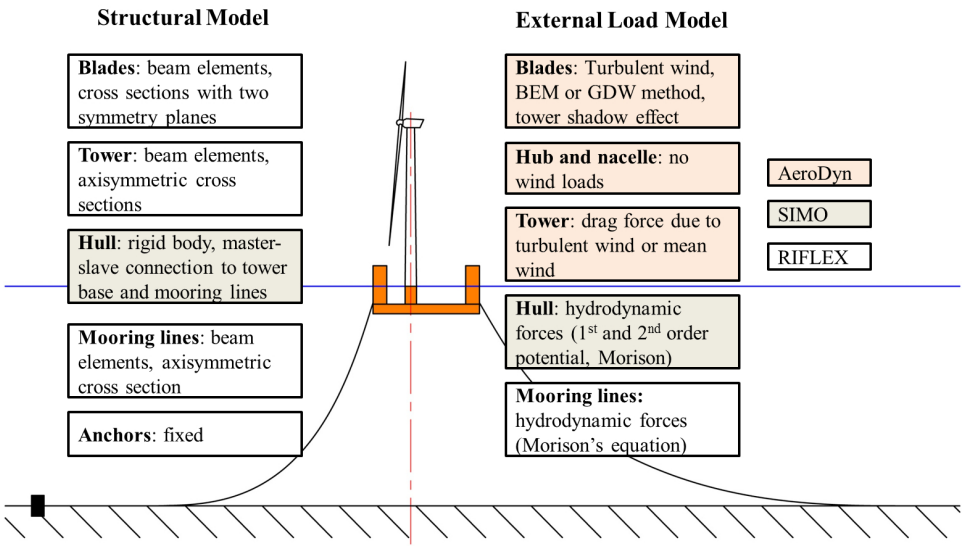

Figure 7.2: *Description of the structural model and external load model of the semi-submersible floating wind turbine (based on Ref [52])*

7.2 Land-Based Wind Turbine Test

Prior to coupled dynamic analysis, several tests have been performed with the land-based DTU 10MW RWT model using the SIMO-RIFLEX-AeroDyn tool to check the modelling.

7.2.1 Constant Wind Test

Two cases of constant wind speed (one set below rated wind speed OP1 and one set above rated wind speed OP3) are tested for the DTU 10MW RWT. Results of rotational speed, blade pitch angle, thrust and generator power time histories are shown in Figure 7.3.

It is seen from the figure that all parameters become steady after about 150s simulation time. It is observed that the thrust curve is oscillating with time. Similar oscillations are found in the time histories of all the other force and displacement curves of blades and tower. This oscillation is introduced by the rotation of the blade and the presence of the tower.

In order to study in details of this oscillation, FFT transformation is applied to the thrust curve. Results are shown in Figure 7.4. It can be found from the transformation that the dominating frequency of the oscillation is 0.341Hz, corresponding to an oscillating period of 2.93s. At the same time, the mean rotational speed of the wind turbine at

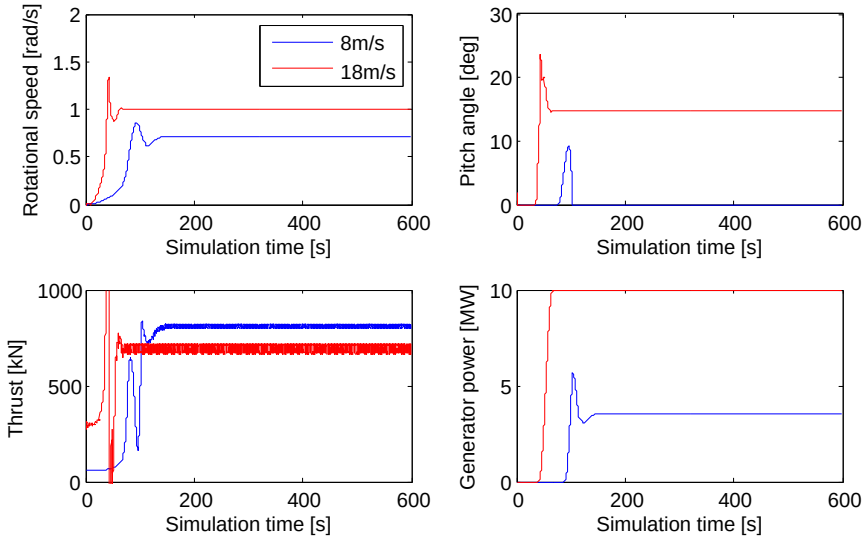

Figure 7.3: *Aerodynamic results of land-based DTU 10MW RWT under constant wind speed*

8m/s is 0.712rad/s as shown in Figure 7.3, equaling to 0.113Hz or 9.82s which is denoted as the 1P frequency of the wind turbine. Then it is clear that the dominated frequency of oscillation of the thrust curve is the 3P frequency. In steady wind condition, this oscillation frequency is caused by the three blades passing by the tower.

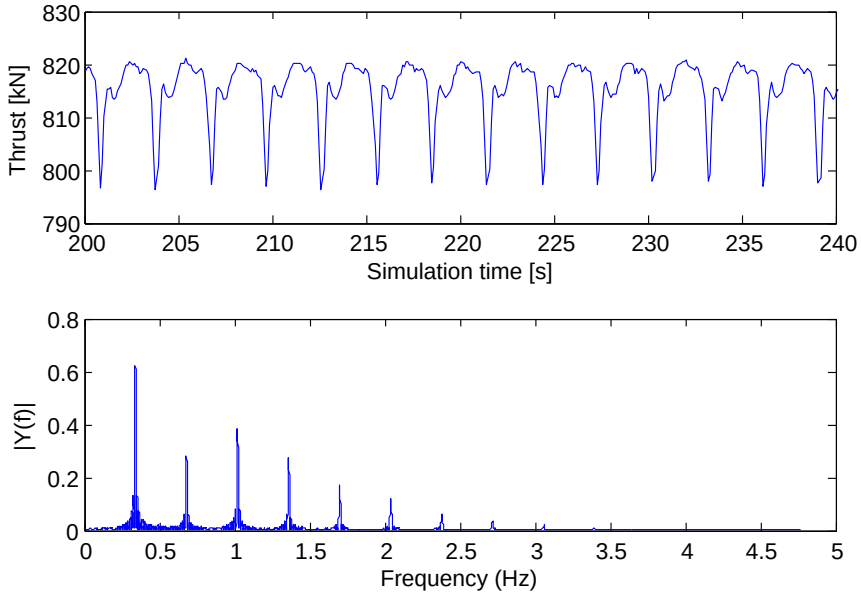

Figure 7.4: *Thrust curve of the land-based DTU 10MW RWT and its FFT transformation, wind speed 8m/s*

7.2.2 Power and Thrust Curve

The thrust and power curve of the DTU 10MW RWT could be obtained by running the constant wind speed test for all the wind speeds from cut-in speed to cut-out speed. Aerodynamic results from the SIMO-RIFELX-AeroDyn are compared to the BEM-based tool HAWCStab2. The power studied here is the generator power, which is 94% of the mechanical power [66].

It is seen from Figure 7.5 that, the comparison shows very good agreement except for some under prediction for thrust at over rated wind speeds. The difference is relative small (up to 8%) comparing to the total thrust. As will be discussed later in Section 7.2.5, the current wind turbine model in SRA is simpler than that in HAWCStab2 due to modeling difficulties, which may be the main reason for the difference.

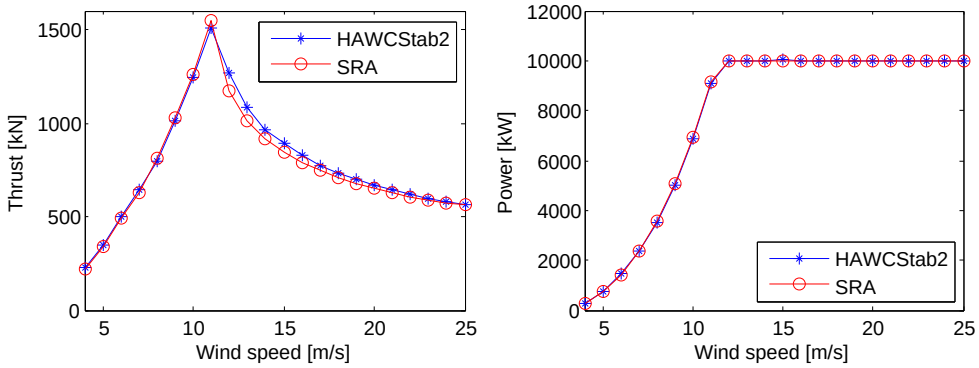

Figure 7.5: *Comparison of thrust and power curves between SIMO-RIFLEX-AeroDyn and HAWCStab2 [66] for the land-based DTU 10MW RWT*

7.2.3 Stepwise Wind Speed Test

A stepwise wind condition is applied to the turbine to test the controller. Results of wind speed, rotational speed of wind turbine, blade pitch angle, generator power are shown in Figure 7.6. These results are very similar to figure 6.1 in the DTU report [66], from which it is confirmed that the controller performs well.

7.2.4 Turbulent Wind Test

Turbulent wind is generated by the TurbSim [78] code and is used as input to AeroDyn. Operational case with mean wind speed of 18m/s (OP3) is considered in this test.

It is seen from Figure 7.7 that the turbulent wind is highly oscillating in time. As expected, there are some oscillation in the curves of blade pitch and rotational speed. It should be noted that that the oscillations of blade pitch angle and rotational speed are much smoother than that of the turbulent wind due to the time delay for the blade pitch controller to act. However, the power outputs for both cases are very smooth and stable, which is a sound evidence of the workability of the controller.

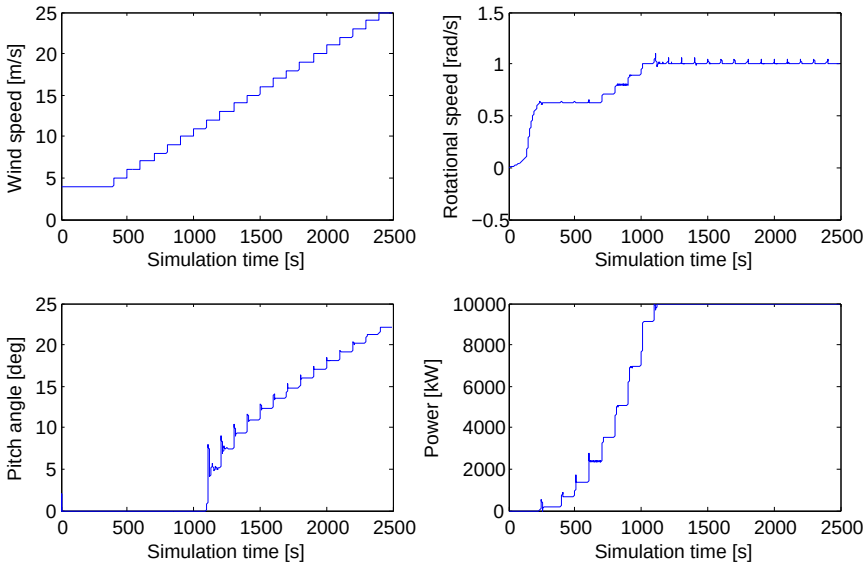

Figure 7.6: *Controller performance at the stepwise wind speed test*

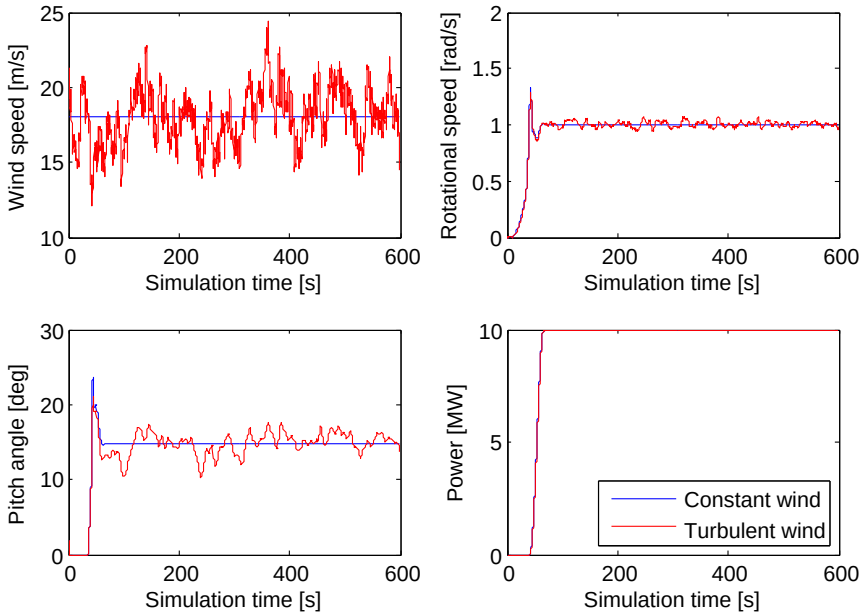

Figure 7.7: *Comparison of land-based DTU turbine under constant and turbulent wind*

7.2.5 Eigenfrequency Test

Eigenfrequency Test of an Isolated Blade

To begin with, eigenfrequency test of an isolated blade of the DTU 10MW RWT is performed. The blade is modelled in RIFLEX as flexible beam members without prebend, cone or tilt and with untwisted structural axis. For the test, the blade is fixed at the blade

root. Results of the first 8 natural frequencies are calculated and compared with those obtained by HAWC2 [66], as shown in Table 7.1.

Table 7.1: *Comparison of natural frequencies of an isolated blade by RIFLEX and HAWC2 (mode is numbered according to HAWC2 results)*

Mode	Description	HAWC2 [Hz]	RIFLEX [Hz]	Relative error [%]
1	1st flap mode	0.61	0.61	1
2	1st edge mode	0.93	0.96	3
3	2nd flap mode	1.74	1.76	1
4	2nd edge mode	2.76	2.9	5
5	3rd flap mode	3.57	3.7	4
6	1st torsion mode	5.69	6.5	14
7	4th flap mode	6.11	6.17	1
8	3rd edge mode	6.66	6.48	3

In general the comparison shows very good agreement with only minor differences towards higher frequency modes. It has to been taken into consideration that there are differences between the beam models used in HAWC2 (Timoshenko [79, 80]) and RIFLEX (Euler-Bernoulli), even if everything else is identical, the HAWC2 eigenfrequencies should in general be lower than the RIFLEX ones.

The difference with the 1st torsion mode is relatively larger than the bending modes. The difference could have to do with the fact that there is an offset between the elastic axes (center of bending for pure moment loading) and shear axis (center of rotation for pure torque loading) for each element of the blade, which is not taken into account in the RIFLEX model. Besides, mass of the blade sections is also eccentric with regard to beam axis, which could be another explanation for the difference.

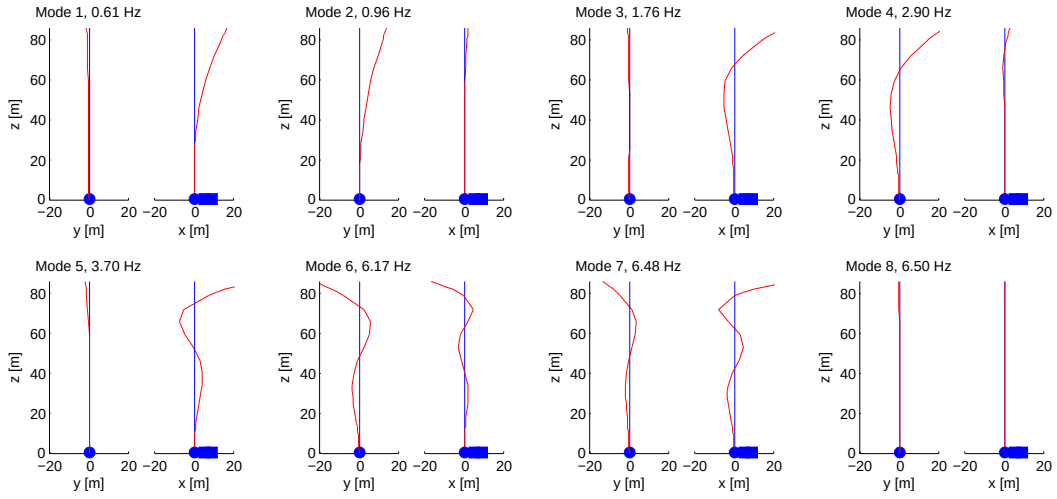

Figure 7.8: *Eigenmodes of an isolated blade (Each mode is illustrated by a front view and a side view. The hub and nacelle are plotted for the purpose of illustration, they are not modeled. The deflection of the blade is multiplied by a factor of 20)*

Figure 7.8 shows the computed eigenmodes of the isolated blade. It is clear that the 1st torsional mode, which is the 6th mode of the HACW2 calculation, is the 8th mode of

the RIFLEX calculation as for the reason stated above. Besides, it is also clear from the figure that the 3rd edgewise mode of the blade is coupled with its 4th flapwise mode.

Eigenfrequency Test of the Whole Turbine

After the eigenfrequency test of an isolated blade, eigenfrequency test for the whole DTU 10MW RWT is also performed in RIFLEX. For this test, prebend, cone and tilt are taken into account in the turbine model. The turbine is fixed at the bottom of tower. Results of the first 13 natural frequencies are shown in Table 7.2, and are also compared with those by HAWC2 [66]. Again, the comparison shows generally good agreement. Differences are also observed, especially for blade bending modes. This is due to the difficulties involved in the modelling of hub, shaft and nacelle.

Figure 7.9 shows the first 3 eigenmodes of the fixed DTU 10MW RWT. Much more work would be needed if one would like to identify and match all the eigenmodes with those from the HAWC2 model. This work is however, beyond the scope of this thesis. If someone is interested, he could refer to Ref [81] to check how the identification of different mode shapes were performed by Risø.

Table 7.2: *Comparison of natural frequency of the land-based DTU 10MW RWT by RIFLEX and HAWC2 (Mode is numbered according to HAWC2 results)*

Mode	Description	HAWC2 [Hz]	RIFLEX [Hz]	Relative error [%]
1	1st Tower Side-to-Side	0.249	0.246	1
2	1st Tower Fore-Aft	0.251	0.247	2
3	1st Drivetrain Torsion	0.502	0.509	1
4	1st Blade Asym. Flapwise Yaw	0.547	0.61	11
5	1st Blade Asym. Flapwise Pitch	0.59	0.614	4
6	1st Blade Collective Flap	0.634	0.739	17
7	1st Blade Asym. Edgewise Pitch	0.922	0.835	9
8	1st Blade Asym. Edgewise Yaw	0.936	0.942	1
9	2nd Blade Asym. Flapwise Yaw	1.376	1.463	6
10	2nd Blade Asym. Flapwise Pitch	1.55	1.638	6
11	2nd Blade Collective Flap	1.763	1.764	0
12	2nd Tower Side-to-Side	1.969	2.045	4
13	2nd Tower Fore-Aft	2.247	2.28	1

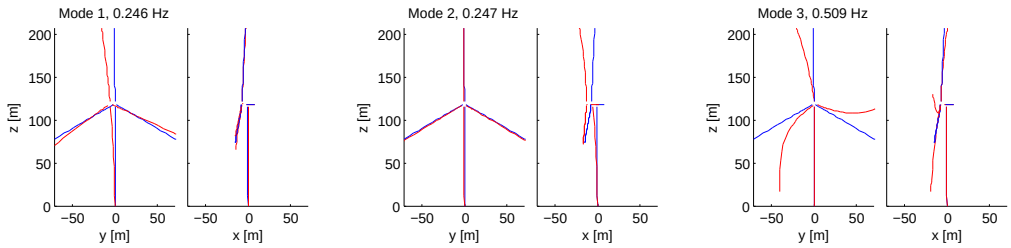

Figure 7.9: *The first 3 eigenmodes of the DTU-10MW-RWT (Displacements are exaggerated by a factor of 150)*

7.3 Floating Wind Turbine Test

In addition to the land-based wind turbine tests, several tests for the floating DTU wind turbine have also been performed.

7.3.1 Constant Wind Test

For the constant wind test, the operational load case (OP3) with constant wind speed of 18m/s is used. The sea state is modelled by JONSWAP spectrum with a peakness factor of 3.3.

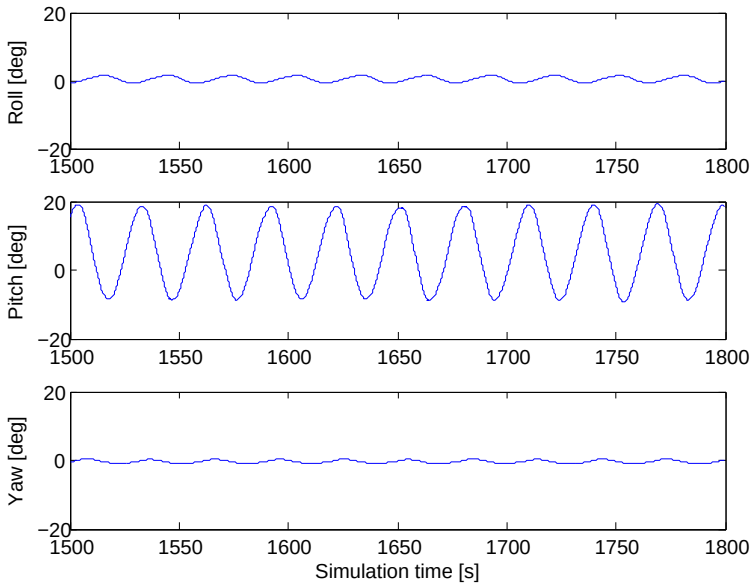

Figure 7.10: *Floating DTU 10MW wind turbine rotations in 4.1m sea with 18m/s constant wind*

Figure 7.10 shows sample time series of rotational motions of the floating wind turbine platform, roll, pitch and yaw over 5 minutes. Due to the symmetric geometry with regard to the wind the wave direction, the motion of roll and yaw is close to zero. A mean pitch of 5° is caused by the aerodynamic loads. However, a pitch oscillation of approximately ±15° around the mean value is observed, which is caused by the blade-pitch controller. This control motion excites the platform at its pitch resonant period around 30s. This is later tuned out by modifying the blade pitch controller coefficients, which is discussed in details in Appendix C.

Figure 7.11 shows the time series of three translational motions of the floating wind turbine. Both heave and sway motions are small, while surge motion is relative large. A mean surge motion of approximately 8m is induced by the aerodynamic loads on the turbine. It is seen that the platform pitch oscillation results in horizontal motion of the platform oscillating at the same period.

Figure 7.12 shows the time series of blade pitch and turbine power output. As discussed above, the motion of blade pitch controller locks into the platform pitch resonance period

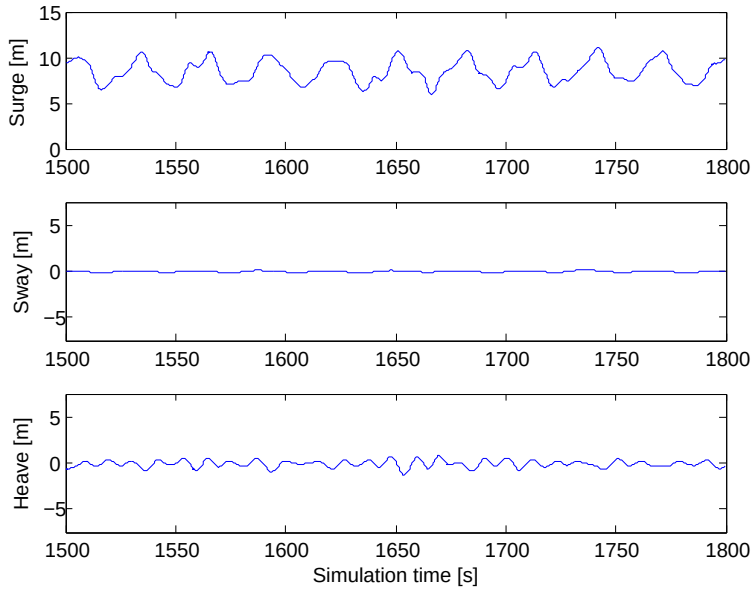

Figure 7.11: *Floating DTU 10MW wind turbine translations in 4.1m sea with 18m/s constant wind*

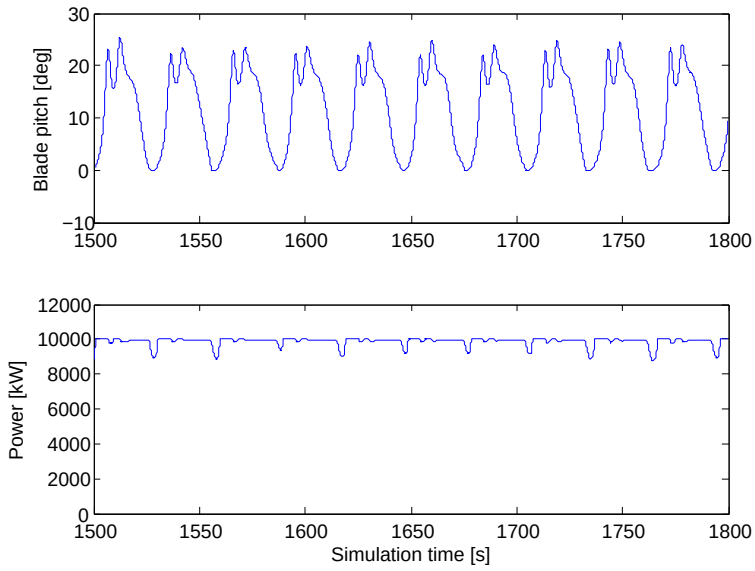

Figure 7.12: *Blade pitch and power output of the floating DTU 10MW wind turbine in 4.1m sea with 18m/s constant wind*

of approximately 30s. However, if we recall previous study on free decay test, the pitch natural period is found to be around 26s, which is smaller than the current value. This issue is discussed in detains in Section 7.3.2.

Back to Figure 7.12, a periodical drop of generator power output occurs when the relative wind speed drops below the rated wind speed due to the motion of platform. However, the influence is very small, the mean power output is still around 9.8MW.

7.3.2 Turbulent Wind Test

The influence of turbulent wind is studied using the load case OP3. The blade pitch controller has been modified according to the methods discussed in Appendix C. Results

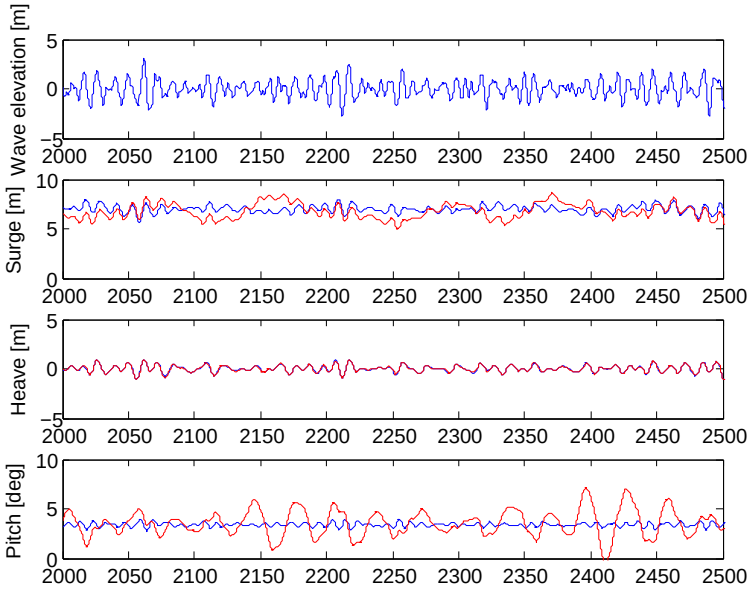

Figure 7.13: *Comparison of time histories of wave elevation (top), platform surge (second), platform heave (third) and platform pitch (bottom) of the Floating DTU 10MW wind turbine under constant (blue line) and turbulent (red line) wind condition*

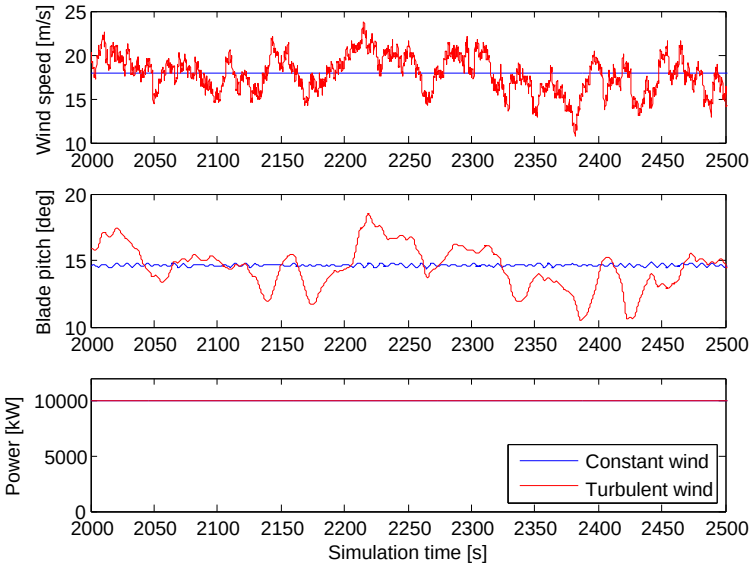

Figure 7.14: *Comparison of time histories of wind speed (top), blade pitch angle (middle) and power output (bottom) of the Floating DTU 10MW wind turbine under constant (blue line) and turbulent (red line) wind condition*

are based on a 1-hour simulation. Time histories of the platform motion responses and wind turbine responses are shown in Figure 7.13 and Figure 7.14 respectively.

From Figure 7.13 it is clear that the turbulent wind will lead to low frequency resonant response of the platform surge and pitch motion, while the heave motion is not affected. This influence will be investigated further in frequency domain later. It is shown by Figure 7.14 that the turbulent wind will cause the blade pitch controller to pitch the blade accordingly. The correlation of the blade pitch angle and the turbulent wind speed is clear. At the meantime, the wind turbine power output is kept at rated power.

Frequency domain investigation

In order to investigate the influence of turbulent wind further, turbine responses are studied in the frequency domain, results are shown in Figure 7.15. The spectra represent the power spectral density, which are obtained by FFT transformation of the time series and are further smoothed by WAFO [86] toolbox.

It is seen that for the surge spectrum the peak at surge resonance frequency increases under turbulent wind, while the part related to wave spectrum is not changed. The same situation is found for the pitch spectrum, where the peak at pitch resonance frequency is dominating the response. It is also clear that the heave response spectrum is not influenced by the turbulent wind, although the heave natural frequency is still within the range of wind spectrum. Possible reason is that in this simulation no wind inclination is considered, which means the wind direction is always horizontal. It will be therefore, difficult for the turbulent wind to excite the vertical heave motion. Similar results has been obtained for other operating load cases, while for parked load case all the response are wave dominated. Please refer to Appendix D for the response of all load cases.

It can therefore be concluded that, under operational conditions, the floating wind turbine surge and pitch resonant motions are excited by turbulent wind and dominating the responses, while heave motion is still wave dominated. Under extreme conditions the influence of turbulent wind is relative small since the blades are pitched to feather, all responses are wave dominated. Besides, for all conditions the mooring line tension response is governed by platform surge motion.

Aerodynamic damping

Recall the discussion in Section 7.3.1, one important thing should be noted from Figure 7.15, namely the pitch resonant frequency is around 0.2rad/s. This value is smaller than the pitch natural frequency from decay test, 0.24rad/s. The same value is observed in load case OP2, while for the extreme load case EX, the blade pitch resonant frequency is found to be back to 0.24rad/s (please refer to Appendix D).

This situation could be explained by the following equation [87]:

$$\omega_{damped} = \omega_n \sqrt{1 - \xi^2} \tag{7.1}$$

where ω_{damped} is the damped natural frequency of a simple 1-dof system and ξ is the damping ratio. Therefore, if the damping ratio is large enough, the resonant frequency will be reduced effectively.

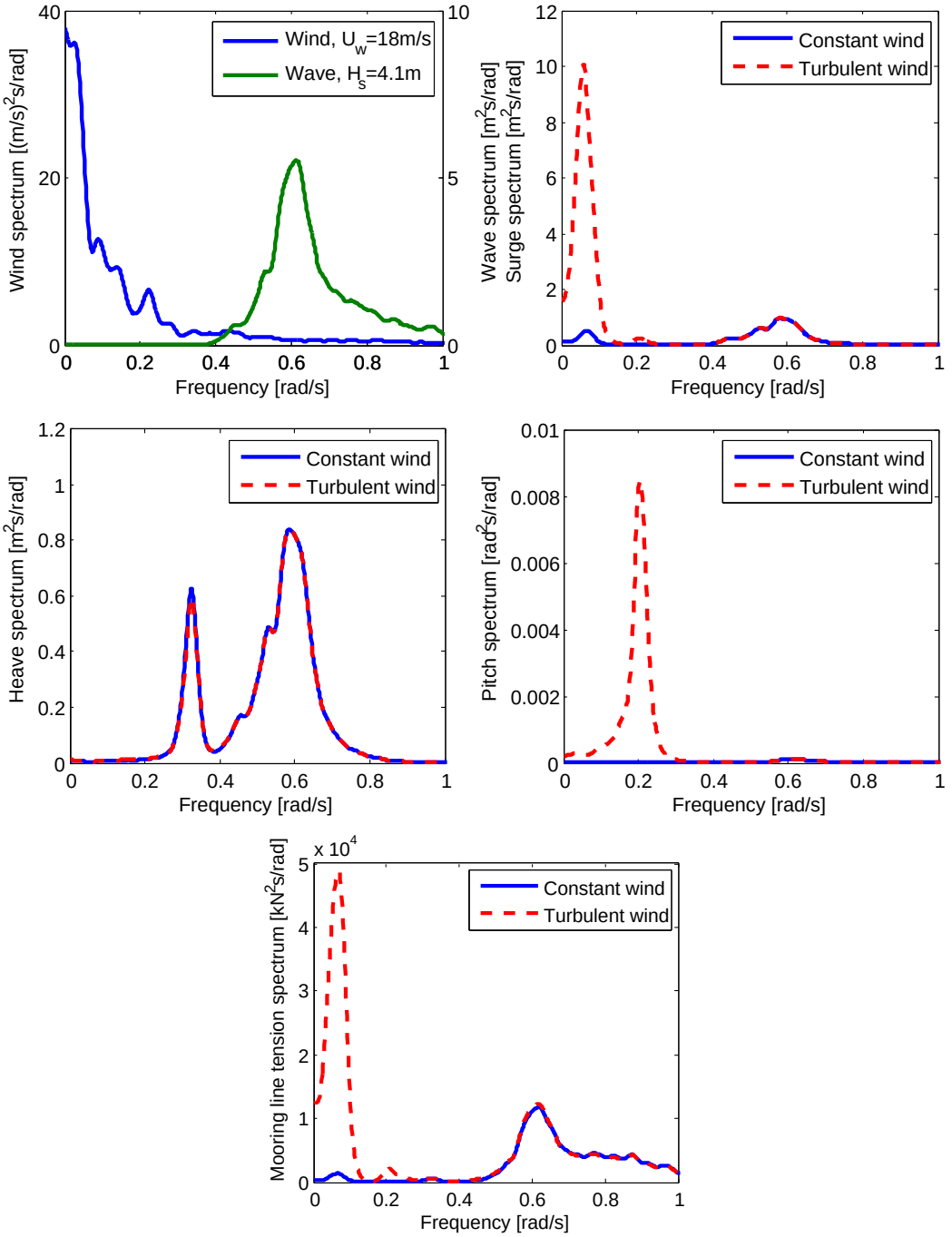

Figure 7.15: *Smoothed turbulent wind and wave spectra (upleft) and smoothed spectra of floating wind turbine responses: surge spectrum (upright), heave spectrum (middleleft), pitch spectrum (middleright) and mooring line fairlead tension spectrum (downleft), response spectra are compared under turbulent and constant wind conditions for load case OP3*

One big difference between the operational condition and the extreme condition is that under extreme condition all blades are pitched to feather resulting in small wind force on the rotor; while under operational condition, there is very large thrust force acting on the rotor. This large thrust force serves as the main source of aerodynamic damping.

A simple form of aerodynamic damping for an operating wind turbine could be derived based on BEM method. Consider a wind turbine blade element with chord length c and distance r to the rotor center. Let the blades rotate at an angular velocity ω under turbulent wind. Then the thrust force per unit length dT/dr could found as [88]:

$$\frac{dT}{dr} = \frac{1}{2}\rho\omega r c \frac{dC_L}{d\alpha}(u - \dot{x}) \tag{7.2}$$

where $dC_L/d\alpha$ is the rate of change of the lift coefficient with angle of attack, u is the change in wind speed and $\dot{x}$ is the structural velocity in the wind direction (blade flapwise motion + tower fore-aft motion + platform pitch and surge motions). Therefore, the aerodynamic damping per unit length of the rotating blade can be estimated as the coefficient related to the structural velocity $\dot{x}$:

$$B_{aero}(r) = \frac{1}{2}\rho\omega r c \frac{dC_L}{d\alpha} \tag{7.3}$$

From Equation (7.3) it is clear that the aerodynamic damping depends on the rotational velocity ω of the blades and will become negligible for a parked wind turbine. Therefore, the reduction in surge resonant frequency could be possibly caused by large aerodynamic damping under operational conditions. However, it should be noted that the evaluation of damping ratio of a floating wind turbine with active controller is still very difficult. More investigation would be needed to study the phenomenon in details.

7.4 Land-Based Versus Floating

In this section the performance of the floating DTU wind turbine is compared to that of the land-based DTU wind turbine to study the differences in performance and responses of the two systems.

7.4.1 Power and Thrust Curve

Site condition with constant wind and no waves are applied to the floating wind turbine system to study the thrust and power output. It should be noted that after the wind speed has reached the rated wind speed, the modified blade pitch controller is applied to the floating wind turbine to avoid the controller induced resonance motion.

As shown in Figure 7.16, in general, the thrust curve and power curve of the floating wind turbine agree well with the results of the land-based wind turbine, except for some small reduction in power output at below rated wind speeds. This means that the motion of the floating platform has limited influence on the aerodynamic performance of the wind turbine. The previous concern about possible reduction of turbine power output due to large motion of the semi-submersible platform during the initial design could be

eliminated. This is because that the blade pitch controller is able change the pitch angle to keep the desired power output during operation.

Therefore, it can be concluded that the floating wind turbine could achieve as good aerodynamic performance as the land-based wind turbine.

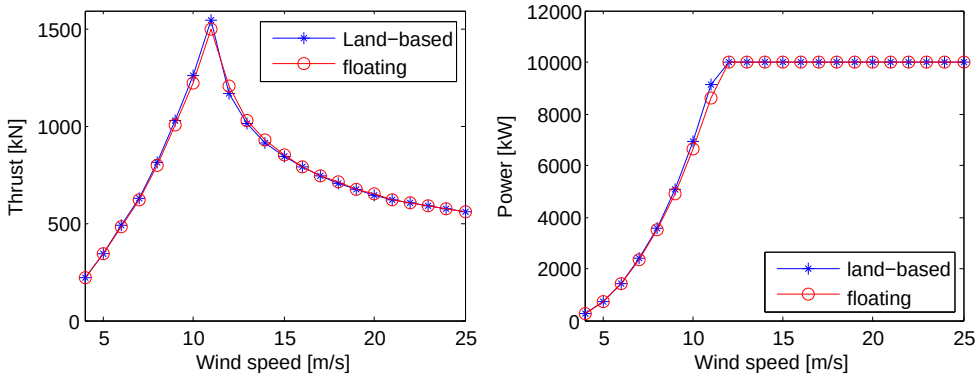

Figure 7.16: *Comparison of thrust and power curve of the land-based and floating DTU wind turbines*

7.4.2 Blade and Tower Response

In order to study further the turbine structural response, load cases listed in Table 3.3 (OP1, OP2, OP3 and EX) with turbulent wind are applied to both land-based and floating wind turbines. Waves are simulated by JONSWAP spectrum with peakness value of 3.3. For each load case, five independent 1-hour simulations are performed. Each of the simulation lasts 4400s with the first 800s excluded from the later data analysis to avoid the transient effect. In the data analysis procedure, the responses of the systems are averaged over the five simulations.

Statistical response characteristics

Figure 7.17 shows the results of blade root out-of-plane bending moment of the floating and the land-based DTU wind turbines under different load cases. Firstly, it is noticed that the moment reaches its largest value at rated wind speed, which is consistent with the thrust curve shown in Figure 7.16. Besides, for the extreme load case, the blade bending moment reduces to about one fifth of the value at rated wind speed, which is caused by the fact that all blades are pitched to feather. In general, it is seen that the blade root bending moment is larger for the floating DTU wind turbine than that of the land-based wind turbine. However, the difference is not big, which is largest at rated wind speed (up to 9%) and becomes negligible for smaller or larger wind speeds.

Figure 7.18 shows the response of tower base fore-aft bending moment under different load cases for the land-based and the floating DTU wind turbines. First of all, it is seen that the tower base bending moment of the floating DTU wind turbine is much larger than that the land-based turbine, and the difference becomes even larger under extreme load condition. While the ratio of mean tower bending moment of the floating wind turbine

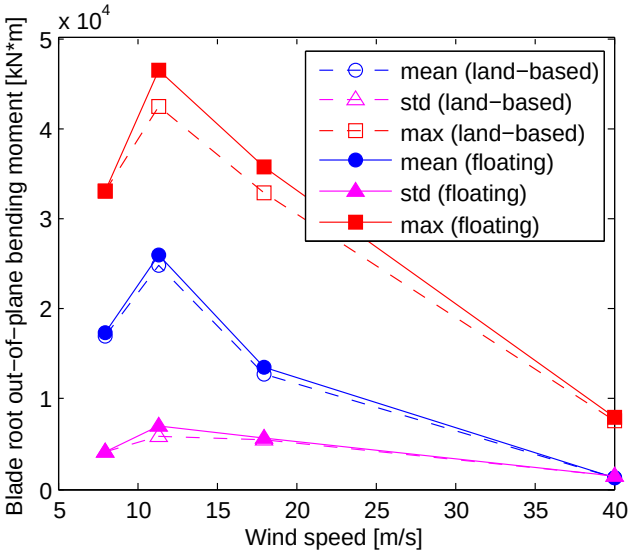

Figure 7.17: *Comparison of blade root out-of-plane bending moment of the land-based and floating DTU wind turbines*

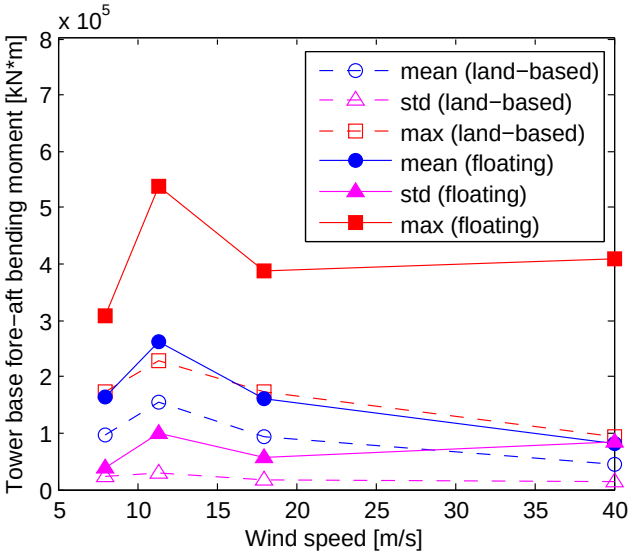

Figure 7.18: *Comparison of tower base fore-aft bending moment of the land-based and floating DTU wind turbines*

to that of the land-based wind turbine keeps around 1.7 over all the load cases, the ratio of standard deviation changes from 1.7 at below rated wind speed to 6.3 under extreme condition and the ratio of maximum value increases from 1.8 at 8m/s to 4.4 at 40m/s wind speed.

However, the figure also shows that based on the present study, the most dangerous condition from the tower response point of view is the condition at rated wind speed not the condition at the 50-year extreme condition. This conclusion is valid for both the land-based and the floating semi-submersible DTU wind turbine based on the present study.

This is different from the results found by Karimirad [89] for the spar-type wind turbine, where he shown that the tower bending moment is highest under survival conditions.

To summarized, motions of the floating wind turbine will lead to larger blade and tower bending moments than those of the land-based wind turbine. Both the blade and the tower have largest responses under operational condition with rated wind speed rather than the extreme condition.

Response spectra

Smoothed response spectra of the blade root out-of-plane bending moment and tower base fore-aft bending moment of the land-based and the floating wind turbines are compared for different load cases. Results under operational condition with rated wind speed and extreme condition are shown in Figure 7.19.

It is seen from Figure 7.19(a) that, for the land-based wind turbine, the blade response is dominated by the wind spectrum with a peak around 1 rad/s which is corresponding to the rated rotational speed 9.6 rpm, namely the 1P frequency of the wind turbine at rated wind speed. For the floating wind turbine, the blade response spectrum has an additional peak at pitch resonant frequency, which is clear when comparing the structural response spectra with the motion response spectra (see Appendix D) of the floating wind turbine. In addition it is seen that for the floating wind turbine blade response spectrum, the peak at 1P frequency is less significant and the response is spread out to a wider range of frequencies. This is because that for a floating wind turbine operating under rated wind speed, in addition to the turbulence of wind, the actual relative wind speed at hub height will also be influenced by the platform motions, which means the wind turbine is actually operating between below rated and above rated wind speeds leading to a change of the rotational (1P) frequency. Similar results have been obtained for the other operational conditions (see Appendix E). The influence of 1P frequency become more significant when the wind speed changes from below rated to above rated. Under extreme condition (Figure 7.19(b)), blades are pitched to feather resulting in small response.

The tower response under operational conditions is similar to that of the blade, but the influence of 1P frequency becomes negligible. Under extreme condition, the platform is characterized by large surge, heave and pitch responses (see Appendix D). The tower response spectrum (Figure 7.19(b)) for frequency below 0.5 rad/s could be seen as a summation of surge, heave and pitch response spectra. Additionally, a large part of the response spectrum locates at frequencies from 0.5 rad/s to 1 rad/s. This part of response is also observed for the load case OP3 (see Appendix D).These frequencies are still within the wave spectrum. More investigations are needed to fully understand the phenomenon.

Therefore, it could be concluded that under operational conditions, the differences in the blade and tower bending moment responses of the land-based and the floating wind turbines are mainly due to the platform pitch motion. Additional influence of 1P frequency is found in blade moment response. Under extreme conditions, there is no big difference in the blade moment response, while the tower moment response for the floating wind turbine has additional contributions from platform surge, heave and pitch motions and another wave frequency part which is not fully explained.

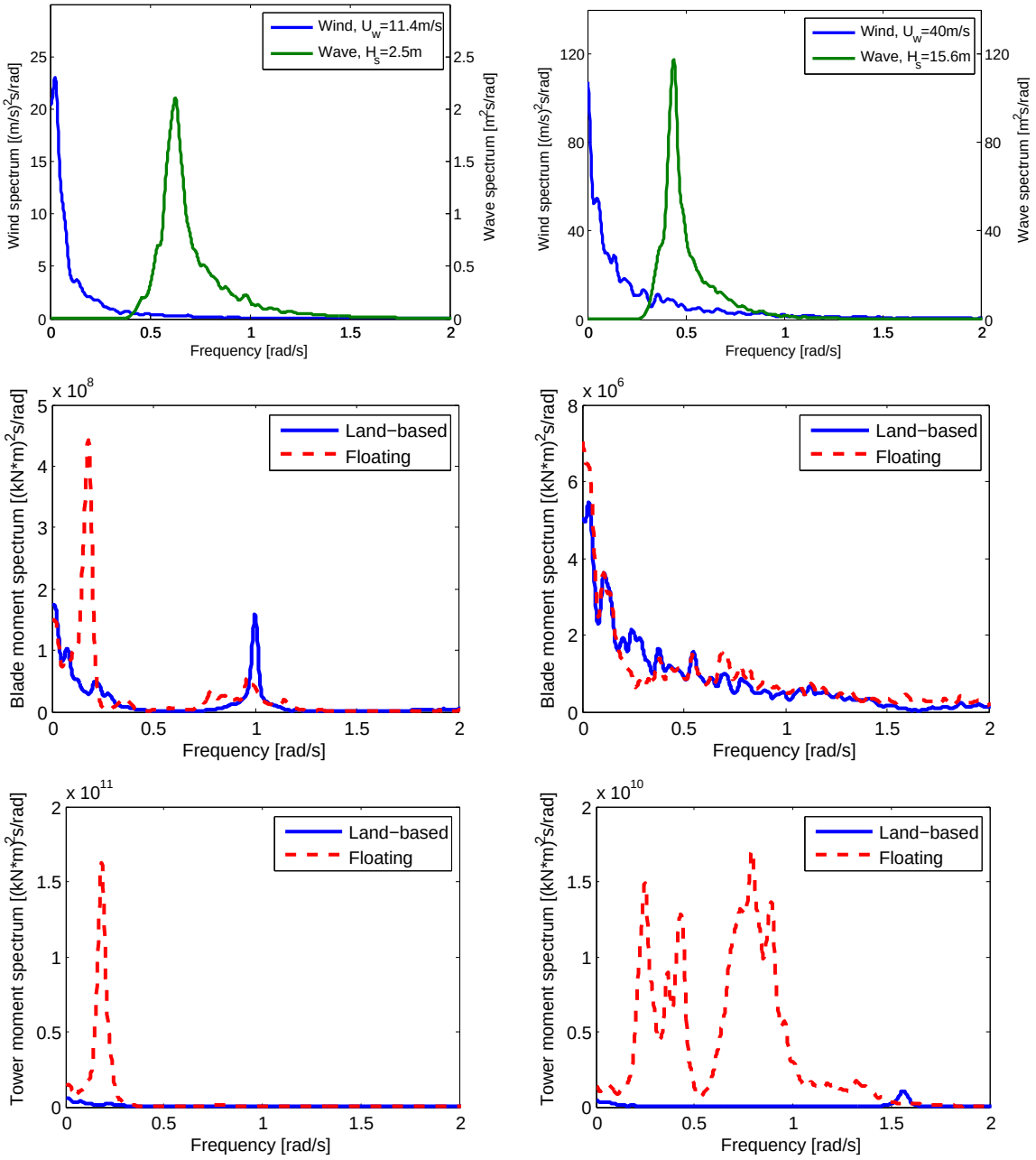

(a) Response spectra for load case OP2 (b) Response spectra for load case EX

Figure 7.19: *Comparison of land-based and floating wind turbine blade root out-of-plane bending moment and tower base fore-aft bending moment response spectra for load case OP2(a) and EX(b)*

7.5 Characteristics of Semi-submersible Wind Turbine

7.5.1 Statistical Response Characteristics

The responses of the semi-submersible floating wind turbine and its mooring line system under different load cases are studied by the same method as described in Section 7.4.2. The statistical results of the responses are averaged over the five simulations which are shown in Figure 7.20.

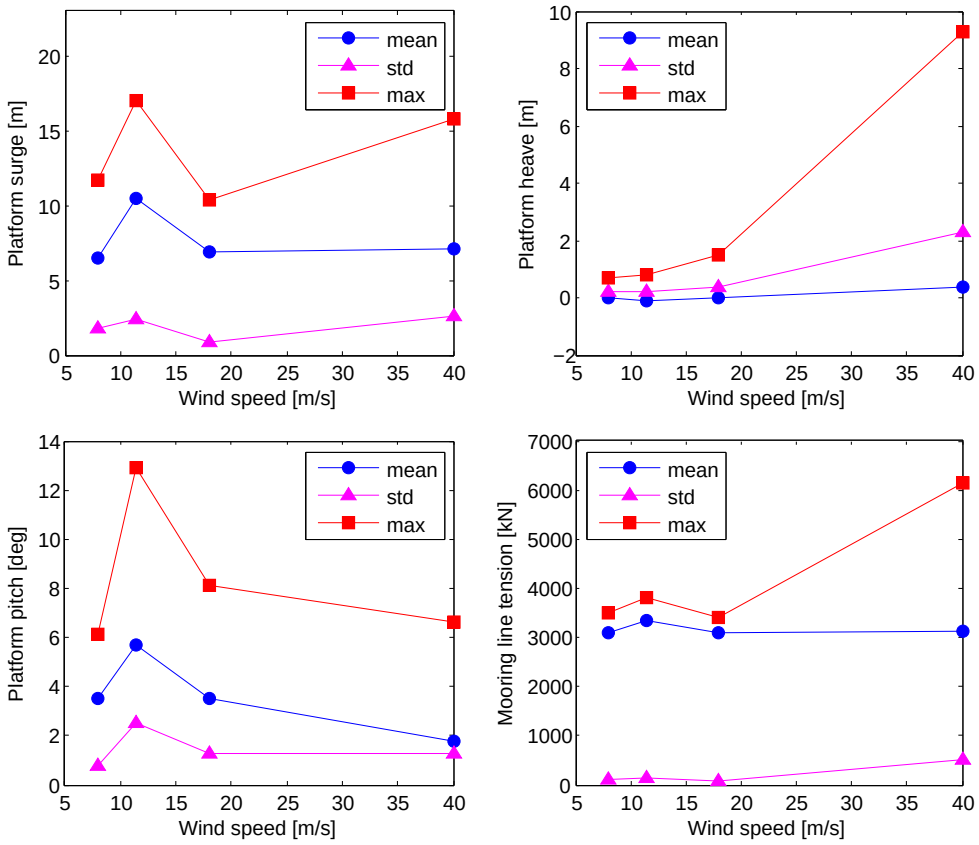

Figure 7.20: *Statistical results of platform surge (upleft), heave (upright), pitch (downleft) and mooring line tension at fairlead (downright) under different load cases*

First of all, all responses except the heave motion have non-zero mean values due to mean wind and wave drift loads. At rated wind speed, the platform response is characterized by large surge and pitch motions, while heave motion and mooring line tension stay almost unaffected.

It can also be seen that the mean values of all responses stay almost unchanged from load case OP3 (18m/s wind speed) to EX (40m/s wind speed), except for the mean pitch motion, which decreases due to the reduced thrust force. At the meantime, the maximum values and standard deviations of pitch, heave and mooring line tension increase sharply, especially for the maximum heave motion and mooring line tension. In a word, the responses of the floating wind turbine system under extreme conditions are characterized by large surge, heave motions and large mooring line tension oscillations but decreased

pitch motion. The increased heave motion may be caused by the fact that under extreme condition, the peak wave frequency is much closer to the heave natural frequency than any other load cases (please refer to Appendix D), which means more wave energy at heave natural frequency leading to lager response.

To conclude, operational condition with rated wind speed is the most important condition for platform pitch motion, while extreme condition is the most important condition for the study of platform heave motion and mooring line tension. Both are important for platform surge motion.

7.5.2 Influence of Second Order Wave Loads

In order to investigate the influence of second order wave loads on the floating wind turbine response, 1-h simulations of load case OP3 are performed with different hydrodynamic models:

- Linear: 1st order wave loads only;
- Newman's approximation: 1st order wave loads, 2nd order wave loads by Newman's approximation;
- Full QTF: 1st order wave loads, 2nd order wave loads by full difference quadratic transfer functions.

In all the three wave models, viscous force is included by Morison elements as before.

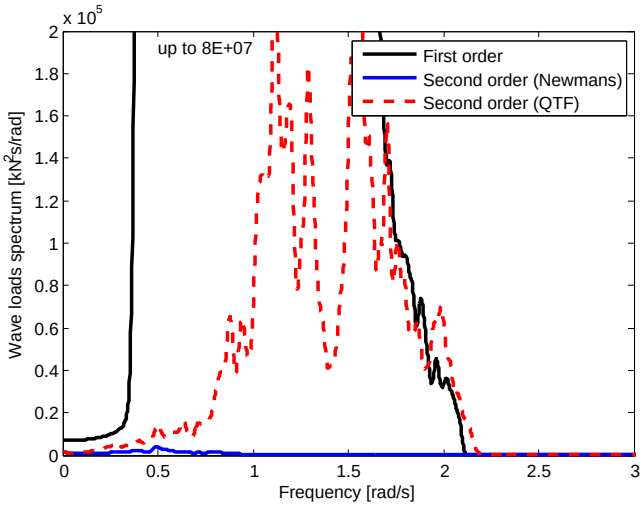

Figure 7.21: *First and second order wave surge excitation forces for load case OP3 (Hs=4.1m and Tp=10.5s)*

The first and second order wave excitation forces are compared in Figure 7.21 and Table 7.3. It is clear that the second order force from full QTF is larger than that obtained through Newman's approximation, but both of them are very small comparing to the first order wave excitation force. Consequently, the influence of second order wave force on the

Table 7.3: *Statistical characteristics of surge excitation forces for load case OP3 (Hs=4.1m and Tp=10.5s)*

Surge force(kN)	Mean	Std
First order	0.8	3860
Second order (Newman)	23.5	41
Second order (QTF)	23.8	360

mooring line tension is negligible as shown in Figure 7.22. However, the second order force is able to excite surge, heave and pitch resonant motions. The surge resonant frequency at 0.07 rad/s, heave resonant frequency at 0.32 rad/s and pitch resonant frequency at 0.25 rad/s are clear from Figure 7.22. In all the responses, the wave frequency part is not affected by the introducing of second order wave force while the resonant responses are affected.

The difference by using different second order wave force models is small for surge and mooring line tension response. The difference is more significant for heave and pitch response around their natural frequencies.

However, the reader should be reminded of the previous discussion on turbulent wind. Under turbulent wind condition (which is more real situation for a floating wind turbine), the responses of platform surge and pitch motions as well as the mooring line tension are governed by the wind force (see Appendix D). Therefore, although the second order wave force has some influence on the responses of surge, pitch and mooring line tension, such influence will become negligible when turbulent wind is considered. However, as discussed previously, the heave motion is not affected by wind force; and as has been pointed out in the previous section, heave response will be important under extreme condition. Therefore it is important to introduce second order wave forces to the system when one want to study the heave response under extreme conditions in details.

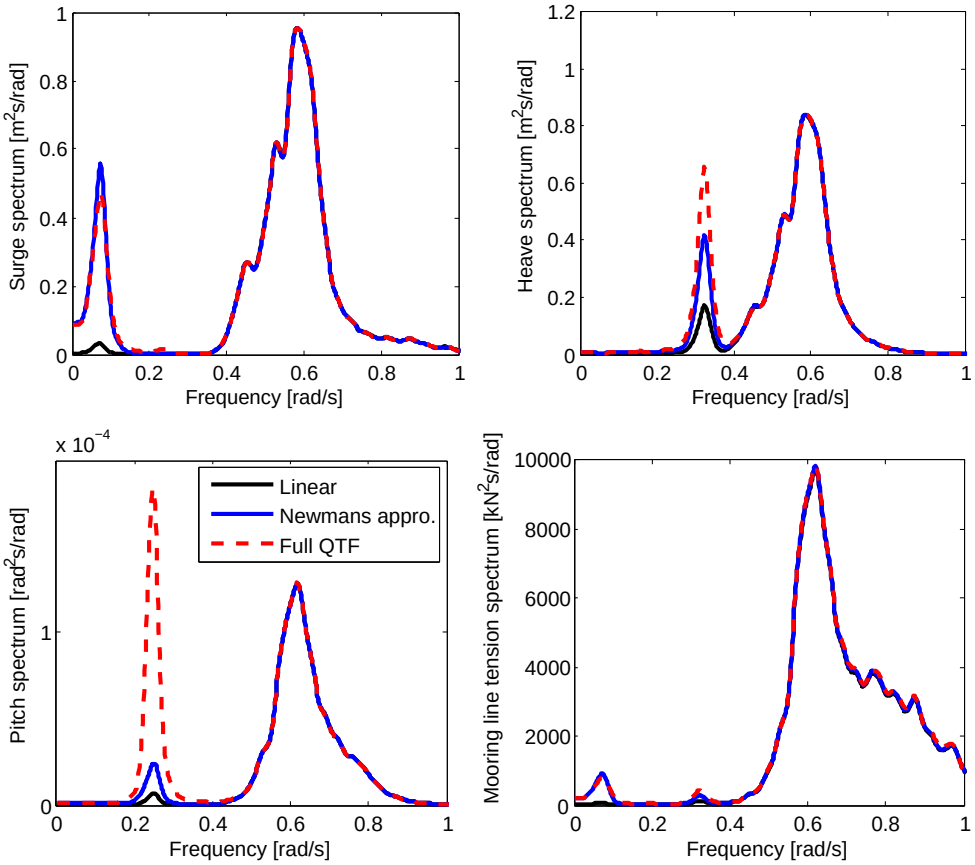

Figure 7.22: *Smoothed spectra of surge, heave, pitch motion and mooring line fairlead tension by different hydrodynamic models under load case OP3 (Hs=4.1m, Tp=10.5s)*

Chapter 8

Conclusion and Recommendation

8.1 Conclusion

An initial design of a pontoon-type semi-submersible platform supporting the 10MW DTU RWT has been successfully performed including a spread catenary mooring system. The hydrodynamic behaviors of the semi-submersible platform are studied in details with implementation of second order wave loads. Finally coupled hydro-aero-servo-elastic dynamic analysis by SIMO-RIFLEX-AeroDyn is performed for the whole system. It can be concluded from the thesis that it's theoretically feasible to use a semi-submersible platform to support the DTU 10MW RWT.

A summary of the properties of the semi-submersible platform and its mooring system are provided from Table 8.1 to Table 8.3.

Table 8.1: *Property of the semi-submersible floating wind turbine*

Property	Value	Unit
Rated power	10	MW
Hub height	119	m
Side column diameter	10	m
Center column diameter	8.3	m
Pontoon length	45	m
Pontoon height	7	m
Operation draft	20	m
Free board	15	m
Turbine mass	1305	t
Semi mass	2588	t
Displacement	13955	t
Vertical center of gravity	-5.7	m
Vertical center of buoyancy	-13.8	m

Table 8.2: *Property of the mooring system*

Property	Value	Unit
Number of mooring lines	3	[-]
Water depth	200	m
Fairlead elevation	-15	m
Unstretched mooring line length	880	m
Pretension	2190	kN
Chain nominal diameter	153	mm
Mooring line unit mass in water	0.447	t/m
Mooring line axial stiffness	2.10E+06	kN

Table 8.3: *Natural frequencies of the semi-submersible floating wind turbine*

Degree of freedom	Natural frequency [rad/s]
Surge/Sway	0.07
Heave	0.31
Roll/Pitch	0.24
Yaw	0.1

More detailed conclusions from analysis are divided into two parts, first part includes conclusions from Chapter 4, while the second part includes conclusions from the rest of the thesis, Chapter 5 to 7.

Conclusions from initial design analysis in Chapter 4:

1. Viscous damping is important for the semi-submersible platform at resonance, linearization of drag force serves as a possible method to deal with it in frequency domain.

2. Cancellation effect of the semi-submersible platform in heave RAO is predicted both numerically and analytically. It is also proved analytically that there is no cancellation effect in the heave motion when viscous damping is included.

3. Cancellation effect at small wave period of the sectional loads takes place when the characteristic length of the semi-submersible platform is equal to several full wave lengths.

4. The stability behavior and heave motion is not dependent on wave direction, while the pitch motion is related to the platform projected width on the direction normal to wave direction. The static heeling angle is most sensitive to pontoon length, while the heave natural period is most sensitive to side column diameter.

Conclusions from further analysis in Chapter 5-7:

1. Similar cancellation effect is observed for the mean drift loads in surge of the platform as that of the sectional loads.

2. The mean drift loads by direct pressure integration is not affected by the size of free surface domain or pontoon mesh size, but is most sensitive to the column mesh size at free surface. Fine mesh at the columns close to water surface is required to achieve accuracy.

3. The controller in the SRA code has a good performance for the land-based DTU wind turbine. For floating wind turbine at above rated wind speed, the blade pitch controller will excited the pitch resonant motion of the platform, which could be solved by reducing the PI gains of the controller.

4. Motions of the floating platform has limited influence on the aerodynamic performance of the wind turbine, but will lead to larger blade and tower bending responses (mainly due to the platform pitch motion). Both blade and tower have the largest structural responses under operational condition with rated wind speed rather than the extreme condition.

5. For the floating wind turbine, operational condition with rated wind speed is the most important condition for platform pitch motion, while extreme condition is most important condition for platform heave and mooring line tension responses. Both are important for platform surge motion.

6. Turbulent wind is able to excite floating wind turbine surge and pitch resonant motions under operational conditions, which will dominate the response, while heave motion remains wave dominated. Under extreme conditions the influence of turbulent wind is relative small, all responses are wave dominated.

7. The second order wave force has no influence on the wave frequency part of all responses, but will influence the surge, heave and pitch resonant responses. However, this influence is negligible under turbulent wind conditions. Second order wave force and the use of different second order wave models could be important for the study of heave motion under extreme conditions.

8.2 Recommendation

Due to limited time, several phenomena have not been fully discussed or studied. In addition, some assumptions have been made during the study. Therefore, some recommendations are made from this study:

1. More work is needed to justify that the static heeling angle and heave natural period obtained in this study is sufficient. Otherwise, the design should be modified to achieve better behavior.
2. The tower used in this design is initially designed for land-based wind turbine, more appropriate hub height and tower property should be used for the floating wind turbine.
3. More advance mesh generation tool should be used to get better mesh for the QTF calculation.
4. Clump weight could be used to balance the strength and stiffness of mooring lines.
5. The wind turbine model in SRA could be improved by introducing more accurate modelling of the blade, nacelle, hub and shaft.
6. The controller in SRA could be improved by implement the wind speed measurement from the RIFLEX output file and use a low pass filter to set the minimum blade pitch of the controller.
7. More load cases or different sites should be investigated to fully understand the behavior of the floating wind turbine, such as wind shear, wind-wave misalignment and fault conditions.
8. Aerodynamic damping in a floating wind turbine system could be studied in details.
9. Model test or code-to-code comparison are recommended to verify the results.
10. Other issues such as fabrication and transportation, cost estimation could be studied.

References

[1] Rebecca J. Barthelmie and Sara Pryor. A review of the economics of offshore wind farms. *Wind engineering*, 25(4):203–213, 2001.

[2] Andrew R. Henderson, Colin Morgan, Bernie Smith, Hans C. Sørensen, Rebecca J. Barthelmie, and Bart Boesmans. Offshore Wind Energy in EuropeA Review of the StateoftheArt. *Wind Energy*, 6(1):35–52, 2003.

[3] EWEA. *Deep Water - The Next Step for Offshore Wind Energy*. The European Wind Energy Association, 2013.

[4] Arapogianni Athanasia and Anne Benedicte Genachte. Deep Offshore and New Foundation Concepts. *Energy Procedia*, 35(0):198–209, 2013. doi: http://dx.doi.org/10.1016/j.egypro.2013.07.173. URL http://www.sciencedirect.com/science/article/pii/S1876610213012599.

[5] K. Lynch, J. Murphy, L. Serri, and D. Airoldi. Site Selection Methodology for Combined Wind and Ocean Energy Technologies In Europe. In *4th International Conference on Ocean Energy*, Dublin, Ireland, 2012.

[6] UMassAmherst. Early Offshore Wind Research. URL http://www.umass.edu/windenergy/about.history.earlyresearch.php.

[7] Statoil. Hywind the worlds first full-scale floating wind turbine. URL http://www.statoil.com/en/technologyinnovation/newenergy/renewablepowerproduction/offshore/hywind/pages/hywindputtingwindpowertothetest.aspx.

[8] Principle. WindFloat. URL http://www.principlepowerinc.com/products/windfloat.html.

[9] Takeshi Ishihara. *Fukushima Floating Offshore Wind FarmDemonstration Project (Fukushima FORWARD)*. Fukushima Offshore Wind Consortium, 2013.

[10] Floating Offshore Wind Foundations: Industry Consortia and Projects in the United States, Europe and Japan. An Overview. Technical report, 2013.

[11] Dominique Roddier, Antoine Peiffer, Alexia Aubault, and Joshua Weinstein. A Generic 5 Mw Windfloat for Numerical Tool Validation & Comparison Against a Generic Spar. In *ASME 2011 30th International Conference on Ocean, Offshore and Arctic Engineering OMAE 2011*, Rotterdam, The Netherlands, 2011.

[12] *DNV-OS-J103. Design of Floating Wind Turbine Structures.* Det Norsk Veritas, 2013.

[13] Dominique Roddier, Christian Cermelli, Alexia Aubault, and Alla Weinstein. WindFloat: A floating foundation for offshore wind turbines. *Journal of Renewable and Sustainable Energy*, 2(3):33104, 2010. doi: 10.1063/1.3435339.

[14] Alexia Aubault, Christian Cermelli, and Dominique Roddier. WindFloat: A Floating Foundation for Offshore Wind TurbinesPart III: Structural Analysis. In *ASME 2009 28th International Conference on Ocean, Offshore and Arctic Engineering*, pages 213–220. American Society of Mechanical Engineers, 2009.

[15] Christian Cermelli, Dominique Roddier, and Alexia Aubault. WindFloat: A floating foundation for offshore wind turbinesPart II: hydrodynamics analysis. In *ASME 2009 28th International Conference on Ocean, Offshore and Arctic Engineering*, pages 135–143. American Society of Mechanical Engineers, 2009.

[16] Dominique Roddier, Christian Cermelli, and Alla Weinstein. WindFloat: A Floating Foundation for Offshore Wind TurbinesPart I: Design Basis and Qualification Process. In *ASME 2009 28th International Conference on Ocean, Offshore and Arctic Engineering*, pages 845–853, 2009.

[17] J. Jonkman, S. Butterfield, W. Musial, and G. Scott. Definition of a 5-MW Reference Wind Turbine for Offshore System Development. Technical Report NREL/TP-500-38060, National Renewable Energy Laboratory, 2009.

[18] A. Robertson, J. Jonkman, M. Masciola, H. Song, A. Goupee, A. Coulling, and C. Luan. Definition of the Semisubmersible Floating System for Phase II of OC4. *NREL, Golden, CO*, 2012.

[19] Andrew Joseph Goupee, Bonjun Koo, Kostas Lambrakos, and Richard Kimball. Model tests for three floating wind turbine concepts. In *Offshore Technology Conference*. Offshore Technology Conference, 2012. ISBN 1613992009.

[20] Alexander J. Coulling, Andrew J. Goupee, Amy N. Robertson, and Jason M. Jonkman. Importance of Second-Order Difference-Frequency Wave-Diffraction Forces in the Validation of a FAST Semi-Submersible Floating Wind Turbine Model. In *ASME 2013 32nd International Conference on Ocean, Offshore and Arctic Engineering*, pages V008T09A019–V008T09A019. American Society of Mechanical Engineers, 2013.

[21] Lin Li, Zhen Gao, and Torgeir Moan. Joint Environmental Data at Five European Offshroe Sites for Design of Combined Wind and Wave Energy Devices. In *32nd International Conference on Ocean, Offshore and Arctic Engineering, OMAE2013*, Nantes, France, 2013.

[22] Hyunkyoung Shin, Byungcheol Kim, Pham Thanh Dam, and Kwangjin Jung. Motion of OC4 5MW Semi-Submersible Offshore Wind Turbine in Irregular Waves. In *ASME 2013 32nd International Conference on Ocean, Offshore and Arctic Engineering*, pages V008T09A028–V008T09A028, 2013.

[23] T. Moan, S. Berge, and K. Holthe. Analysis of the Fatigue Failure of Alexander L. Kielland. In *ASME Winter Journal Meeting, Washington, D. C*, 1981.

[24] Wikipedia. Alexander L. Kielland (platform). URL http://en.wikipedia.org/wiki/Alexander_L._Kielland_(platform).

[25] Odd Faltinsen. *Sea loads on ships and offshore structures*. Cambridge university press, 1993. ISBN 0521458706.

[26] Johan M. J. Journée and W. W. Massie. Offshore Hydrodynamics. *Delft University of Technology*, 2001.

[27] Walt Musial, Sandy Butterfield, and Andrew Boone. Feasibility of floating platform systems for wind turbines. In *A Collection of the 2004 ASME Wind Energy Symposium Technical Papers Presented at the 42nd AIAA Aerospace Sciences Meeting and Exhibit, 57 January 2004, Reno Nevada, USA*, pages 476–486, 2004.

[28] Z. Gao and T. Moan. Mooring system analysis of multiple wave energy converters in a farm configuration. In *Proc. of the 8th European Wave and Tidal Energy Conference (EWTEC), Uppsala, Sweden*, 2009.

[29] *DNV-OS-E301. Position Mooring*. Det Norsk Veritas, 2013.

[30] *API RP 2SK. Recommended Practice for Design and Analysis of Stationkeeping Systems for Floating Structures*. American Petroleum Institute, 2005.

[31] N. D. P. Barltrop. *Floating structures: a guide for design and analysis*, volume 2. CMPT, Aberdeen, 1998. ISBN 1-870553-35-7.

[32] Petrowiki. MODU riser and mooring systems. URL http://petrowiki.org/MODU_riser_and_mooring_systems.

[33] C. López-Pavón, R. A. Watai, F. Ruggeri, A. N. Simos, and A Souto-Iglesias. Influence of wave induced second-order forces in semisubmersible FOWT mooring design. volume 8, 2013. URL http://www.scopus.com/inward/record.url?eid=2-s2.0-84893064201&partnerID=40&md5=1dfbcbb1c06b16d1c3cf7368cec78877.

[34] Marco Masciola, Amy Robertson, Jason Jonkman, Alexander Coulling, and Andrew Goupee. Assessment of the importance of mooring dynamics on the global response of the deepcwind floating semisubmersible offshore wind turbine. In *Proc. 23rd International Offshore and Polar Engineering Conference*, 2013.

[35] Madjid Karimirad and Torgeir Moan. Wave and Wind Induced Motion Response of Catenary Moored Spar Wind Turbine. In *Computational Methods in Marine Engineering Conference*, Trondheim, Norway, 2009. International Center for Numericcal Methods in Engineering (CIMNE), Barcelona, Spain.

[36] E. N. Wayman, P. D. Sclavounos, S. Butterfield, J. Jonkman, and W. Musial. Coupled Dynamic Modelling of Floating Wind Turbine System, 2006.

[37] Madjid Karimirad. *Stochastic Dynamic Response Analysis of Spar-Type Wind Turbine with Catenary or Taut Mooring Systems*. PhD thesis, Norwegian University of Science and Technology, Trondheim, Norway, 2011.

[38] A. Cordle and J. Jonkman. State of The Art in Floating Wind Turbine Design Tools. In *21st International Offshore and Polar Engineering Conference*, Maui, Hawaii, 2011.

[39] J. Jonkman and W. Musial. Offshore code comparison collaboration (OC3) for IEA task 23 offshore wind technology and deployment. *Contract*, 303:275–3000, 2010.

[40] A. Robertson, J. Jonkman, W. Musial, F. Vorpahl, and W. Popko. Offshore Code Comparison Collaboration, Continuation: Phase II Results of a Floating Semisubmersible Wind System. 2013.

[41] Jason M. Jonkman and Marshall L. Buhl. FAST User's Guide. Technical report, National Renewable Energy Laboratory, 2005.

[42] J. M. Jonkman. Dynamics Modeling and Loads Analysis of an Offshore Floating Wind Turbine. Technical report, National Renewable Energy Laboratory, 2007.

[43] David J. Laino. AeroDyn User's Guide, Version 12.50. Technical report, National Renewable Energy Laboratory, 2002.

[44] *WAMIT User Manual, Version 7.0*. WAMIT Inc., 2013.

[45] J. M. Jonkman and D. Matha. Dynamics of offshore floating wind turbinesanalysis of three concepts. *Wind Energy*, 14(4):557–569, 2011.

[46] K. J. Hao, A. N. Robertson, J. Jonkman, F. Driscoll, and E. Y. K. Ng. Building and calibration of a fast model of the SWAY prototype floating wind turbine. pages 788–793, 2013. URL http://www.scopus.com/inward/record.url?eid=2-s2.0-84899089186&partnerID=40&md5=6fcf5867261553eb05e9be4a820f2023.

[47] S. Shim and M. H. Kim. Rotor-Floater-Tether Coupled Dynamic Analysis Of Offshore Floating Wind Turbines. In *International Offshroe and Polar Engineering Conference (ISOPE)*, pages 455–460, Vancouver, Canada, 2008.

[48] Torben J. Larsen and Anders Melchior Hansen. *How 2 HAWC2, the user's manual*. RisøNational Laboratory, 2007. ISBN 8755035833.

[49] Z. Jiang, M. Karimirad, and T. Moan. Dynamic response analysis of wind turbines under blade pitch system fault, grid loss, and shutdown events. *Wind Energy*, 2013. URL http://www.scopus.com/inward/record.url?eid=2-s2.0-84878817772&partnerID=40&md5=f0ec41fb00a24fb03618d6b585562714.

[50] MARINTEK. *SIMO User Manual Version 4.0 rev 0*. Norwegian Marine Technology Research Insitute, Trondheim, Norway, 2012.

[51] MARINTEK. *RIFLEX User Manual Version 4.0 rev 3.* Norwegian Marine Technology Research Insitute, Trondheim, Norway, 2013.

[52] Erin Elizabeth Bachynski. *Design and Dynamic Analysis of Tension Leg Platform Wind Turbines.* PhD thesis, Norwegian University of Science and Technology, 2014.

[53] Marit I. Kvittem, Erin E. Bachynski, and Torgeir Moan. Effects of Hydrodynamic Modelling in Fully Coupled Simulations of a Semi-submersible Wind Turbine. *Energy Procedia*, 24:351–362, 2012. doi: 10.1016/j.egypro.2012.06.118.

[54] M. I. Kvittem and T. Moan. Effect of mooring line modelling on motions and structural fatigue damage for a semisubmersible wind turbine. pages 273–278, 2012. URL http://www.scopus.com/inward/record.url?eid=2-s2.0-84866103765&partnerID=40&md5=ff57f8ded31ec3002e19c64f51c4c012.

[55] M. O. L. Hansen and H. A. Madsen. Review Paper on Wind Turbine Aerodynamics. *Journal of Fluids Engineering-Transactions of the Asme*, 133(11), 2011. doi: 11400110.1115/1.4005031. URL <GotoISI>://WOS:000297932200018http://scitation.aip.org/getpdf/servlet/GetPDFServlet?filetype=pdf&id=JFEGA4000133000011114001000001&idtype=cvips&prog=normal.

[56] M.O.L. HANSEN. *Aerodynamics of Wind Turbines.* Earthscan, London, 2nd edition, 2008.

[57] P. J. Moriarty and A. C. Hansen. *AeroDyn Theory Manual.* National Renewable Energy Laboratory, 2005.

[58] Frank M.White. *Fluid Mechenics.* McGraw-Hill, NY, 7 edition, 2009.

[59] Marilena Greco. *Lecture Notes to TMR 4215: Sea Loads.* Department of Marine Hydrodynamics, NTNU, 2012.

[60] Johannes Albert Pinkster. Low frequency second order wave exciting forces on floating structures. 1980.

[61] J. N. Newman. Second-order, slowly-varying forces on vessels in irregular waves. 1974.

[62] C. H. Lee and J. N. Newman. Second-order wave effects on offshore structures. *Proceedings of BOSS94*, pages 133–146, 1994.

[63] MARINTEK. *SIMO Theory Manual Version 4.0 rev 1.* Norwegian Marine Technology Research Insitute, Trondheim, Norway, 2012.

[64] *SESAM User Manual, HydroD v4.6. Wave load & stability analysis of fixed and floating structures.* Det Norsk Veritas, 2013.

[65] MARINTEK. *RIFLEX Theory Manual Version 4.0 rev 0.* Norwegian Marine Technology Research Insitute, Trondheim, Norway, 2012.

[66] C. Bak, F. Zahle, R. Bitsche, T. Kim, A. Yde, L. C. Henriksen, P. B. Andersen, A.Natarajan, and M. H. Hansen. Design and performance of a 10 MW wind turbine. *J. Wind Energy.*

[67] Karl Otto Merz. NOWITECH Reference Turbine, Version 0 - System Description for Dynamic Analysis. Norwegian Research Centre for Offshore Wind Technology, 2013.

[68] Raymond Chow and C. P. van Dam. Verification of computational simulations of the NREL 5 MW rotor with a focus on inboard flow separation. *Wind Energy*, 15 (8):967–981, 2012. doi: 10.1002/we.529.

[69] Aina Crozier. *Design and Dynamic Modeling of the Support Structure for a 10 MW Offshore Wind Turbine*. PhD thesis, Norwegian University of Science and Technology, 2011.

[70] *Guideline for the Certification of Offshore Wind Turbines*. Germanischer Lloyd, 2012.

[71] *IEC 61400-1. Wind turbines - Part 1: Design requirements*. International Electrotechnical Commission, 2005.

[72] C. Luan, Z. Gao, and T. Moan. Conceptual designs of a 5-MW and a 10-MW semi-submersible wind turbine with emphasis on the design procedure. Journal of Offshore Mechanics and Arctic Engineering [Submitted], 2014.

[73] *SESAM User Manual, GeniE v6.4.Concept design and analysis of offshore structures*. Det Norsk Veritas, 2013.

[74] Edward V. Lewis. *Principles of Naval Architecture.*, volume 1. SNAME, Jersey City, NJ, 1988.

[75] *DNV-OS-J101. Design of Offshore Wind Turbine Structures*. Det Norsk Veritas, 2013.

[76] *DNV-RP-C205. Environmental Conditions and Environmental Loads*. Det Norske Veritas, 2010.

[77] *DNV-OS-E302. Offshore Mooring Chain*. Det Norsk Veritas, 2013.

[78] B. J. Jonkman and L. Kilcher. TurbSim User's Guide: Version 1.06.00. Technical report, National Renewable Energy Laboratory, 2012.

[79] Stephan P Timoshenko. On the correction for shear of the differential equation for transverse vibrations of prismatic bars. *Philosophical Magazine*, 41(245):744–746, 1921.

[80] Stephan P Timoshenko. On the transverse vibrations of bars of uniform cross-section. *Philosophical Magazine*, 43(253):125–131, 1922.

[81] Morten H. Hansen, A. D. Hansen, Torben J. Larsen, Stig Øye, Poul Sørensen, and Peter Fuglsang. *Control design for a pitch-regulated, variable speed wind turbine*. 2005. ISBN 8755034098.

[82] Finn Gunnar Nielsen, Tor David Hanson, and Bjørn Skaare. Integrated dynamic analysis of floating offshore wind turbines. In *Proceedings of OMAE2006 25th International Conference on Offshore Mechanics and Arctic Engineering, 49 June 2006, Hamburg, Germany*, 2006.

[83] Jason Mark Jonkman. Influence of control on the pitch damping of a floating wind turbine. Technical report, National Renewable Energy Laboratory, 2008.

[84] Jason M. Jonkman. Dynamics of offshore floating wind turbinesmodel development and verification. *Wind Energy*, 12(5):459–492, 2009.

[85] Torben J. Larsen and Tor D. Hanson. A method to avoid negative damped low frequent tower vibrations for a floating, pitch controlled wind turbine. In *Journal of Physics: Conference Series*, volume 75, page 12073. IOP Publishing, 2007. ISBN 1742-6596.

[86] WAFO-group. *WAFO - A Matlab Toolbox for Analysis of Random Waves and Loads - Tutorial for WAFO version 2.5*. Math. Stat., Center for Math. Sci., Lund University, Lund, Sweden, 2011. URL `http://www.maths.lth.se/matstat/wafo`.

[87] Arvid Naess and Torgeir Moan. *Stochastic dynamics of marine structures*. Cambridge University Press, 2012.

[88] Tony Burton, Nick Jenkins, David Sharpe, and Ervin Bossanyi. *Wind energy handbook*. John Wiley & Sons, 2011.

[89] Madjid Karimirad and Torgeir Moan. Wave-and wind-induced dynamic response of a spar-type offshore wind turbine. *Journal of waterway, port, coastal, and ocean engineering*, 138(1):9–20, 2012.

Appendix A

Drawings of the Semi-submersible Wind Turbine

A.1 Drawing of the Semi-submersible Platform

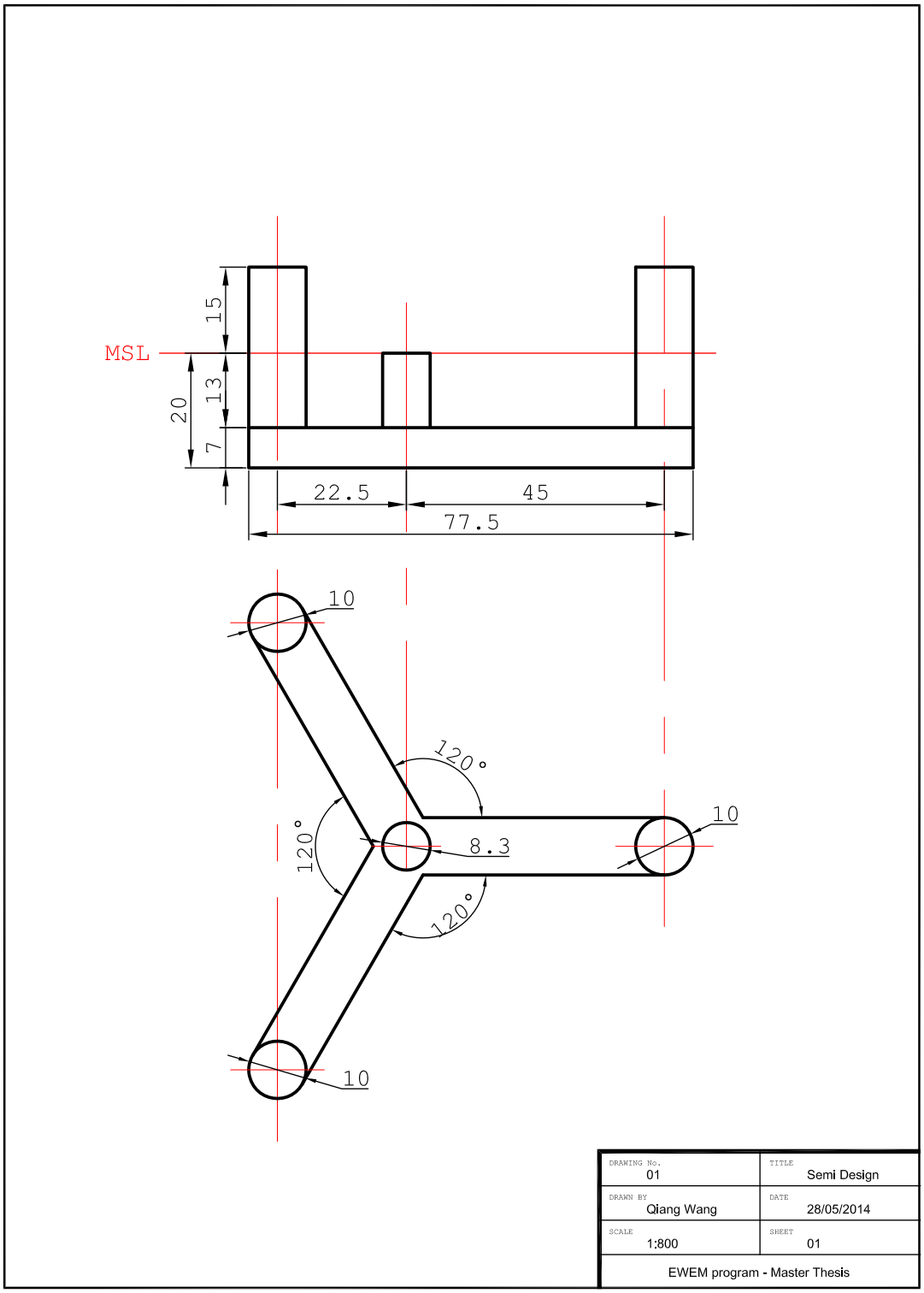

DRAWING No. 01	TITLE Semi Design
DRAWN BY Qiang Wang	DATE 28/05/2014
SCALE 1:800	SHEET 01
EWEM program - Master Thesis	

A.2 Drawing of the Semi-submersible Wind Turbine

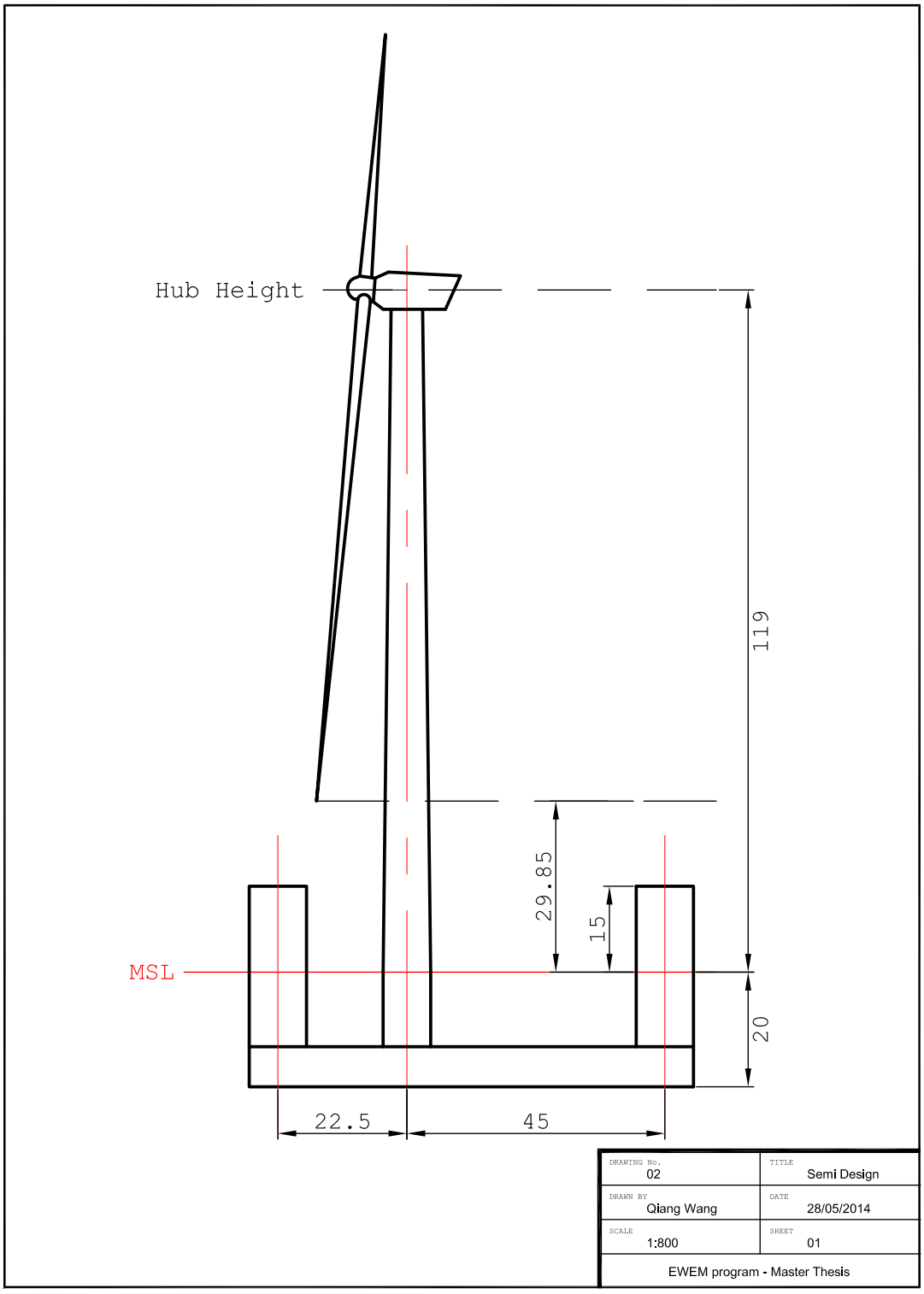

Appendix B

Drawings of the Mooring System

B.1 Drawing of the Mooring System - Top View

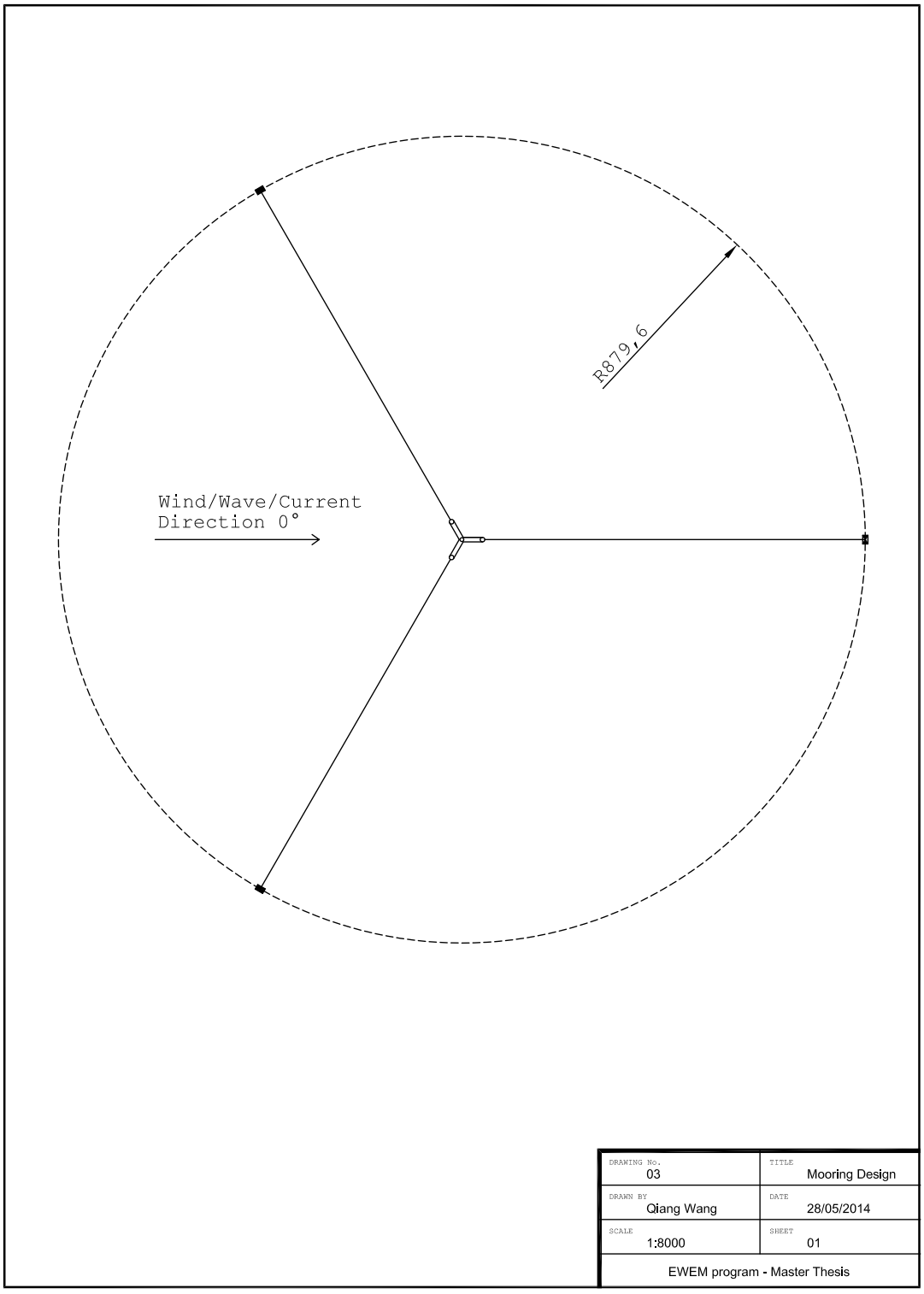

B.2 Drawing of the Mooring System - Side View

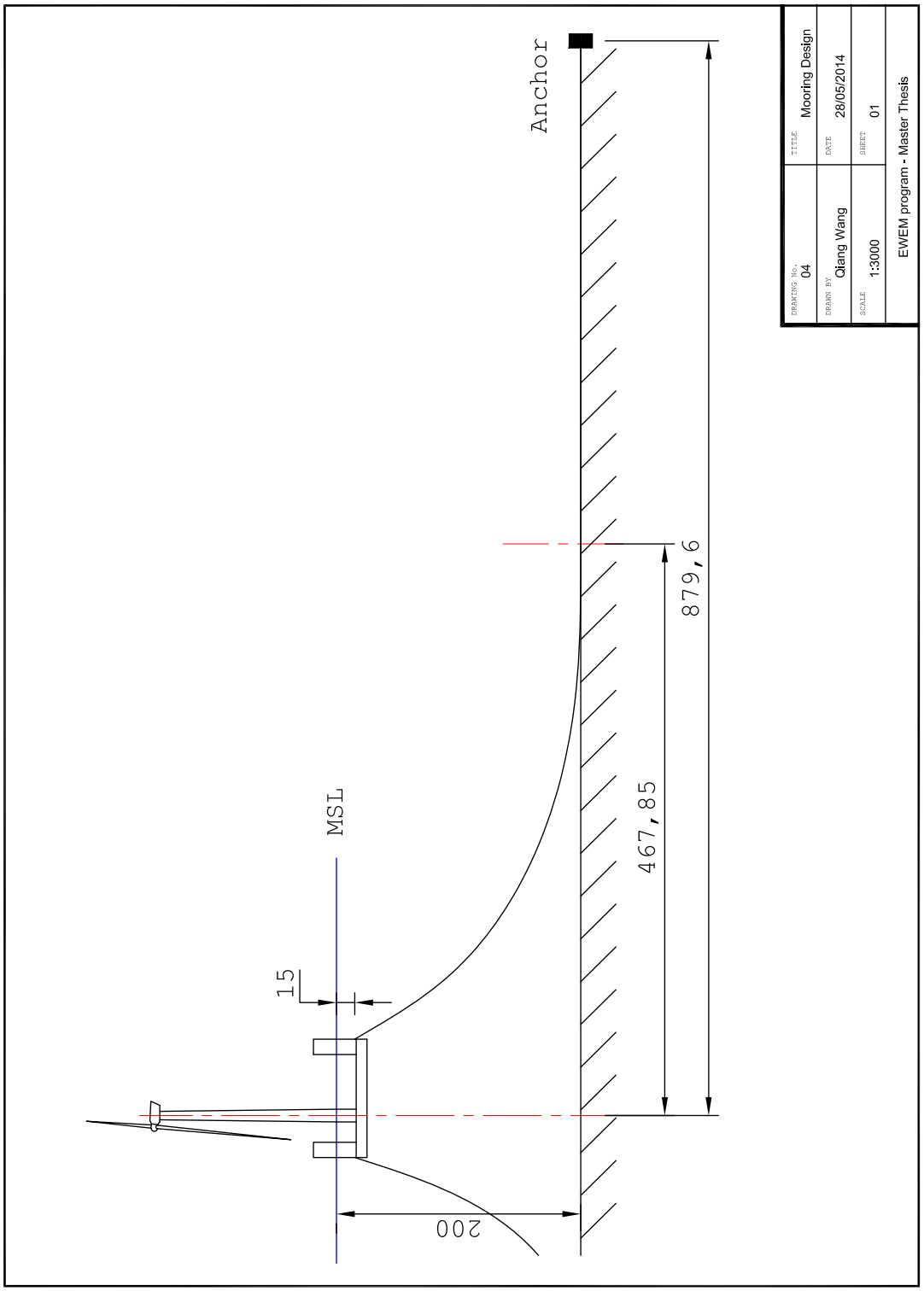

Appendix C

Controller Modification

As shown in Section 7.3.1, when mounting the DTU 10MW RWT onto the semi-submersible platform, large resonant pitch motion of the floater will occur under above rated wind speed.

The resonant pitch motion of the floater is caused by negative damping from the blade pitch controller. This phenomenon is also reported by Nielsen [82] in the analysis of Hywind concept, Jonkman [83] in the analysis of ITI Energy barge concept and Roddier [13] in the analysis of WindFloat concept.

The DTU 10MW RWT controller is based on classical proportional-integral (PI) theory [66]. According Jonkman, such blade pitch control system follows the following equation of motion [84]:

$$\underbrace{\left[I_{Drivetrain}+\frac{1}{\Omega_0}\left(-\frac{\partial P}{\partial\theta}\right)N_{Gear}K_D\right]}_{M_\phi}\ddot{\varphi}+\underbrace{\left[\frac{1}{\Omega_0}\left(-\frac{\partial P}{\partial\theta}\right)N_{Gear}K_P-\frac{P_0}{\Omega_0^2}\right]}_{C_\phi}\dot{\varphi}+\underbrace{\left[\frac{1}{\Omega_0}\left(-\frac{\partial P}{\partial\theta}\right)N_{Gear}K_I\right]}_{K_\phi}\varphi=0 \tag{C.1}$$

Where $I_{Drivetrain}$ is the drivetrain inertia cast to the low speed shaft, N_{Gear} is the high-speed to low-speed gearbox ratio, Ω_0 is the rated low-speed shaft rotational speed, P_0 is the rated mechanical power, $\partial P/\partial\theta$ is the sensitivity of aerodynamic power to the rotor collective blade pitch angle, K_P, K_I and K_D is the blade pitch controller proportional, integral and derivative gain respectively, $\dot{\varphi}=\Delta\Omega$ is the rotor speed error.

It is seen that the rotor speed error will response as a 1 dof dynamic system with natural frequency $\omega_{\varphi n}$, and damping ratio ζ_φ equal to:

$$\omega_{\varphi n}=2\pi f_{\varphi n}=\sqrt{\frac{K_\varphi}{M_\varphi}},\quad and\ \ \zeta_\varphi=\frac{C_\varphi}{2M_\varphi\omega_{\varphi n}} \tag{C.2}$$

In the design of blade pitch controller [81], the PI gains can be determined by neglecting the derivative gain and negative damping term in Equation (C.1):

$$K_P=\frac{2I_{Drivetrain}\Omega_0\zeta_\varphi\omega_{\varphi n}}{N_{Gear}\left(-\frac{\partial P}{\partial\theta}\right)},\quad and\ \ K_I=\frac{I_{Drivetrain}\Omega_0\omega_{\varphi n}^2}{N_{Gear}\left(-\frac{\partial P}{\partial\theta}\right)} \tag{C.3}$$

Currently, the land-based DTU 10MW RWT uses blade pitch controller natural frequency of 0.06Hz (0.38rad/s) and a damping ratio of 0.7. This natural frequency is above the natural frequency of the floater pitch motion, 0.04Hz (0.24rad/s). According to Larsen [85], the smallest controller response natural frequency must be lower than the smallest critical support structure natural frequency to ensure that the support structure motions of an offshore floating wind turbine with active pitch-to-feather control remain positively damped. Therefore, reducing the controller response natural frequency to 0.03Hz (0.19rad/s) will ensure that it is lower than the floater pitch natural frequency and lower than the excitation frequency of most sea states.

Therefore, the PI gains are reduced according to Equation (C.3) to achieve the desired controller response natural frequency while keeping the damping ratio unchanged as shown in Table C.1. Figure C.1 confirms that the modification successfully avoids the platform pitch resonance.

Table C.1: *Modification of PI gains of the DTU blade pitch controller*

Item	Default value for the land-based DTU 10MW RWT	Target value for the floating DTU 10MW RWT
Blade pitch controller natural frequency [Hz]	0.06	0.03
Proportional gain [-]	0.524485	0.262243
Integral gain [-]	0.141233	0.035308

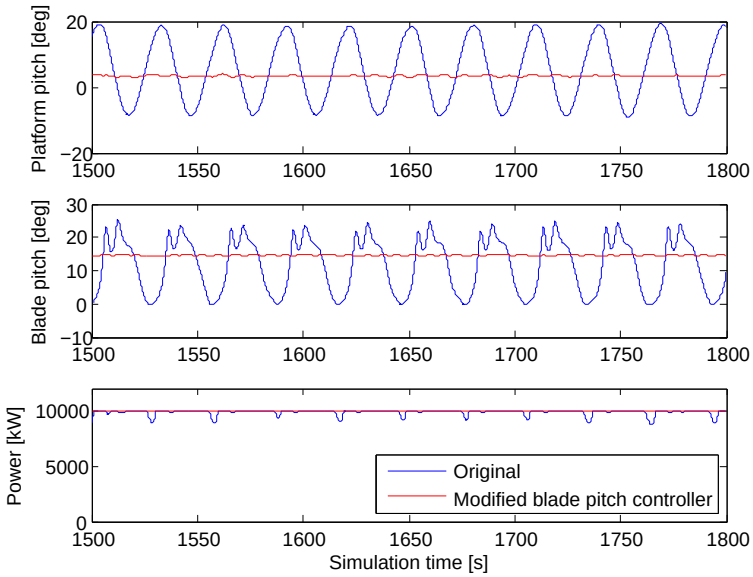

Figure C.1: *Comparison of response of the floating DTU 10MW RWT with the original and the modified blade pitch controllers*

Appendix D

Response Spectra of the Floating Wind Turbine

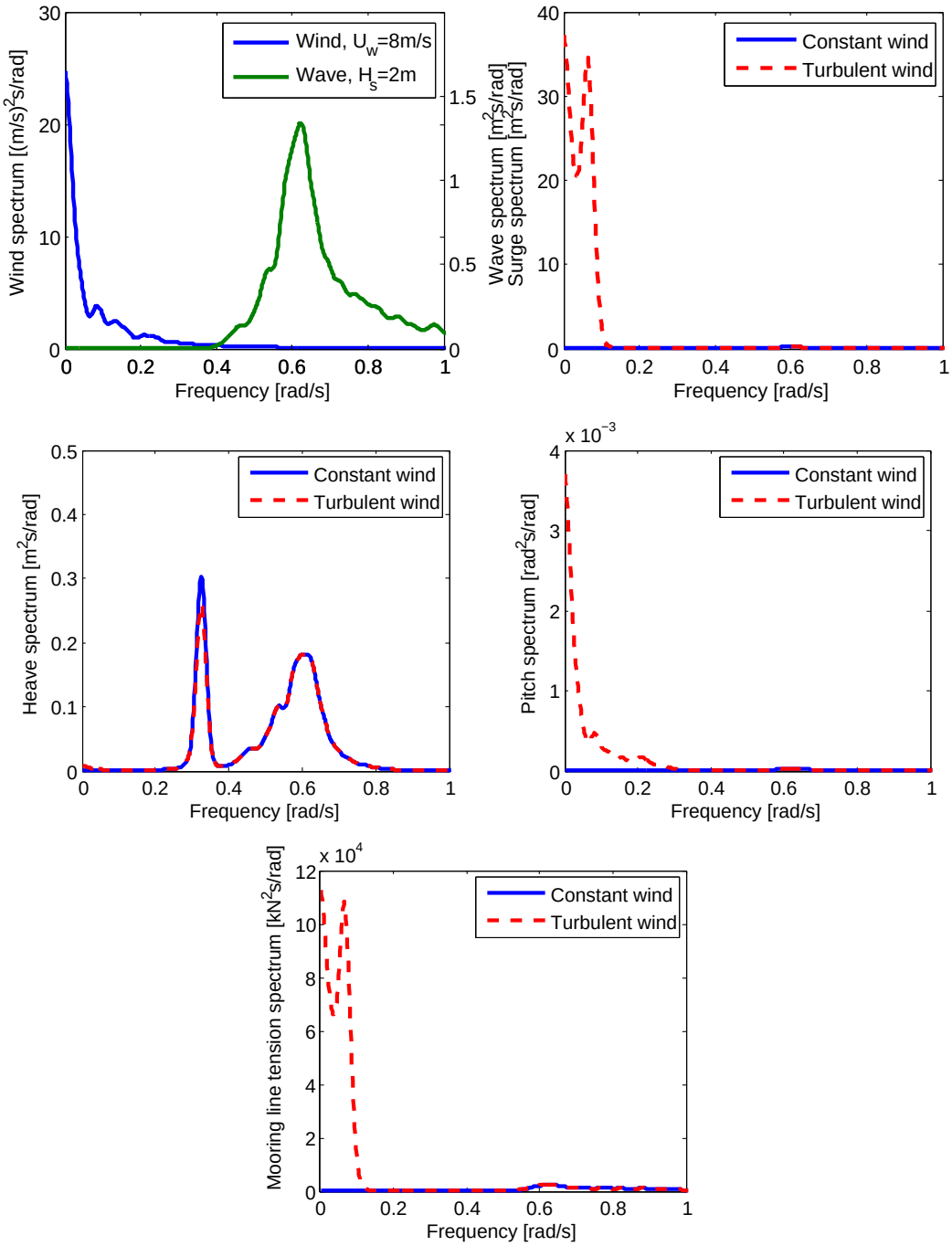

Figure D.1: *Smoothed turbulent wind and wave spectra (upleft) and smoothed spectra of floating wind turbine responses: surge spectrum (upright), heave spectrum (middleleft), pitch spectrum (middleright) and mooring line fairlead tension spectrum (downleft), response spectra are compared under turbulent and constant wind conditions for load case OP1*

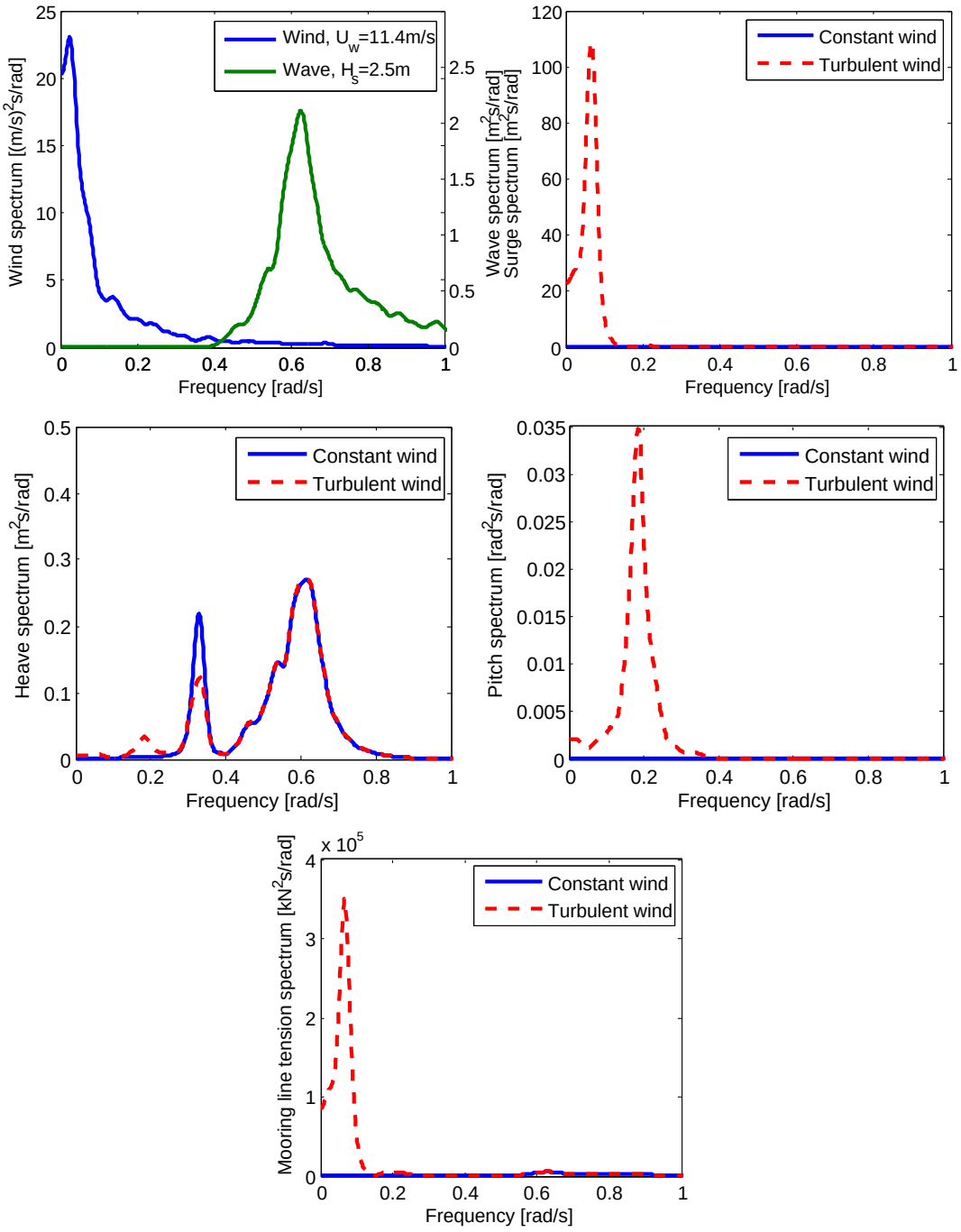

Figure D.2: *Smoothed turbulent wind and wave spectra (upleft) and smoothed spectra of floating wind turbine responses: surge spectrum (upright), heave spectrum (middleleft), pitch spectrum (middleright) and mooring line fairlead tension spectrum (downleft), response spectra are compared under turbulent and constant wind conditions for load case OP2*

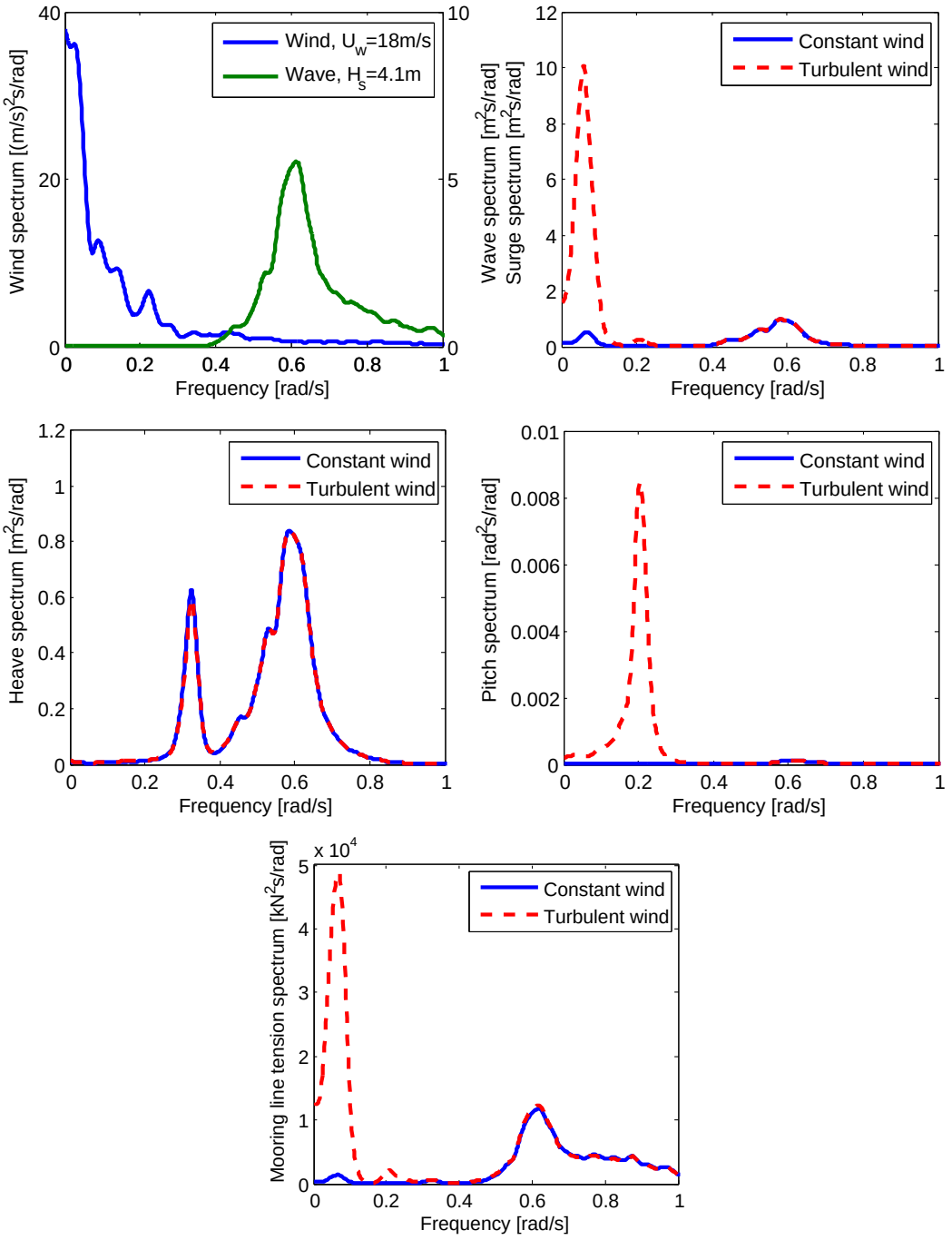

Figure D.3: *Smoothed turbulent wind and wave spectra (upleft) and smoothed spectra of floating wind turbine responses: surge spectrum (upright), heave spectrum (middleleft), pitch spectrum (middleright) and mooring line fairlead tension spectrum (downleft), response spectra are compared under turbulent and constant wind conditions for load case OP3*

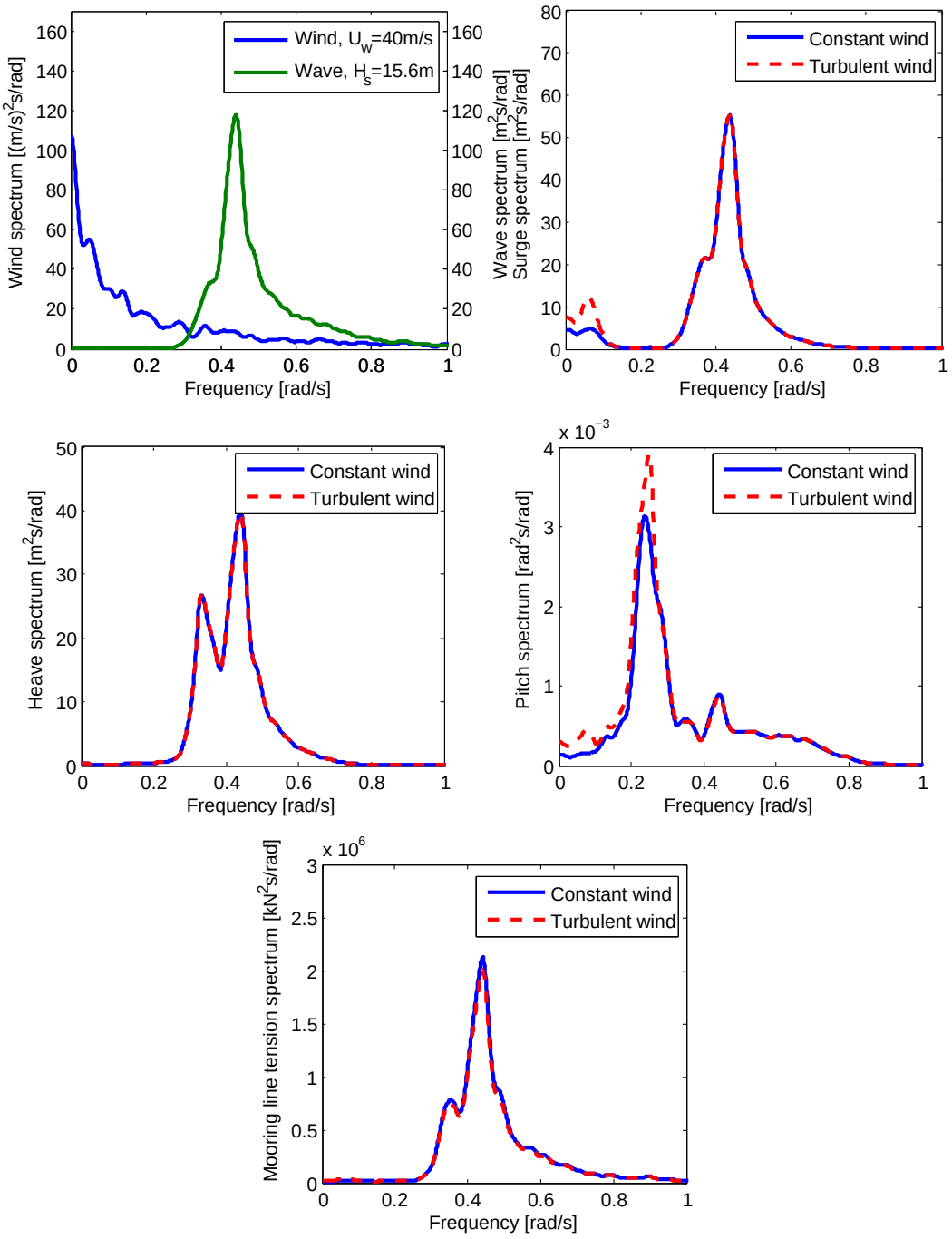

Figure D.4: *Smoothed turbulent wind and wave spectra (upleft) and smoothed spectra of floating wind turbine responses: surge spectrum (upright), heave spectrum (middleleft), pitch spectrum (middleright) and mooring line fairlead tension spectrum (downleft), response spectra are compared under turbulent and constant wind conditions for load case EX*

Appendix E

Structral Response Spectra of the Wind Turbine

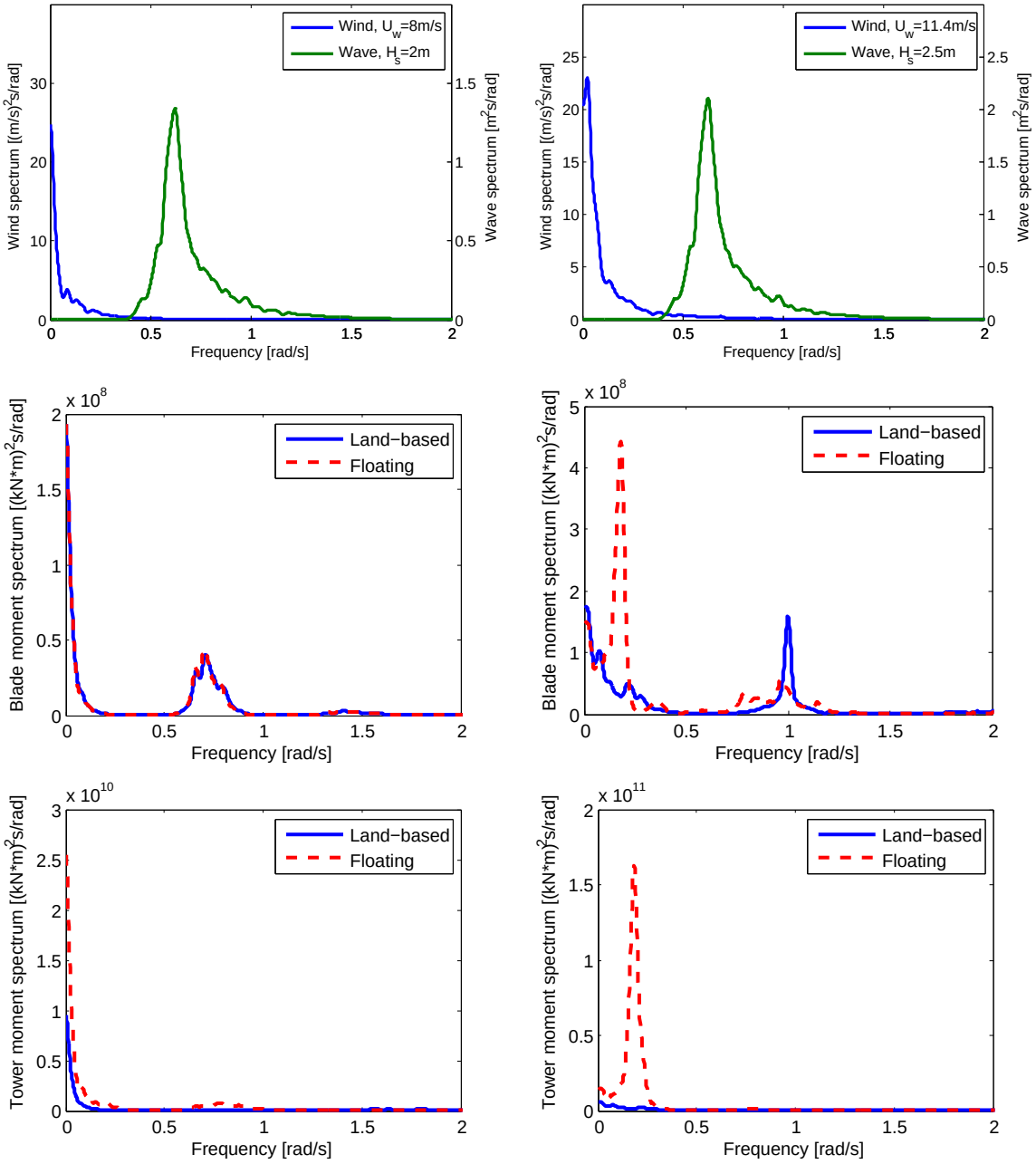

(a) Response spectra for load case OP1 (b) Response spectra for load case OP2

Figure E.1: *Comparison of land-based and floating wind turbine blade root out-of-plane bending moment and tower base fore-aft bending moment response spectra for load case OP1(a) and OP2(b)*

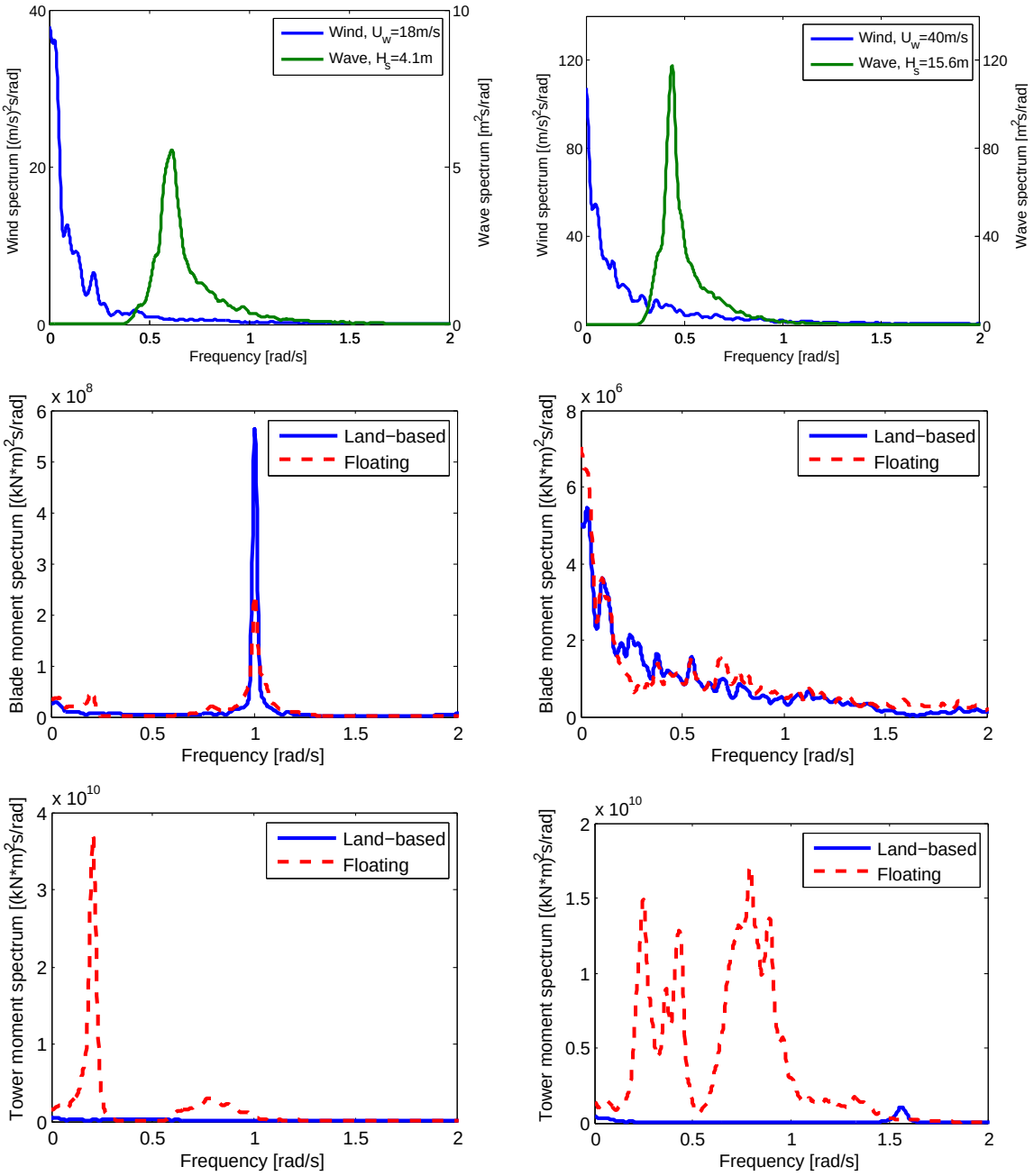

(a) Response spectra for load case OP3 (b) Response spectra for load case EX

Figure E.2: *Comparison of land-based and floating wind turbine blade root out-of-plane bending moment and tower base fore-aft bending moment response spectra for load case OP3(a) and Ex(b)*